Fault Detection and Restoration for Hybrid HVDC Systems

by

Mohan Du

A thesis
presented to the University of Waterloo
in fulfillment of the
thesis requirement for the degree of
Master of Applied Science
in
Electrical and Computer Engineering

Waterloo, Ontario, Canada, 2021

Author's Declaration

I hereby declare that I am the sole author of this thesis. This is a true copy of the thesis, including any required final revisions, as accepted by my examiners.

I understand that my thesis may be made electronically available to the public.

Abstract

As a promising solution for connecting remote, asynchronous, and intermittent renewable energy resources with existing AC grids, high voltage direct current (HVDC) systems are being built in many countries around the world. HVDC lines are used for bulk power transmission over long distances with low power losses and high security, reliability, and system stability. With the development of various HVDC technologies, HVDC systems in various forms are being constructed, and eventually will be connected to each others. The expansion of HVDC grids may result in systems with HVDC converters that have different fault blocking capabilities. Even though considerable relaying and restoration algorithms are developed for HVDC systems, many of these algorithms are only applicable to one specific type of HVDC converter. This thesis presents a universal protection scheme that can be implemented in HVDC grids with different topologies and with converters that have different fault blocking capability, i.e., half-bridge modular multilevel converter (HB-MMC) and full-bridge MMC (FB-MMC).

A fault current calculation method is developed first to calculate the current derivative of each line in an HVDC system during a DC fault. The developed method calculates fault currents by solving matrix-form differential equations, whose matrices can be automatically built based on system parameters and without requiring any information corresponding to the fault condition. The calculation method can be used in HVDC grids with various topologies, structures, and fault types. The universal protection scheme consists of a universal relaying scheme and a universal restoration algorithm. The universal relaying scheme provides a systematic approach to design the current derivative-based relaying algorithm for a specific HVDC system. The relaying algorithm compares the locally measured current derivative with thresholds to detect DC faults in HVDC systems and to differentiate between internal and external faults. Instead of using the traditional method, which is based on extensive time-consuming electromagnetic transient (EMT) simulations, to determine the relay settings, this thesis developed a systematic method to calculate the settings. The universal restoration algorithm can quickly and reliably restore a hybrid HVDC system with different types of converters including HB-MMCs and FB-MMCs.

Study results show that (i) the matrix-form differential equations can calculate the current derivative of each line right after a DC fault accurately and quickly, (ii) for most HVDC configurations and fault scenarios, settings of each relay can be calculated using the matrix-form differential equations, (iii) the developed relaying algorithm selectively detects internal faults in a few milliseconds and meets

the requirement of dependability and security, (iv) the developed restoration algorithm restores hybrid HVDC systems with low voltage oscillations and limited inrush currents, and (v) the developed relaying scheme and restoration algorithm are flexible and can be employed to HVDC grids with different combinations of converter topologies and technologies with limited modifications.

Acknowledgements

First and foremost, I would like to express my sincere gratitude to my supervisor, Dr. Sahar Pirooz Azad, for her enormous support throughout my M.A.Sc studies. It was her professional guidance, insightful advising, and constant encouragement that helped me overcome the challenges in my academic life. During the process of developing this thesis, Dr. Azad devoted immeasurable time, energy, and inspiring patience to providing constructive feedback. It is my honor to be supervised by Dr. Azad in my program, and Dr. Azad will always be the academic model throughout my life.

I also want to express my thanks to Prof. Kankar Bhattacharya and Prof. Sheshakamal Jayaram for serving in my thesis committee and providing valuable comments to my thesis.

I owe special thanks to the comments, suggestions, and support provided by the members in our academic group.

Finally, I would like to thank my family and friends for their unconditional support.

Dedication

To my dear parents, Huayang and Pengxiang, whom I will always be indebted to.

Table of Contents

List of Figures

List of Tables

Nomenclature

$\boldsymbol{i}, \boldsymbol{v}$	current and voltage vectors
$\mathbf{0}, \mathbf{1}, \mathbf{I}$	all-zeros, all-ones, and identity matrices
$\mathbf{A}$	incidence matrix for an HVDC grid
$\mathbf{R}, \mathbf{L}, \mathbf{E}$	resistance, inductance, and elastance matrices
$\mathcal{U}(\cdot), \mathcal{L}(\cdot)$	upper and lower bounds for a variable
$\square^g, \square^c, \square^l$	elements corresponding to the grounding branch, equivalent MMC branch, and transmission line (the empty squares represent any variables)
$\square^p, \square^n, \square^m$	elements corresponding to the positive, negative, and metallic poles
$\square_0, \square_f$	elements corresponding to the pre-fault and post-fault scenarios
$\square_{jk}$	elements corresponding to line jk
$\square_j, \square_f$	elements corresponding to terminal j and the fault point
$\square_{pp}, \square_{pg}, \square_{pm}$	elements corresponding to the pole-to-pole, pole-to-ground, and pole-to-metallic fault scenarios
$DI_{\square}^{th\square}$	the threshold for the current derivative-based relaying algorithm
r^{arm}, l^{arm}	arm resistance and inductance of an MMC
V_{dc}	rated DC voltage of an MMC
V_m	peak AC phase voltage

P2G	pole-to-ground
P2M	pole-to-metallic
P2P	pole-to-pole

Chapter 1

Introduction

1.1 HVDC grids

The global warming resulted from the extensive burning of fossil fuels has demonstrate devastating impacts on the environment, wildlife, and humans, such as extreme heat waves, biodiversity loss, and food crisis [7, 8]. As a response to the climate-change threat, 194 states and the European Union have signed the Paris Agreement by February 2021, which aims to limit the global temperature rise of this century well below 2 degrees Celsius above pre-industrial levels [9]. This goal should be achieved by obtaining net-zero emission of carbon dioxide (CO_2) by 2050 [10], where zero-carbon resources are expected to supply 76% of electricity globally [11]. Particularly, as the main driver of this decarbonization process, wind and PV sources should grow from 9% of the global electricity generation today to 56% by 2050 [11]. However, the addition of renewable resources to the existing energy system to reduce the CO_2 emission has resulted in various challenges to the security and stability of traditional alternating current (AC) transmission systems due to the distributed and fluctuating nature of renewable resources [5].

The high voltage direct current (HVDC) technology has significant potential for resolving the security and stability issues of the AC power systems integrated with large amounts of renewable resources because HVDC systems offer better control on the power transmission compared to traditional AC systems [2, 12]. Furthermore, HVDC lines can connect two asynchronous power systems and serve as a boundary in case of a cascading failure. HVDC systems also offer a lower power loss for long-distance power transmission between load centers and remote renewable resources

[13]. All of the benefits of HVDC transmissions have resulted in a boost in the HVDC market. According to [14, 15], the global HVDC converter station market is expected to grow from USD 7.9 billion in 2017 to USD 15.74 billion by 2026, with an average annual growth rate of 7.96%.

By 2020, there have been more than 200 HVDC projects operating or being constructed all over the world [16]. These HVDC systems vary in topology, converter type, grounding configuration, and grid configuration. For example, the world's first commercial HVDC link, Gotland 1, was operated in 1954 and is a point-to-point asymmetric monopole grid based on the mercury arc valve using the sea for the return current [17]. With the development of HVDC technology, in recent HVDC projects, the state-of-art converters, environment-friendly grounding options, and more flexible configurations are used to increase the controllability, flexibility, and DC voltage level. For example, the Zhoushan five-terminal HVDC grid operated in 2014 is a bipolar grid using the modular multilevel converter (MMC) at each station [18], Fig. 1.1. Compared to Gotland 1, the Zhoushan HVDC grid has a higher degree of controllability on the DC voltage [19] and more redundancy in case of the loss of a transmission pole [20]. The different topology, type of converters, grounding configuration, and grid configuration of HVDC systems will result in different fault responses, the analysis of which has significant importance to HVDC protection design.

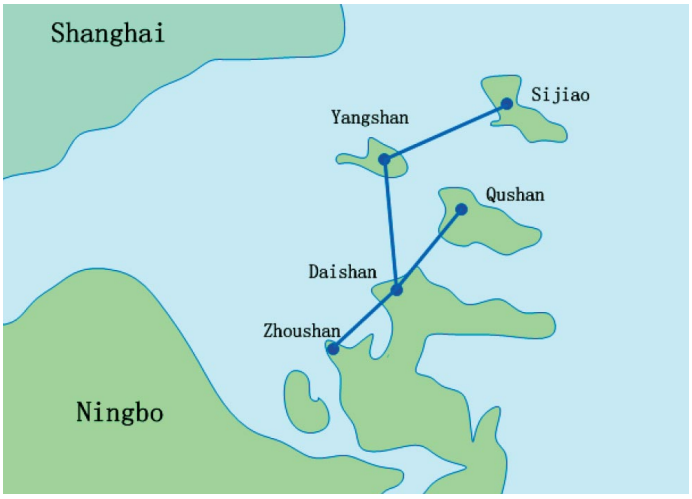

Figure 1.1: Zhoushan five-terminal HVDC grid [1].

1.1.1 Converters of HVDC Systems

There are three main technologies for HVDC converters, the line commuted converter (LCC), two-level and three-level voltage source converters (VSCs), and the modular multilevel converter (MMC) [21, 22]. For the sake of simplicity, VSC in the remaining part of this thesis corresponds to a two-level or three-level converter.

The LCC, also known as a current source converter, uses semi-controlled thyristors as switches [21]. On the contrary, the VSC, which employs fully-controlled insulated-gate bipolar transistors (IGBTs) for AC-DC conversion, has a higher degree of controllability than the LCC. The VSC is able to [21, 23]

- be connected with a weak AC grid,
- perform black start,
- control active power and reactive power separately, and thus requires no additional reactive power compensation, and
- achieve a bi-directional power transmission.

However, a VSC should operate at a high frequency to reduce harmonics in the DC voltage waveform, which will result in high switching losses. Furthermore, the voltage level of a VSC is restricted by the voltage rating of IGBTs. In order to overcome the two main disadvantages of the VSC, the technology of MMC was developed [23]. An MMC consists of six arms, where each arm connects an AC phase to a DC pole. Multiple submodules (SMs) are connected in series and controlled separately in each arm of an MMC. The voltage level of an MMC can be easily increased by increasing the number of SMs in each arm. Meanwhile, the switching frequency of each IGBT in an SM is around the AC frequency. Compared to the VSC, the MMC [22, 24]

- has lower switching losses,
- has a lower requirement for IGBT's voltage rating,
- does not require the DC-link capacitor,
- can be modularly designed, and
- can generate the DC voltage with fewer harmonics.

Being benefited by so many advantages, the MMC has become the most favorable type of converter for HVDC systems [25]. This thesis will only focus on HVDC systems based on MMCs.

Each SM is a basic AC-DC conversion circuit consisting of IGBTs, freewheeling-diodes, and DC capacitors. Different types of SMs have various operating principles and fault ride-through characteristics. This subsection will introduce two basic SMs, the half-bridge (HB)-SM and the full-bridge (FB)-SM.

An HB-SM consists of two IGBTs with freewheeling-diodes (S_1 and $\overline{S_1}$) and a DC capacitor (C) [22], Fig. 1.2(a). During the normal operation, the capacitor voltage v_c is regulated around a constant value $\frac{V_{dc}}{N_{\text{SM}}}$, where V_{dc} is the rated output DC voltage of the MMC, and N_{SM} is the number of SMs in each arm of the MMC. An HB-SM can output a two-level voltage, v_c or 0. If S_1 is in the on-state ($S_1 = 1$), the output voltage v_H is v_c; if S_1 is in the off-state ($S_1 = 0$), $v_H = 0$. Since an HB-SM can only generate a monopole output voltage, V_{dc} of an HB-MMC cannot be smaller than the peak AC phase voltage [26]. If a DC fault occurs, the MMC will be blocked—all IGBTs in the MMC are switched to the off-state—to protect each device from being damaged by the large DC fault current. However, the HB-SM does not have the fault-current interrupting capability. Even though the each HB-SM is blocked during the fault, the fault current can still flow through the freewheeling-diodes until the fault disappears, the MMC is disconnected from the fault, or the AC grid is disconnected from the MMC. As a compensation for HB-MMC's incapability of interrupting the fault current, DC circuit breakers (DCCBs) or AC circuit breakers (ACCBs) should be installed on the DC side or the AC side, respectively.

An FB-SM consists of four IGBTs with freewheeling-diodes (S_1, $\overline{S_1}$, S_2, and $\overline{S_2}$) and a capacitor (C), Fig. 1.2(b). Each FB-SM can output a three-level voltage, v_c, $-v_c$, or 0. If S_1 and S_2 are both 1, $v_F = v_c$; conversely, if S_1 and S_2 are both 0, $v_F = -v_c$; if S_1 and S_2 are of different values ($S_1 = 1$ and $S_2 = 0$ or $S_1 = 0$ and $S_2 = 1$), $v_F = 0$. Since an FB-SM can generate a bipolar output voltage, the V_{dc} of a FB-MMC can be smaller than the peak AC phase voltage [26]. This characteristic is useful for a FB-MMC to raise the DC grid voltage smoothly during the restoration process. If a FB-MMC is blocked during a fault, the four IGBTs in each FB-SM will all be switched to the off-state so that the fault current cannot flow through them. In this case, the DC fault current will be interrupted by the FB-MMC when each FB-SM capacitors are fully charged. Fig. 1.3 shows the fault-current path in an FB-MMC, whose each arm contains only one FB-SM for the sake of simplicity and AC side is Δ-connected. For example, after the occurrence of a pole-to-pole (P2P) fault in an HVDC grid, if the phase A-to-C voltage reaches its peak, the fault

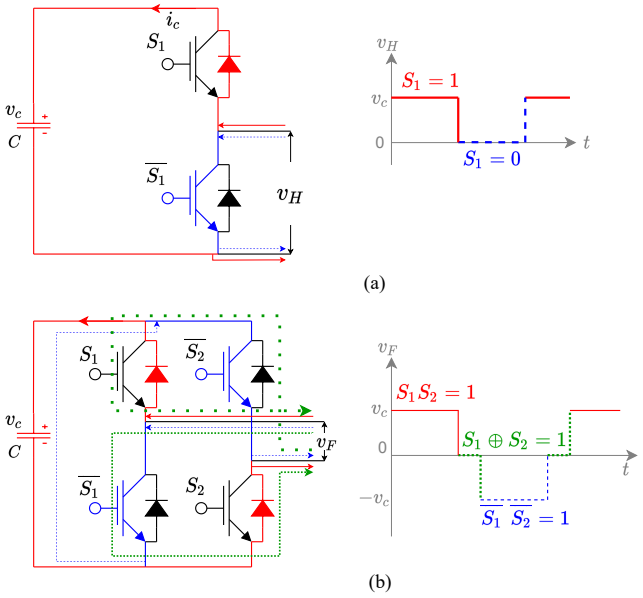

Figure 1.2: (a) HB-SM's and (b) FB-SM's circuits and output voltage waveforms.

current will flow from phase A, flow through the diodes in the SMs on the upper arm connected to phase A, charge the capacitors in these SMs, flow from the positive pole to the negative pole through the fault point, flow through the SMs on the lower arm connected to phase C, charge corresponding capacitors, and return to phase C, Fig. 1.3. During the process that the fault current charges SM capacitors, the capacitor voltages are rising. When the sum of SM-capacitor voltages of an upper arm and a lower arm rises to the peak phase-to-phase AC voltage V_m, the AC side will not feed any fault current to the HVDC grid. As a result, the fault current is interrupted by the blocked FB-MMC. Since FB-MMCs can interrupt fault currents, neither DCCBs nor ACCBs are required to be installed around FB-MMCs in a point-to-point HVDC link.

1.1.2 HVDC System Structure

Based on structure, HVDC systems can be classified into point-to-point HVDC links, multi-terminal HVDC (MTDC) grids, and meshed HVDC grids [2]. HVDC systems in these three structures are shown in Fig. 1.4.

The point-to-point HVDC link can be embedded in an AC grid for transferring bulk electric power over long distances. Both an MTDC grid and a meshed HVDC

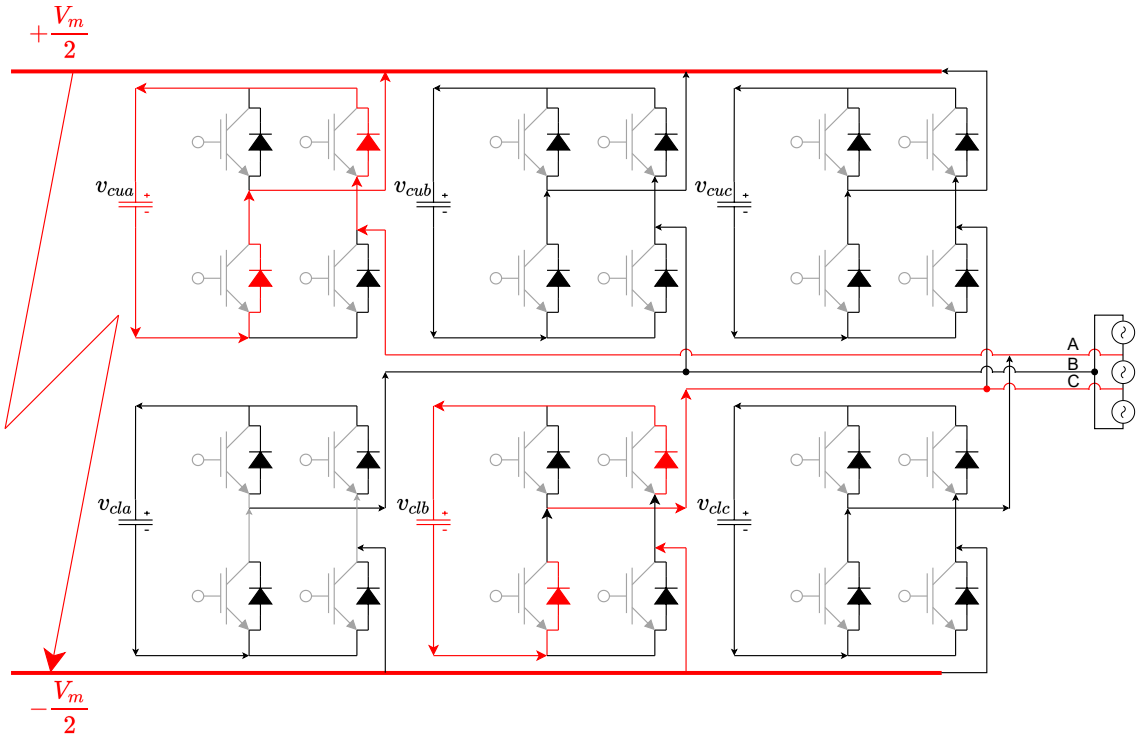

Figure 1.3: Fault-current path in an FM-MMC during a P2P fault.

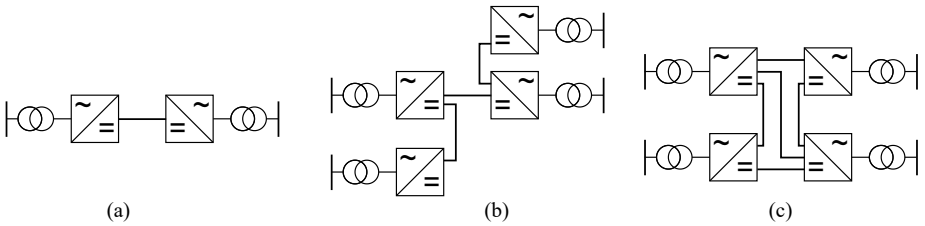

Figure 1.4: Structure of HVDC systems: (a) point-to-point HVDC link, (b) MTDC grid, and (c) meshed HVDC grid [2].

grid contain multiple converter terminals. The major difference between these two grids is that the meshed HVDC grid contains at least one loop while an MTDC grid does not [2]. Being benefited by the transmission loop, a meshed HVDC grid can function normally even when a transmission line in the loop is lost. However, a more complex grid structure requires more advanced converters. For example, a meshed HVDC grid can only use VSCs or MMCs, while an MTDC grid can use LCCs, VSCs,

or MMCs. Compared to traditional HVAC grids, meshed HVDC grids and MTDC grids demonstrate an improved performance in reducing grid congestion, providing increased system stability, and enabling the interconnection of asynchronous power resources [2].

1.1.3 Topology and Grounding Configurations of HVDC Systems

HVDC systems can be formed in various topologies such as symmetric monopole, asymmetric monopole with ground or metallic return, and bipole with ground or metallic return [20], Fig. 1.5. This subsection will introduce the above five topologies with their corresponding grounding configurations briefly.

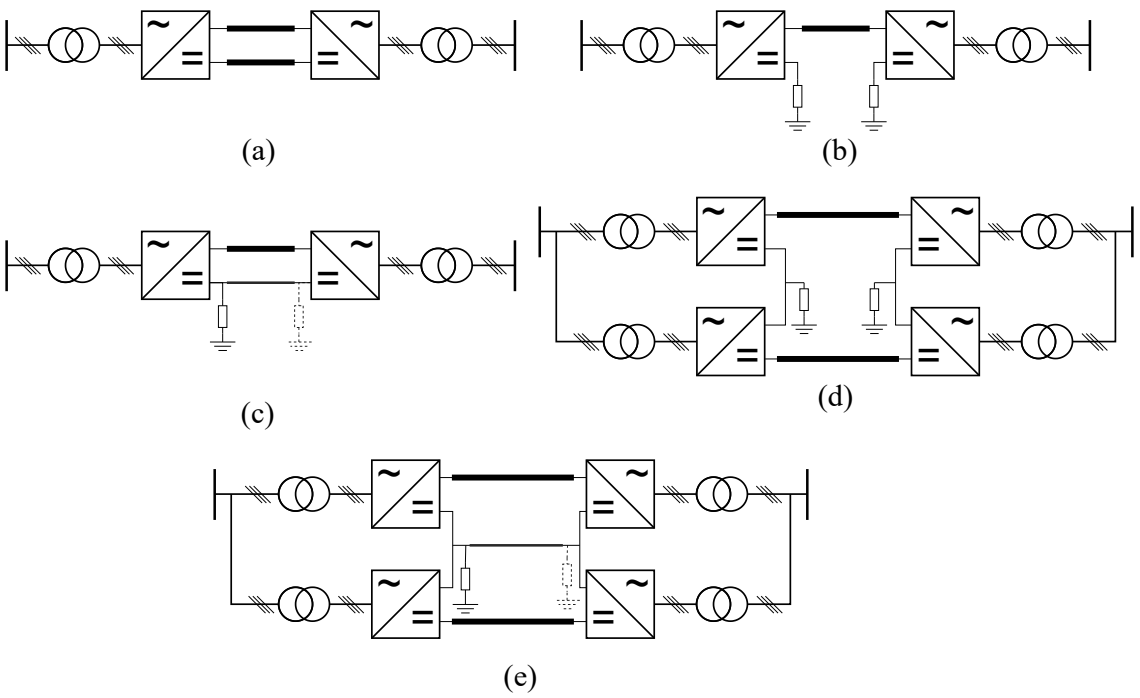

Figure 1.5: Topology of a point-to-point HVDC link: (a) symmetric monopole configuration, (b) asymmetric monopole configuration with ground return, (c) asymmetric monopole configuration with metallic return, (d) bipolar configuration with ground return, and (e) bipolar configuration with metallic return [3].

A symmetric monopole system contains one MMC at each terminal and employs

two transmission lines corresponding to two poles for a transmission path, where each line requires full insulation. If a P2P fault occurs on the transmission line, the power transmission in this system will be interrupted until the fault is cleared. If a pole-to-ground fault occurs, the fault response of the system varies depending on the grounding configuration on the AC side [4], Fig. 1.6. In the first grounding configuration, the transformer on the AC side is Y-Δ connected to the MMC, and grounding branches are installed between the transformer and the MMC, Fig. 1.6(a). If a P2G fault occurs, the grounding branches will supply the unbalanced fault current. In order to restrict the magnitude and rising speed of fault current, inductors and resister in grounding branches should be large, e.g., $L_g = 3$ H and $R_g = 1000\,\Omega$ [6]. In the second grounding configuration, the transformer is Δ-Y connected to the MMC, and a large grounding resister is connected to the neutral point of the transformer, Fig. 1.6(b). The flowing path of fault current in this configuration during a P2G fault is similar to that in the first configuration, except the fault current in this configuration will flow through the secondary side of the transformer. From the transformer protection perspective, this configuration can only be used in low voltage systems. In the third configuration, the transformer is Δ-Y connected to the MMC, and two series-connected resistors are installed on the DC side with the neutral point grounded, Fig. 1.6(c). These two resistors may result in DC voltage unbalance and will increase the power loss. Consequently, this configuration cannot be used in a high-voltage grid. Among the three configurations, the first grounding configuration is the most reliable and is used in many existing HVDC systems, e.g., the Trans Bay Cable in the USA. As a result, in this thesis, the symmetric monopole grid has the first grounding configuration.

An asymmetric monopole system only uses one pole for power transmission, and that pole is preferred to be the negative pole to reduce corona effects [27]. The return current can flow through the ground or metallic conductor. If the ground return is used, each terminal should be low-impedance grounded to reduce the power loss [20]. In this configuration, continuous return current will flow through the ground along the transmission path, which requires specific permission [3]. Specifically, sea can also be used for the return current, e.g., Gotland 1 HVDC line [17]. If the metallic return is used, only one terminal should be low-impedance grounded, and other terminals can be high-resistance grounded or ungrounded [20].

A bipolar system contains two MMCs at each terminal, where each MMC connects a pole and the neutral point, which can be low- or high-impedance grounded. The grid can use ground return or metallic return [20]. If the ground return is used, all terminals should be low-impedance or high-impedance grounded. In this config-

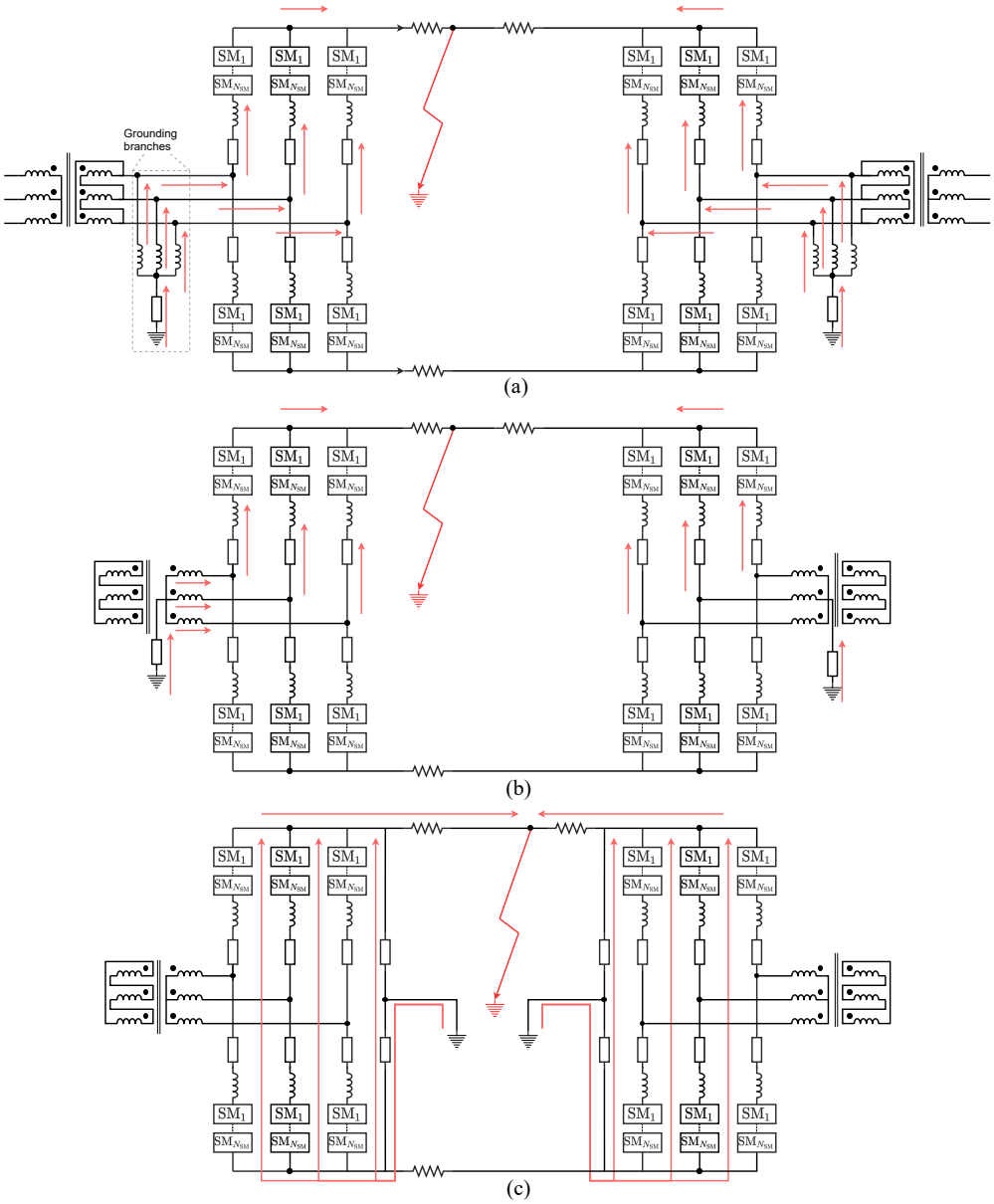

Figure 1.6: Grounding configuration for a symmetric monopole point-to-point HVDC link: (a) with grounding branches between the transformer and MMC, (b) with a resistor connecting to the neutral point of the transformer, and (c) with series-connected resistors on the DC side [4].

uration, no continuous ground current will flow through the transmission path, but the permission for temporary operating with ground current is still required [3]. If the metallic return is used, at least one terminal should be grounded, and other terminals can be high-impedance grounded or ungrounded. The bipolar grid has a 50% redundancy; therefore, if a P2G or pole-to-metallic (P2M) fault occurs on the grid, the power transmission on the healthy pole—50% of the rated grid capacity—will not be interrupted.

1.2 Statement of the Problem and Thesis Objectives

Although extensive research has been conducted on the protection of HVDC systems, a universal protection scheme for HVDC systems in various forms has not been proposed. The objective of this thesis is to develop a universal protection scheme that is suitable for HVDC systems in various forms. The variety of system forms includes three aspects:

- structure of the system, i.e., point-to-point, MTDC, or meshed HVDC,
- type of MMCs in the system, i.e., only FB-MMCs, only HB-MMCs, or both FB- and HB-MMCs, and
- system topology and grounding configuration, i.e., symmetric monopole, asymmetric monopole with ground or metallic return, or bipole with ground or metallic return.

A universal protection scheme for HVDC systems contains two parts: a universal relaying scheme and a universal restoration algorithm to quickly restore the system with low voltage oscillations and limited inrush currents. The developed relaying scheme only uses the locally measured current derivatives to detect internal faults, and the relay settings are calculated based on differential equations of the system after fault occurrence instead of being obtained by extensive time-consuming electromagnetic transient (EMT) simulations.

In order to fulfill the objective of this thesis, the following methodology is used:

- Each component in an MMC-based HVDC system is linearized and an equivalent circuit of an MMC-based HVDC system right after a DC fault is built,

- A matrix-form differential equation that can calculate the current derivative of each line right after a DC fault is developed (for each grid form and each fault scenario, a matrix-form equation is developed),
- A method that uses the calculated post-fault current derivative of each line to determine the setting of each relay in an HVDC system is developed,
- A linear control block for HB-MMCs to raise the grid DC voltage stably during the restoration process is designed, and
- Time-domain simulations in PSCAD/EMTDC that can demonstrate the feasibility of the relaying scheme and restoration algorithm are performed. Various grid configurations and fault scenarios are investigated in PSCAD/EMTDC.

1.3 Thesis Layout

The rest of this thesis is organized as follows:

- Chapter 2 presents an approach to build the equivalent circuits and construct the matrix-form differential equations for post-fault MMC-HVDC grids in various topologies under various fault scenarios. In the simulation section, the matrix-form differential equation is used to calculate the fault current in an HVDC grid right after a DC fault. The accuracy of the differential equation is discussed in various grid topologies under various fault scenarios.
- Chapter 3 presents a universal relaying scheme, specific relaying algorithms corresponding to various grid topologies, and a new method that uses differential equations to calculate the relay settings. In the simulation section, various types of DC faults are employed to grids in various topologies to evaluate the performance of the developed relaying algorithms and the calculated relaying settings.
- Chapter 4 analyzes the voltage-control and power-control abilities of FB- and HB-MMCs during the restoration process and presents a universal algorithm for the restoration of various types of HVDC grids, which may even contain different types of MMCs with and without fault blocking capability. A voltage-control block is designed for HB-MMCs to stabilize the rise of the DC voltage during restoration when the HB-MMC controls the DC voltage in the HVDC

grid. In the simulation section, the performances of the developed restoration algorithm is evaluated.

- Chapter 5 presents the contributions and conclusions of this thesis and points out the directions for future work.

Chapter 2

Fault-Current Calculation for HVDC Systems

2.1 Introduction

The design of a relaying algorithm for HVDC grids requires comprehensive understanding of the fault transient, which can be obtained by performing electromagnetic transient (EMT) simulations, frequency-domain analysis, or time-domain analysis on the equivalent models of HVDC grids. In the literature, various equivalent models of HVDC components are developed to achieve the fault-transient analysis in various levels of details.

An MMC can be built as a detailed model [22, 28], a continuous model [29], or a RLC branch [5, 30, 31]. The detailed MMC model is constructed with the the highest fidelity, where each SM and non-linear semiconductor device is individually modeled and controlled. For some highly detailed models, the temperature effect on semiconductors is even simulated. The detailed model enables the analysis in the level of devices, such as the behavior of an individual SM during a transient. However, the extensive appearance of nonlinear devices in the detailed model requires significant calculation resources and comprises the model's calculation efficiency. If only the analysis in the grid level is required, the MMC can be represent by a continuous model [29], which consists of a controlled voltage source with a few semiconductor switches. The continuous model is of high accuracy during the steady state, fault transient, and operation transient. Meanwhile, the simulation efficiency of the continuous model is significantly higher than that of the detailed model. If the analysis

only focuses on the period right after the fault (tens of milliseconds), a RLC branch with [30, 31] or without a controlled current source [5, 6] can be used to represent an MMC. The equivalent RLC branch significantly simplifies the MMC and enables the mathematical expression of the fault current right after a fault.

An transmission line can be represented by the frequency dependent (FD) model, the lumped Π model, or a RL branch. In the FD model, the line resistance, inductance, and capacitance are distributed along the transmission line, and the traveling-wave dispersion resulted from the different propagation speeds of traveling-waves with different frequencies is considered. The FD model is excellent in describing the traveling wave phenomenons during the transient, such as the propagation of fault current and the over voltage resulted from the reflected traveling waves between terminals. However, it is hard to use the FD model to analyze the fault transients in HVDC grids other than by using simulation tools. The lumped Π model, which represents a transmission line with a resister, an inductor, and two capacitors, enables a mathematical approach to describe the HVDC grid with impedance or conductance matrix. If a transmission line has small capacitance, e.g., an overhead line, this line can be further simplified as a RL model. Both the lumped Π model and the RL model provide the approach to mathematically express the fault current right after the fault occurrence with acceptable accuracy.

This chapter presents a set of matrix-form differential equations to calculate the fault current in HVDC grids right after a DC fault. The matrix-form differential equations can be easily built and are suitable for:

- various grid topologies, e.g., symmetric monopole, asymmetric monopole with ground or metallic return, and bipole with ground or metallic return;
- various fault scenarios, e.g., P2P, P2G, and pole-to-metallic (P2M) faults;
- grids with different types of MMCs, e.g., a grid with both FB-MMCs and HB-MMCs.

Section 2.2 introduces the test grid. Section 2.3 presents the matrix-form equations for various grid topologies and fault scenarios. Section 2.4 evaluates the accuracy of the developed calculation methods.

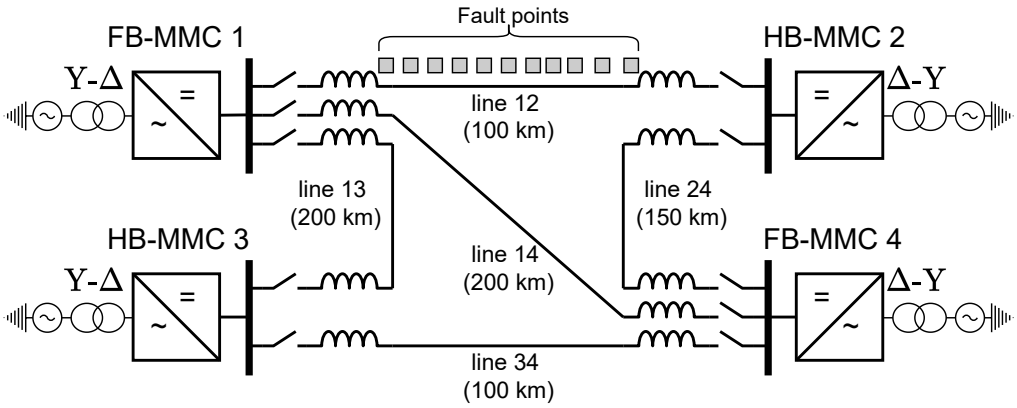

Figure 2.1: Four-terminal meshed HVDC test grid.

2.2 Test Grids

Five four-terminal meshed HVDC grids in different configurations—symmetric monopole, asymmetric monopole with ground or metallic return, and bipole with ground or metallic return—are tested in this chapter, Fig. 2.1. For each configuration, FB-MMCs are installed at terminals 1 and 4, and HB-MMCs are installed at terminals 2 and 3. The rated DC voltage of each MMC station is $V_{dc} = 640$ kV, i.e., the rated P2P voltage of the bipole grid is $2V_{dc}$.

For each configuration, the MMC is connected to the AC grid through a Δ-Y connected transformer, where Δ and Y are on MMC and AC sides, respectively [6]. For the symmetric monopole grid, each MMC is connected with grounding branches—three Y-connected inductors in series with a resistor—on the AC side and un-grounded on the DC side [4], Fig. 2.2. The asymmetric monopole and bipole grids have no grounding branch on the AC side and are low-impedance (10 Ω) grounded on the DC side. The asymmetric monopole grid uses the negative pole for transmission.

Transmission lines in test grids are overhead lines (OHLs), which are represented by RL branches [30] to simplify the calculation of fault currents. At both ends of a line, terminal inductors are implemented to limit the rising speed of the fault current [32]. Between each MMC and a terminal inductor, a hybrid DCCB is implemented. The hybrid DCCB model is presented by [33], which will open within 2 ms after receiving a trip signal generated by the relay. Between the two terminal inductors on each line, eleven fault points are equally distributed. These fault points will be used in Section 2.4.3. For the sake of simplicity, these fault points are only shown on line 12 in Fig. 2.1. The grid and converter parameters are shown in Table 2.1 [6].

Table 2.1: Converter and grid parameters

Items	Values
Converter stations	
AC grid voltage	400 kV
Nominal ratio of transformer	400 kV/380 kV
Transformer leakage inductance (u_k)	0.15 p.u.
Grounding inductance (l^{ac})	3 H
Grounding resistance (r^{ac})	1000 Ω
Dc grid rated voltage (V_{dc})	640 kV
Sub-module (SM) capacitance (c^{SM})	10000 μF
IGBT and diode on-state resistance (r_{ON})	5 mΩ
Arm inductance (l^{arm})	20 mH
Arm resistance (r^{arm})	0 Ω
Number of SMs per arm (N_{SM})	76
DC overhead lines	
Resistance per unit length	0.014 Ω/km
Inductance per unit length	0.82 mH/km
Terminal inductance (l^t)	50 mH
Control mode	
FB-MMC 1	V_{dc}=640 kV
HB-MMC 2	P=-900 MW
HB-MMC 3	P=-900 MW
FB-MMC 4	P=950 MW

2.3 Calculation of Fault-Current Derivatives

This section introduces a new methods to calculate the DC current right after a DC fault occurs in a multi-terminal HVDC grid. All of the grid topologies and fault scenarios are covered by the calculation methods. Namely, a P2G or P2P fault in a symmetric monopole grid, a P2G fault in an asymmetric monopole grid with ground return, a P2G or P2M fault in an asymmetric monopole grid with metallic return, a P2G or P2P fault in a bipole grid with ground return, and a P2G, P2M, or P2P fault in a bipole grid with metallic return are studied in this section. An advantage of the calculation methods is that the differential equations used for the calculation are all in the similar matrix forms, and these matrices can be easily built or modified once an HVDC grid is expanded or reconstructed

This section will introduce the calculation method for four typical fault scenarios—P2G and P2P faults in a symmetric monopole grid, a P2G fault in an asymmetric monopole grid with metallic return, and a P2M fault in a bipole grid with metallic return—and a uniform matrix-form equation with a table where matrices for all fault scenarios are listed. The equivalent MMC models are introduced in 2.3.1, and the current calculation method for the four fault scenarios is introduced in 2.3.2-2.3.6.

2.3.1 Equivalent MMCs right after a DC Fault

Right after a P2P fault, an MMC can be represented by an RLC branch [5], Fig. 2.2. After the fault occurrence and before the operation of the protection system (less than 10 ms), SM capacitors discharge rapidly and lead to large fault currents. Comparatively, currents from the AC side are small, so the AC side is not considered in this equivalent MMC model [5, 34]. Parameters of the equivalent MMC model are

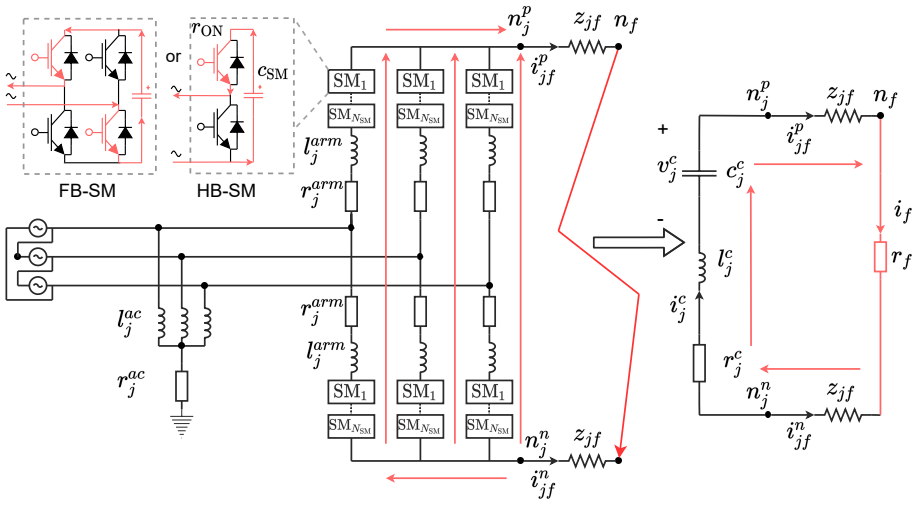

Figure 2.2: Equivalent MMC model right after a P2P fault [5].

expressed as (2.1) [5],

$$r_j^c = \frac{2(r_j^{arm} + N_{\mathrm{SM}} \frac{N_{\mathrm{sw}}}{2} r_{\mathrm{ON}})}{3}, \tag{2.1a}$$

$$l_j^c = \frac{2l_j^{arm}}{3}, \tag{2.1b}$$

$$c_j^c = \frac{6c_j^{\mathrm{SM}}}{N_{\mathrm{SM}}}, \tag{2.1c}$$

where r_j^{arm} and l_j^{arm} are arm resistance and inductance of MMC j, respectively; N_{SM} is the number of SMs in each arm; N_{sw} is the number of IGBTs in an SM, e.g., N_{sw} is 2 in a HB-SM and is 4 in an FB-SM; r_{ON} is the on-state resistance of an IGBT or diode; c_j^{SM} is the SM capacitance of MMC j; and r_j^c, l_j^c, and c_j^c are the equivalent resistance, inductance, and capacitance of MMC j, respectively.

Right after a P2G fault, an MMC can be represented by the aforementioned RLC branch with two equivalent grounding branches as shown in Fig. 2.3(b), the proof of which is expressed below [6].

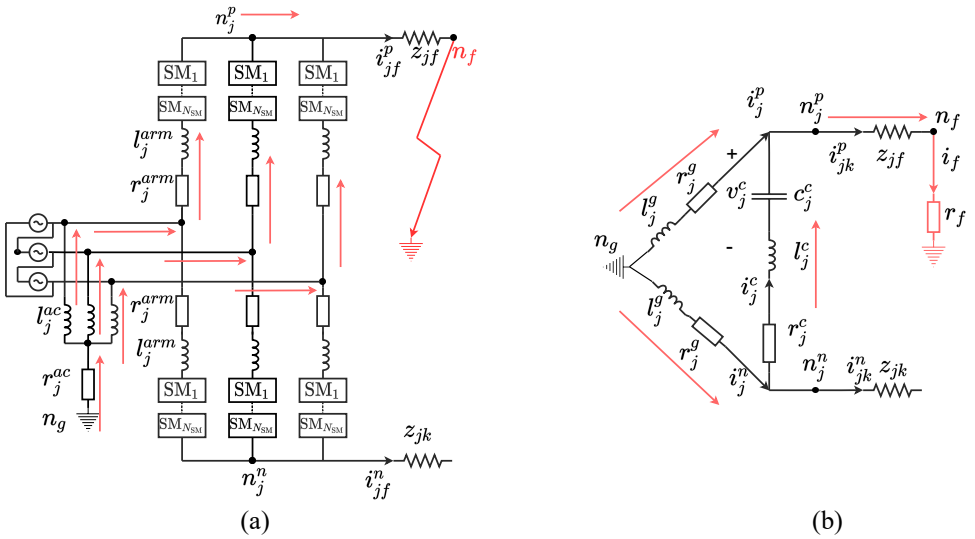

Figure 2.3: (a) Original and (b) equivalent circuits of an MMC right after a P2G fault [6].

According to the superposition principle, an MMC terminal during a P2G fault, Fig. 2.4(a), can be decomposed into a steady-state circuit, Fig. 2.4(c), and a fault circuit, Fig. 2.4(c). Since the Δ-connected transformer on the AC side cannot provide the unbalanced P2G fault current, the steady-state circuit can be neglected during the P2G-fault analysis.

Fig. 2.5(a) shows a single phase of the circuit in Fig. 2.4(c). Since the grounding impedance is much larger than the upper and lower arm impedances ($Z_j^g \gg Z_j^p$ and Z_j^n), the equivalent Δ-connected circuit in Fig. 2.5(b) can be approximated as (2.2) by employing the Y-Δ transform.

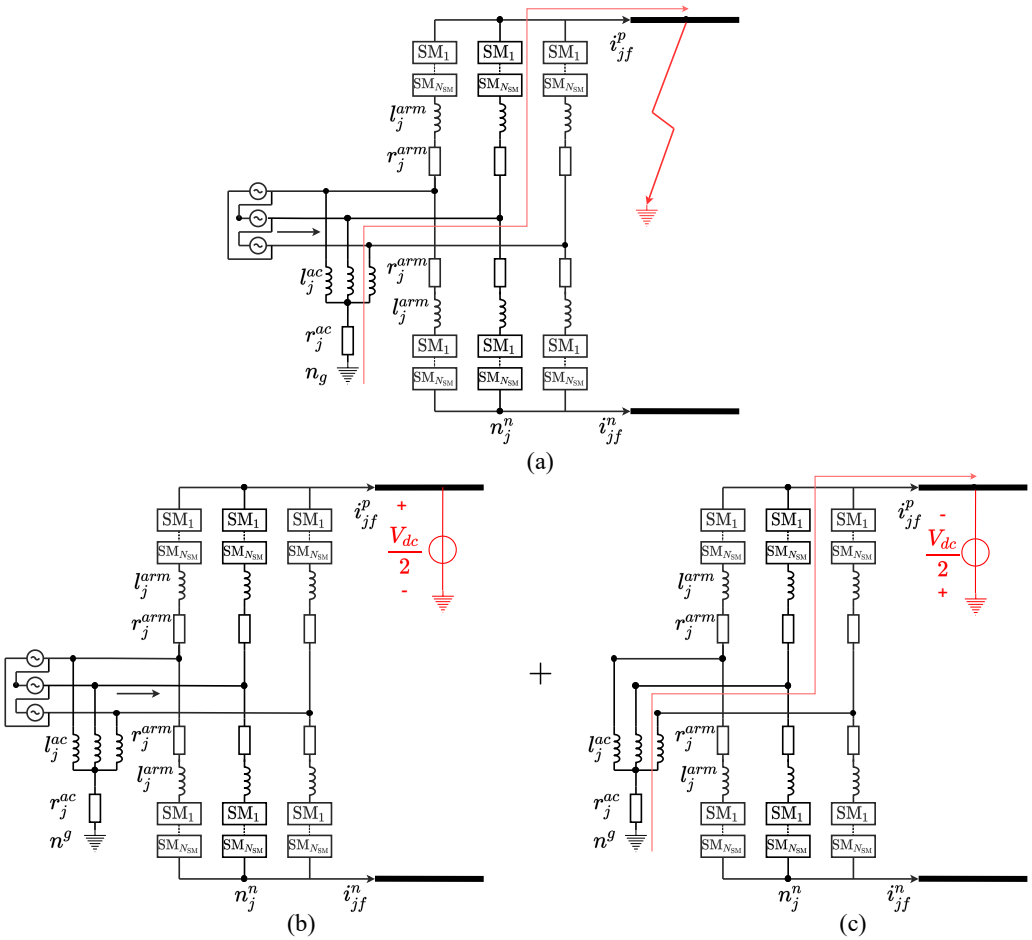

Figure 2.4: MMC circuit during a positive P2G fault: (a) original circuit; (b) steady-state circuit; and (c) fault circuit [6].

$$Z_j^{pg} = Z_j^g + Z_j^p + \frac{Z_j^g Z_j^p}{Z_j^n} \approx 2Z_j^g = j2\omega l_j^{ac} + 6r_j^{ac}, \tag{2.2a}$$

$$Z_j^{ng} = Z_j^g + Z_j^n + \frac{Z_j^g Z_j^n}{Z_j^p} \approx 2Z_j^g = j2\omega l_j^{ac} + 6r_j^{ac}, \tag{2.2b}$$

$$Z_j^{pn} = Z_j^p + Z_j^n + \frac{Z_j^p Z_j^n}{Z_j^g} \approx Z_j^p + Z_j^n = -j\frac{1}{\omega C_i} + j2\omega l_j^{arm} + 2r_j^{arm}, \tag{2.2c}$$

where Z_j^{pg}, Z_j^{ng}, and Z_j^{pn} are the equivalent impedances of the Δ-connected circuit

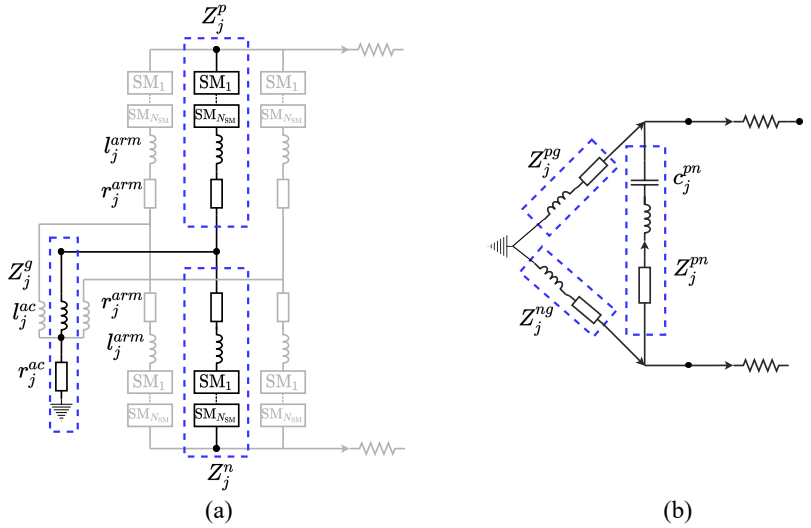

(a) (b)

Figure 2.5: (a) Circuit and (b) equivalent circuit for a single phase of an MMC [6].

in Fig. 2.5(b). c_j^{pn} can be calculated based on the energy balance principle [35, 36]:

$$\begin{cases} \frac{1}{2}c_j^{pn}V_{dc}^2 = 2N_{\text{SM}} \times \frac{1}{2}c^{\text{SM}}V_{\text{SM}}^2 \\ V_{dc} = N_{\text{SM}}V_{\text{SM}} \end{cases} \Rightarrow c_j^{pn} = \frac{2}{N_{\text{SM}}}c^{\text{SM}}. \tag{2.3}$$

The equivalent MMC during a P2G fault can be obtained by connecting three of the circuits shown in Fig. 2.5(b) in parallel. As a result, the parameters of the equivalent grounding branch are expressed as (2.4),

$$l_j^g = \frac{2l_j^{ac}}{3}, \tag{2.4a}$$

$$r_j^g = \frac{6r_j^{ac}}{3} = 2r_j^{ac}, \tag{2.4b}$$

where r_j^g and l_j^g are the equivalent resistance and inductance of the grounding branches for MMC j, respectively.

2.3.2 P2G Fault in the Symmetric Monopole Grid

Fig. 2.6 shows the equivalent test grid when a positive P2G fault occurs on line 12. Branch currents i_{jk}^p and i_{jk}^n are the positive and negative pole currents flowing from MMC j to MMC k, respectively. Branch currents of faulty lines are i_{1f}^p and i_{f2}^p, where f denotes the fault point. The capacitor current i_j^c is flowing from the

negative pole of MMC j to its positive pole. Ground currents i_j^p and i_j^n are flowing from the ground to positive and negative poles of MMC j, respectively. The voltage across c_j^c is v_j^c. Bold variables $\boldsymbol{i}^p$, $\boldsymbol{i}^n$, $\boldsymbol{i}^c$, and $\boldsymbol{v}^c$ represent column vectors of i_{jk}^p, i_{jk}^n, i_j^c, and v_j^c, respectively. Specifically, two faulty line currents form the last two elements of the current vector, i.e., $\boldsymbol{i}^p(5) = i_{1f}^p$ and $\boldsymbol{i}^p(6) = i_{f2}^p$ for the test grid.

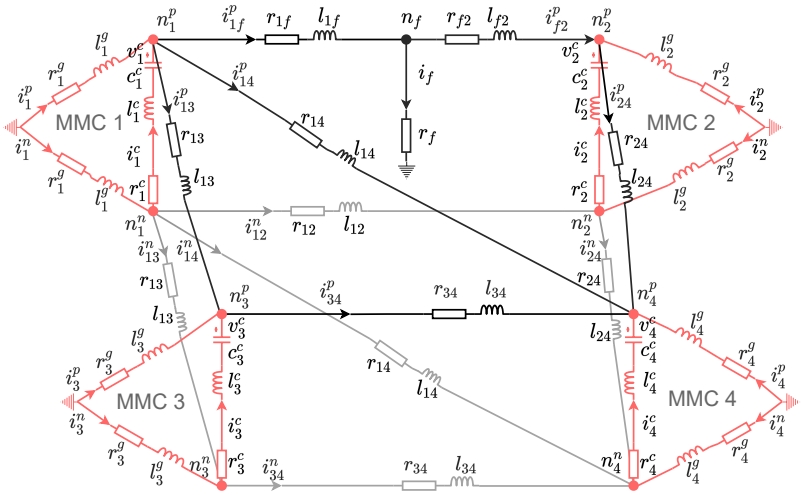

Figure 2.6: Equivalent model of the symmetric monopole test grid when a positive P2G fault occurs on line 12 [6].

For each current in $\boldsymbol{i}^p$, $\boldsymbol{i}^n$, and $\boldsymbol{i}^c$, a differential equation can be formed by employing KVL to the electrical path that the current passes. For example, equations for i_{34}^p, i_{1f}^p, i_{12}^n, and i_1^c is expressed in (2.5a), (2.5b), (2.5c), and (2.5d), respectively.

$$0 = r_3^g i_3^p + r_{34} i_{34}^p - r_4^g i_4^p + l_3^g \frac{\mathrm{d}i_3^p}{\mathrm{d}t} + l_{34} \frac{\mathrm{d}i_{34}^p}{\mathrm{d}t} - l_4^g \frac{\mathrm{d}i_4^p}{\mathrm{d}t}, \tag{2.5a}$$

$$0 = r_1^g i_1^p + r_{1f} i_{1f}^p + r_f i_f + l_1^g \frac{\mathrm{d}i_1^p}{\mathrm{d}t} + l_{1f} \frac{\mathrm{d}i_{1f}^p}{\mathrm{d}t}, \tag{2.5b}$$

$$0 = r_1^g i_1^n + r_{12} i_{12}^n - r_2^g i_2^n + l_1^g \frac{\mathrm{d}i_1^n}{\mathrm{d}t} + l_{12} \frac{\mathrm{d}i_{12}^n}{\mathrm{d}t} - l_2^g \frac{\mathrm{d}i_2^n}{\mathrm{d}t}, \tag{2.5c}$$

$$v_1^c = r_1^g i_1^n + r_1^c i_1^c - r_1^g i_1^p + l_1^g \frac{\mathrm{d}i_1^n}{\mathrm{d}t} + l_1^c \frac{\mathrm{d}i_1^c}{\mathrm{d}t} - l_1^g \frac{\mathrm{d}i_1^p}{\mathrm{d}t}. \tag{2.5d}$$

Each ground current can be replaced by the sum of certain currents in $\boldsymbol{i}^p$, $\boldsymbol{i}^n$, and $\boldsymbol{i}^c$. For example, $i_1^p = i_{1f}^p + i_{13}^p + i_{14}^p - i_1^c$, and $i_1^n = i_{12}^n + i_{13}^n + i_{14}^n + i_1^c$. Replacing ground

currents in (2.5a-2.5d) with currents in $\boldsymbol{i}^p$, $\boldsymbol{i}^n$, and $\boldsymbol{i}^c$ yields

$$\begin{aligned}
0 =& - r_3^g i_{13}^p + r_4^g i_{14}^p + r_4^g i_{24}^p + (r_{34} + r_3^g + r_4^g) i_{34}^p - r_3^g i_3^c + r_4^g i_4^c \\
& - l_3^g \frac{\mathrm{d}i_{13}^p}{\mathrm{d}t} + l_4^g \frac{\mathrm{d}i_{14}^p}{\mathrm{d}t} + l_4^g \frac{\mathrm{d}i_{24}^p}{\mathrm{d}t} + (l_{34} + l_3^g + l_4^g) \frac{\mathrm{d}i_{34}^p}{\mathrm{d}t} - l_3^g \frac{\mathrm{d}i_3^c}{\mathrm{d}t} + l_4^g \frac{\mathrm{d}i_4^c}{\mathrm{d}t}, \qquad (2.6a) \\
0 =& (r_{1f} + r_1^g + r_f) i_{1f}^p - r_f i_{f2}^p + r_1^g i_{13}^p + r_1^g i_{14}^p - r_1^g i_1^c \\
& + (l_{1f} + l_1^g) \frac{\mathrm{d}i_{1f}^p}{\mathrm{d}t} + l_1^g \frac{\mathrm{d}i_{13}^p}{\mathrm{d}t} + l_1^g \frac{\mathrm{d}i_{14}^p}{\mathrm{d}t} - l_1^g \frac{\mathrm{d}i_1^c}{\mathrm{d}t}, \qquad (2.6b) \\
0 =& r_1^g i_{13}^n + r_1^g i_{14}^n - r_2^g i_{24}^n + (r_{12} + r_1^g + r_2^g) i_{12}^n + r_1^g i_1^c - r_2^g i_2^c \\
& + l_1^g \frac{\mathrm{d}i_{13}^n}{\mathrm{d}t} + l_1^g \frac{\mathrm{d}i_{14}^n}{\mathrm{d}t} - l_2^g \frac{\mathrm{d}i_{24}^n}{\mathrm{d}t} + (l_{12} + l_1^g + l_2^g) \frac{\mathrm{d}i_{12}^n}{\mathrm{d}t} + l_1^g \frac{\mathrm{d}i_1^c}{\mathrm{d}t} - l_2^g \frac{\mathrm{d}i_2^c}{\mathrm{d}t}, \qquad (2.6c) \\
v_1^c =& - r_1^g (i_{1f}^p + i_{13}^p + i_{14}^p - i_{12}^n - i_{13}^n - i_{14}^n) + (r_1^c + 2r_1^g) i_1^c \\
& - l_1^g \frac{\mathrm{d}}{\mathrm{d}t} (i_{1f}^p + i_{13}^p + i_{14}^p - i_{12}^n - i_{13}^n - i_{14}^n) + (l_1^c + 2l_1^g) \frac{\mathrm{d}i_1^c}{\mathrm{d}t}. \qquad (2.6d)
\end{aligned}$$

2.3.2.1 The matrix-form representation of currents and voltages relationship

There are $2b+N+1$ currents in $\boldsymbol{i}^p$, $\boldsymbol{i}^n$, and $\boldsymbol{i}^c$ in total, where N is the number of MMC terminals, and b is the number of positive pole lines before the fault occurrence. The equations for all currents can be expressed in the matrix form,

$$\mathbf{A}_{pg} \cdot \boldsymbol{v}^c = \mathbf{R}_{pg} \cdot \boldsymbol{i} + \mathbf{L}_{pg} \cdot \frac{\mathrm{d}\boldsymbol{i}}{\mathrm{d}t}, \qquad (2.7)$$

where $\mathbf{A}_{pg} = [\mathbf{0}_{N,2b+1}, \mathbf{I}_N]^\top$, $\boldsymbol{i} = [\boldsymbol{i}^{p\top}, \boldsymbol{i}^{n\top}, \boldsymbol{i}^{c\top}]^\top$, and $\mathbf{I}_N$ is a $N \times N$ identity matrix. The first $b-1$ rows in (2.7) are in the form similar to (2.6a), and they correspond to the positive healthy pole currents. Likewise, the b_{th} to $(b+1)_{\text{th}}$, $(b+2)_{\text{th}}$ to $(2b+1)_{\text{th}}$, and $(2b+2)_{\text{th}}$ to $(2b+N+1)_{\text{th}}$ rows are in the forms similar to (2.6b), (2.6c), and (2.6d), respectively.

$\mathbf{R}_{pg}$ and $\mathbf{L}_{pg}$ are $(2b+N+1) \times (2b+N+1)$ resistance and inductance matrices, respectively. $\mathbf{R}_{pg}$ is expressed as

$$\mathbf{R}_{pg} = \begin{bmatrix} \mathbf{A}_f(\mathbf{R}^g + \mathbf{R}^f)\mathbf{A}_f^\top + \mathbf{R}_f^l & \mathbf{0}_{b+1,b} & -\mathbf{A}_f\mathbf{R}^g \\ \mathbf{0}_{b,b+1} & \mathbf{A}_0\mathbf{R}^g\mathbf{A}_0^\top + \mathbf{R}_0^l & \mathbf{A}_0\mathbf{R}^g \\ -\mathbf{R}^{g\top}\mathbf{A}_f^\top & \mathbf{R}^{g\top}\mathbf{A}_0^\top & \mathbf{R}^c + 2\mathbf{R}^g \end{bmatrix}, \qquad (2.8)$$

where $\mathbf{A}_0$ is the incidence matrix for the pre-fault grid which has a row for each transmission line and a column for each terminal [37]. $\mathbf{A}_f$ is the incidence matrix for the post-fault grid, which is formed by 1) splitting the row in $\mathbf{A}_0$ corresponding to the faulty line into two rows that contain a non-zero element, and 2) moving these

two rows to the bottom of $\mathbf{A}_0$. For example, $\mathbf{A}_0$ and $\mathbf{A}_f$ for the test grid during a P2G fault on line 12 are shown in (2.9).

$$\mathbf{A}_0 = \begin{bmatrix} 1 & -1 & 0 & 0 \\ 1 & 0 & -1 & 0 \\ 1 & 0 & 0 & -1 \\ 0 & 1 & 0 & -1 \\ 0 & 0 & 1 & -1 \end{bmatrix}, \quad \mathbf{A}_f = \begin{bmatrix} 1 & 0 & -1 & 0 \\ 1 & 0 & 0 & -1 \\ 0 & 1 & 0 & -1 \\ 0 & 0 & 1 & -1 \\ 1 & 0 & 0 & 0 \\ 0 & -1 & 0 & 0 \end{bmatrix}. \tag{2.9}$$

$\mathbf{R}^g$, $\mathbf{R}^c$, $\mathbf{R}_0^l$, and $\mathbf{R}_f^l$ are diagonal matrices with ground resistances, MMC equivalent resistances, line resistances of the pre-fault and post-fault grids on diagonals, respectively. The sequences of line resistances in $\mathbf{R}_0^l$ and $\mathbf{R}_f^l$ correspond to the sequences of lines in $\mathbf{A}_0$ and $\mathbf{A}_f$, respectively. $\mathbf{R}^f$ is the fault resistance matrix. For example, these matrices for the test grid are

$$\mathbf{R}^g = \mathrm{diag}(r_1^g, r_2^g, r_3^g, r_4^g), \tag{2.10a}$$
$$\mathbf{R}^c = \mathrm{diag}(r_1^c, r_2^c, r_3^c, r_4^c), \tag{2.10b}$$
$$\mathbf{R}_0^l = \mathrm{diag}(r_{12}, r_{13}, r_{14}, r_{24}, r_{34}), \tag{2.10c}$$
$$\mathbf{R}_f^l = \mathrm{diag}(r_{13}, r_{14}, r_{24}, r_{34}, r_{1f}, r_{f2}), \tag{2.10d}$$
$$\mathbf{R}^f = r_f \cdot \mathbf{1}_{4,4}, \tag{2.10e}$$

where $\mathbf{1}_{4,4}$ is a 4×4 all-ones matrix, and the diagonal function $\mathrm{diag}(\cdot)$ is defined in [38].

The structure of $\mathbf{L}_{pg}$ is the same as $\mathbf{R}_{pg}$, except all $\mathbf{R}$ and r in $\mathbf{R}_{pg}$ are replaced by $\mathbf{L}$ and l, respectively. Generally, $\mathbf{L}^f$ is a zero matrix.

The matrix form equation for all capacitor voltages is expressed as

$$\frac{\mathrm{d}\boldsymbol{v}}{\mathrm{d}t} = -\mathbf{E}^c \cdot \mathbf{A}_{pg}^\top \cdot \boldsymbol{i}, \tag{2.11}$$

where the elastance matrix $\mathbf{E}^c$ is a diagonal matrix with the reciprocal of each equivalent MMC's capacitance as the element,

$$\mathbf{E}^c = \mathrm{diag}(1/c_1^c, \cdots, 1/c_j^c, \cdots, 1/c_N^c. \tag{2.12}$$

Combining (2.7) and (2.11) yields the matrix-form equation for the P2G fault scenario,

$$\frac{\mathrm{d}}{\mathrm{d}t}\begin{bmatrix} \boldsymbol{i} \\ \boldsymbol{v} \end{bmatrix} = \begin{bmatrix} -\mathbf{L}_{pg}^{-1} \cdot \mathbf{R}_{pg} & \mathbf{L}_{pg}^{-1} \cdot \mathbf{A}_{pg} \\ \mathbf{E}_{pg} & \mathbf{0}_{N,N} \end{bmatrix} \cdot \begin{bmatrix} \boldsymbol{i} \\ \boldsymbol{v} \end{bmatrix}, \tag{2.13}$$

where $\mathbf{E}_{pg} = -\mathbf{E}^c \cdot \mathbf{A}_{pg}^\top$.

2.3.3 P2P Fault in the Symmetric Monopole Grid

Fig. 2.7 shows the equivalent model of the symmetric monopole test grid when a P2P fault occurs on line 12. The matrix-form equation for a P2P fault scenario is expressed as (2.14) [5].

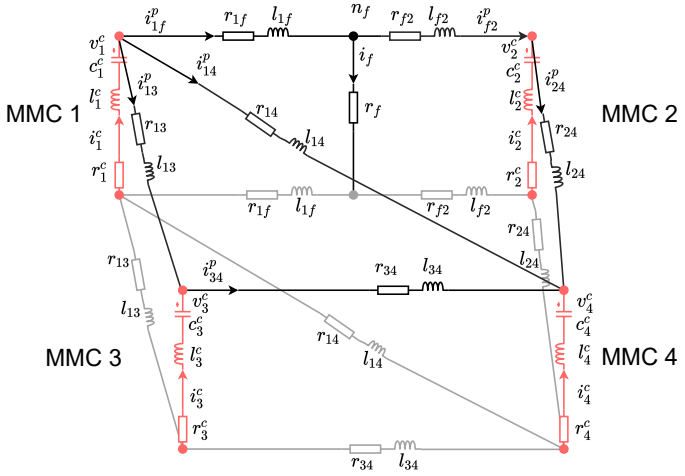

Figure 2.7: Equivalent model of the symmetric monopole test grid when a P2P fault occurs on line 12.

$$\frac{\mathrm{d}}{\mathrm{d}t}\begin{bmatrix}\boldsymbol{i}^p\\ \boldsymbol{v}^c\end{bmatrix} = \begin{bmatrix}-\mathbf{L}_{pp}^{-1}\cdot\mathbf{R}_{pp} & \mathbf{L}_{pp}^{-1}\cdot\mathbf{A}_{pp}\\ \mathbf{E}_{pp} & \mathbf{0}_{N,N}\end{bmatrix}\cdot\begin{bmatrix}\boldsymbol{i}^p\\ \boldsymbol{v}^c\end{bmatrix}. \tag{2.14}$$

$\mathbf{R}_{pp}$ and $\mathbf{L}_{pp}$ are $(b+1)\times(b+1)$ resistance and inductance matrices, respectively. $\mathbf{E}_{pp}$ is a $N\times(b+1)$ elastance matrix.

$$\mathbf{A}_{pp} = \mathbf{A}_f, \tag{2.15a}$$
$$\mathbf{R}_{pp} = \mathbf{A}_f(\mathbf{R}^c+\mathbf{R}^f)\mathbf{A}_f^\top + 2\mathbf{R}_f^l, \tag{2.15b}$$
$$\mathbf{L}_{pp} = \mathbf{A}_f\mathbf{L}^c\mathbf{A}_f^\top + 2\mathbf{L}_f^l, \tag{2.15c}$$
$$\mathbf{E}_{pp} = -\mathbf{E}^c\cdot\mathbf{A}_{pp}^\top. \tag{2.15d}$$

$\mathbf{A}_f$, $\mathbf{R}^c$, $\mathbf{R}^f$, $\mathbf{R}_f^l$, $\mathbf{L}^c$, $\mathbf{L}_f^l$, and $\mathbf{E}^c$ are the same as expressed previously.

2.3.4 P2G fault in the Asymmetric Monopole Grid with Metallic Return

The equivalent circuit when a negative P2G fault occurs on line 12 in the asymmetric monopole test grid with metallic return is shown in Fig. 2.8. Since each MMC

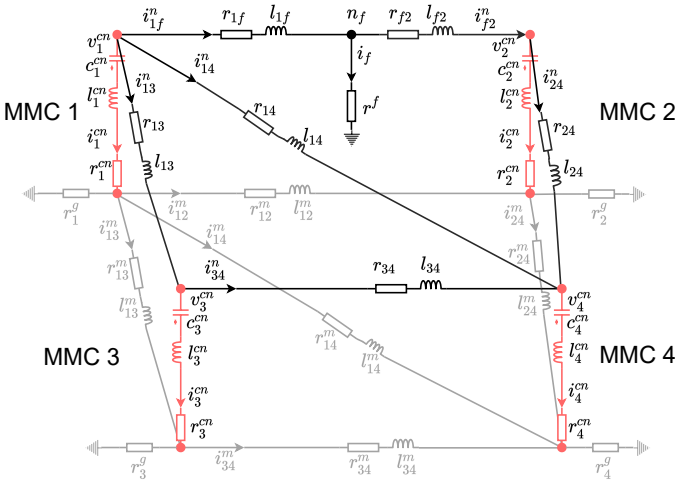

Figure 2.8: Equivalent model of the asymmetric monopole test grid with metallic return when a positive P2G fault occurs on line 12.

connects the neutral point with the negative pole, the voltage of the equivalent capacitor of MMC j is denoted as v_j^{cn}, the positive direction of which is from the neutral point to the negative pole, Fig. 2.8. The voltage vector, MMC current vector, MMC resistance matrix, MMC inductance matrix, and MMC conductance matrix are denoted as $\boldsymbol{v}^{cn}$, $\boldsymbol{i}^{cn}$, $\mathbf{R}^{cn}$, $\mathbf{L}^{cn}$, and $\mathbf{E}^{cn}$, respectively. The vector $\boldsymbol{i}^m$ consists of each current on the metallic return line. The matrices $\mathbf{R}_0^m$ and $\mathbf{L}_0^m$ are similar to $\mathbf{R}_0^l$ and $\mathbf{L}_0^l$, respectively, except that $\mathbf{R}_0^m$ and $\mathbf{L}_0^m$ correspond to the metallic return lines. For example, $\boldsymbol{i}^m$ and $\mathbf{R}_0^m$ for the asymmetric monopole test grid with metallic return are expressed as

$$\boldsymbol{i}^m = [i_{12}^m, i_{13}^m, i_{14}^m, i_{24}^m, i_{34}^m]^\top, \tag{2.16a}$$

$$\mathbf{R}_0^m = \mathrm{diag}(r_{12}^m, r_{13}^m, r_{14}^m, r_{24}^m, r_{34}^m). \tag{2.16b}$$

$\mathbf{R}^g$ and $\mathbf{L}^g$ are still diagonal matrices consisting of the grounding resistance and grounding inductance at each terminal, respectively. If MMC j is ungrounded, r_j^g and l_j^g should be set at a very large value, e.g., 100 times larger than the maximum line resistance and inductance, respectively.

The matrix-form equation for this scenario is express as

$$\frac{\mathrm{d}}{\mathrm{d}t}\begin{bmatrix}\boldsymbol{i}\\ \boldsymbol{v}^{cn}\end{bmatrix} = \begin{bmatrix}-\mathbf{L}_{pg}^{-1}\cdot\mathbf{R}_{pg} & -\mathbf{L}_{pg}^{-1}\cdot\mathbf{A}_{pg}\\ -\mathbf{E}_{pg} & \mathbf{0}_{N,N}\end{bmatrix}\cdot\begin{bmatrix}\boldsymbol{i}\\ \boldsymbol{v}^{cn}\end{bmatrix}, \tag{2.17}$$

where

$$\boldsymbol{i} = [\boldsymbol{i}^{n\top}, \boldsymbol{i}^{m\top}]^\top, \tag{2.18a}$$

$$\mathbf{A}_{pg} = [\mathbf{A}_f^\top, \mathbf{0}_{N,b}]^\top, \tag{2.18b}$$

$$\mathbf{R}_{pg} = \begin{bmatrix} \mathbf{A}_f(\mathbf{R}^{cn} + \mathbf{R}^g + \mathbf{R}^f)\mathbf{A}_f^\top + \mathbf{R}_f^l & \mathbf{A}_f\mathbf{R}^g\mathbf{A}_0^\top \\ \mathbf{A}_0\mathbf{R}^g\mathbf{A}_f^\top & \mathbf{A}_0\mathbf{R}^g\mathbf{A}_0^\top + \mathbf{R}_0^m \end{bmatrix}, \tag{2.18c}$$

$$\mathbf{L}_{pg} = \begin{bmatrix} \mathbf{A}_f(\mathbf{L}^{cn} + \mathbf{L}^g)\mathbf{A}_f^\top + \mathbf{L}_f^l & \mathbf{A}_f\mathbf{L}^g\mathbf{A}_0^\top \\ \mathbf{A}_0\mathbf{L}^g\mathbf{A}_f^\top & \mathbf{A}_0\mathbf{L}^g\mathbf{A}_0^\top + \mathbf{L}_0^m \end{bmatrix}, \tag{2.18d}$$

$$\mathbf{E}_{pg} = -\mathbf{E}^{cn} \cdot \mathbf{A}_{pg}^\top. \tag{2.18e}$$

If the test grid is low-resistance grounded at one MMC terminal and ungrounded at other terminals, the earth current during normal operation will be small, but P2G faults far away from the grounding terminal can be hardly detected. If one terminal is low-resistance grounded and others are high-resistance grounded, the earth current during normal operation will be small, and P2G faults far away from the low-resistance grounded terminal can be detected easily.

2.3.5 P2M fault in the Bipole Grid with Metallic Return

The equivalent circuit when a fault occurs on line 12 in the bipole test grid with metallic return is shown in Fig. 2.9. In this fault scenario, the P2M fault branch is considered as a virtual MMC with an equivalent resistance of r_f, zero inductance, no capacitance, ground resistance of r_f^g, and ground inductance of l_f^g, where r_f^g and l_f^g are arbitrary large values that are 100 times larger than the maximum line resistance and inductance, respectively.

Since the fault branch is considered as a virtual MMC branch, one more column will be added to $\mathbf{A}_0$ and $\mathbf{A}_f$, and one more diagonal element will be added to $\mathbf{R}^{cp}$, $\mathbf{R}^{cn}$, $\mathbf{R}^g$, $\mathbf{L}^{cp}$, $\mathbf{L}^{cn}$, $\mathbf{L}^g$, $\mathbf{E}^{cp}$, and $\mathbf{E}^{cn}$, where $\mathbf{R}^{cp}$, $\mathbf{L}^{cp}$, and $\mathbf{E}^{cp}$ are resistance matrix, inductance matrix, and conductance matrix of the equivalent MMCs connected to the positive pole, respectively. $\boldsymbol{v}^{cp}$ is the voltage vector of the equivalent MMCs connected to the positive pole. A star marker (*) will be added to the superscript of each matrix that is modified for the virtual MMC branch. For example, the modified matrices $\mathbf{A}_0^*$, $\mathbf{A}_f^*$, $\mathbf{R}^{cp*}$, $\mathbf{R}^{g*}$, and $\mathbf{E}^{cp*}$ for the bipole test grid with metallic return

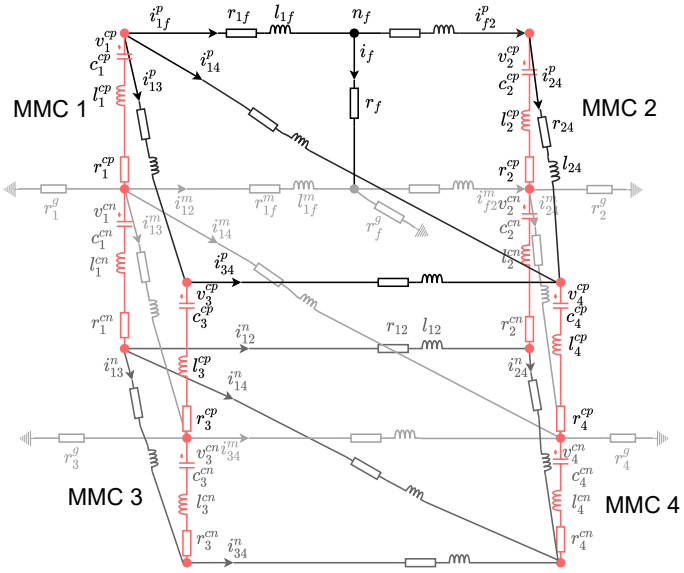

Figure 2.9: Equivalent model of the bipole test grid with metallic return when a positive P2M fault occurs on line 12.

are expressed as

$$\mathbf{A}_0^* = \begin{bmatrix} 1 & -1 & 0 & 0 & 0 \\ 1 & 0 & -1 & 0 & 0 \\ 1 & 0 & 0 & -1 & 0 \\ 0 & 1 & 0 & -1 & 0 \\ 0 & 0 & 1 & -1 & 0 \end{bmatrix}, \tag{2.19a}$$

$$\mathbf{A}_f^* = \begin{bmatrix} 1 & 0 & -1 & 0 & 0 \\ 1 & 0 & 0 & -1 & 0 \\ 0 & 1 & 0 & -1 & 0 \\ 0 & 0 & 1 & -1 & 0 \\ 1 & 0 & 0 & 0 & -1 \\ 0 & -1 & 0 & 0 & 1 \end{bmatrix}, \tag{2.19b}$$

$$\mathbf{R}^{cp*} = \mathrm{diag}(r_1^{cp}, r_2^{cp}, r_3^{cp}, r_4^{cp}, r_f), \tag{2.19c}$$

$$\mathbf{R}^{g*} = \mathrm{diag}(r_1^{g}, r_2^{g}, r_3^{g}, r_4^{g}, r_f^{g}), \tag{2.19d}$$

$$\mathbf{E}^{cp*} = \mathrm{diag}(\frac{1}{c_1^{cp}}, \frac{1}{c_2^{cp}}, \frac{1}{c_3^{cp}}, \frac{1}{c_4^{cp}}, 0). \tag{2.19e}$$

$$\tag{2.19f}$$

The matrix-form equation for the bipole grid is express as

$$\frac{\mathrm{d}}{\mathrm{d}t}\begin{bmatrix} \boldsymbol{i} \\ \boldsymbol{v} \end{bmatrix} = \begin{bmatrix} -\mathbf{L}_{pm}^{-1} \cdot \mathbf{R}_{pm} & \mathbf{L}_{pm}^{-1} \cdot \mathbf{A}_{pm} \\ \mathbf{E}_{pm} & \mathbf{0}_{2N+2,2N+2} \end{bmatrix} \cdot \begin{bmatrix} \boldsymbol{i} \\ \boldsymbol{v} \end{bmatrix}, \tag{2.20}$$

where

$$\boldsymbol{i} = [\boldsymbol{i}^{p\top}, \boldsymbol{i}^{m\top}, \boldsymbol{i}^{n\top}]^\top, \tag{2.21a}$$

$$\boldsymbol{v} = [\boldsymbol{v}^{cp\top}, 0, -\boldsymbol{v}^{cn\top}, 0]^\top, \tag{2.21b}$$

$$\mathbf{A}_{pm} = \begin{bmatrix} \mathbf{A}_f^* & \mathbf{0}_{b+1,N+1} \\ \mathbf{0}_{b+1,N+1} & \mathbf{0}_{b+1,N+1} \\ \mathbf{0}_{b,N+1} & \mathbf{A}_0^* \end{bmatrix}, \tag{2.21c}$$

$$\mathbf{R}_{pm} = \begin{bmatrix} \mathbf{A}_f^*(\mathbf{R}^{cp*} + \mathbf{R}^{g*})\mathbf{A}_f^{*\top} + \mathbf{R}_f^l & \mathbf{A}_f^*\mathbf{R}^{g*}\mathbf{A}_f^{*\top} & \mathbf{A}_f^*\mathbf{R}^{g*}\mathbf{A}_0^{*\top} \\ \mathbf{A}_f^*\mathbf{R}^{g*}\mathbf{A}_f^{*\top} & \mathbf{A}_f^*\mathbf{R}^{g*}\mathbf{A}_f^{*\top} + \mathbf{R}_f^m & \mathbf{A}_f^*\mathbf{R}^{g*}\mathbf{A}_0^{*\top} \\ \mathbf{A}_0^*\mathbf{R}^{g*}\mathbf{A}_f^{*\top} & \mathbf{A}_0^*\mathbf{R}^{g*}\mathbf{A}_f^{*\top} & \mathbf{A}_0^*(\mathbf{R}^{cn*} + \mathbf{R}^{g*})\mathbf{A}_0^{*\top} + \mathbf{R}_0^l \end{bmatrix}, \tag{2.21d}$$

$$\mathbf{E}_{pm} = -\begin{bmatrix} \mathbf{E}^{cp} & \mathbf{0}_{N+1,N+1} \\ \mathbf{0}_{N+1,N+1} & \mathbf{E}^{cn} \end{bmatrix} \cdot \mathbf{A}_{pm}^\top. \tag{2.21e}$$

$\mathbf{L}_{pm}$ is the same as $\mathbf{R}_{pm}$, except that r and $\mathbf{R}$ are replaced by l and $\mathbf{L}$.

2.3.6 Uniform Matrix-Form Equations for Current Calculation

The uniform expression of the differential equation for current calculation is

$$\frac{\mathrm{d}}{\mathrm{d}t}\begin{bmatrix} \boldsymbol{i} \\ \boldsymbol{v} \end{bmatrix} = \begin{bmatrix} -\mathbf{L}^{-1}\cdot\mathbf{R} & \mathbf{L}^{-1}\cdot\mathbf{A} \\ \mathbf{E} & \mathbf{0} \end{bmatrix} \cdot \begin{bmatrix} \boldsymbol{i} \\ \boldsymbol{v} \end{bmatrix}. \tag{2.22}$$

For each grid topology and fault type, the corresponding $\boldsymbol{i}$, $\boldsymbol{v}$, $\mathbf{L}$, $\mathbf{R}$, $\mathbf{A}$, and $\mathbf{E}$ can be found in Table 2.2.

For the matrices listed in Table 2.2, $\mathbf{R}^c$, $\mathbf{R}^{cp}$, $\mathbf{R}^{cn}$, $\mathbf{L}^c$, $\mathbf{L}^{cp}$, $\mathbf{L}^{cn}$, $\mathbf{E}^c$, $\mathbf{E}^{cp}$, $\mathbf{E}^{cn}$, and $\mathbf{R}^g$ are determined by the the number of MMC terminals, MMC parameters, and the grounding configuration of each MMC terminal; $\mathbf{A}_0$, $\mathbf{R}_0^l$, $\mathbf{R}_0^m$, $\mathbf{L}_0^l$, and $\mathbf{L}_0^m$ are determined by the grid structure and line parameters; $\mathbf{A}_f$, $\mathbf{R}_f^l$, $\mathbf{R}_f^m$, $\mathbf{L}_f^l$, and $\mathbf{L}_f^m$ are determined by the grid structure, line parameters, the faulty line, and the fault position on the line; $\mathbf{R}^f$ is determined by the fault resistance and the number of MMC terminals in the grid. The modified matrices $\mathbf{A}_0^*$, $\mathbf{A}_f^*$, $\mathbf{R}^{g*}$, $\mathbf{R}_0^{cp*}$, $\mathbf{R}_0^{cn*}$, $\mathbf{L}_0^{cp*}$, and $\mathbf{L}_0^{cn*}$ are only used in the P2M fault scenario in a bipole grid with metallic return. None of the aforementioned matrices depend on the fault type.

The negative P2M fault in a bipole grid with metallic return and the negative P2G faults in a symmetric monopole grid, bipole grid with ground return, and bipole grid with metallic return are similar to their corresponding positive ones. For the sake of clarity, the aforementioned negative faults are not presented in Table 2.2.

Table 2.2: Matrix-form equations for all fault scenarios.

	Symmetric monopole Positive P2G	P2P	Asymmetric monopole with ground return Negative P2G	Asymmetric monopole with metallic return Negative P2M
$\boldsymbol{i}$	$[\boldsymbol{i}^{p\top}, \boldsymbol{i}^{n\top}, \boldsymbol{i}^{c\top}]^\top$	$\boldsymbol{i}^{p}$	$\boldsymbol{i}^{n}$	$\boldsymbol{i}^{n}$
$\boldsymbol{v}$	$\boldsymbol{v}^{c}$	$\boldsymbol{v}^{c}$	$-\boldsymbol{v}^{cn}$	$-\boldsymbol{v}^{cn}$
$\mathbf{A}$	$[\mathbf{0}_{N,2b+1}, \mathbf{I}_N]^\top$	$\mathbf{A}_f$	$\mathbf{A}_f$	$\mathbf{A}_f$
$\mathbf{R}$	$\begin{bmatrix} \mathbf{A}_f(\mathbf{R}^g+\mathbf{R}^f)\mathbf{A}_f^\top+\mathbf{R}_f^l & \mathbf{0}_{b+1,b} & -\mathbf{A}_f\mathbf{R}^g \\ \mathbf{0}_{b,b+1} & \mathbf{A}_0\mathbf{R}^g\mathbf{A}_0^\top+\mathbf{R}_0^l & \mathbf{A}_0\mathbf{R}^g \\ -\mathbf{R}^{g\top}\mathbf{A}_f^\top & \mathbf{R}^{g\top}\mathbf{A}_0^\top & \mathbf{R}^c+2\mathbf{R}^g \end{bmatrix}$	$\mathbf{A}_f(\mathbf{R}^c+\mathbf{R}^f)\mathbf{A}_f^\top+2\mathbf{R}_f^l$	$\mathbf{A}_f(\mathbf{R}^c+\mathbf{R}^g+\mathbf{R}^f)\mathbf{A}_f^\top+\mathbf{R}_f^l$	$\mathbf{A}_f(\mathbf{R}^c+\mathbf{R}^f)$
$\mathbf{E}$	$-\mathbf{E}^c\cdot\mathbf{A}^\top$	$-\mathbf{E}^c\cdot\mathbf{A}^\top$	$-\mathbf{E}^{cn}\cdot\mathbf{A}^\top$	$-\mathbf{E}^{cn}\cdot\mathbf{A}^\top$
$\mathbf{0}$	$\mathbf{0}_{N,N}$	$\mathbf{0}_{N,N}$	$\mathbf{0}_{N,N}$	$\mathbf{0}_{N,N}$

	Asymmetric monopole with metallic return Negative P2G	Bipole with ground return Positive P2G	P2P	Bipole with metallic return P2P
$\boldsymbol{i}$	$[\boldsymbol{i}^{n\top}, \boldsymbol{i}^{m\top}]^\top$	$\boldsymbol{i}^{p}$	$\boldsymbol{i}^{p}$	$\boldsymbol{i}^{p}$
$\boldsymbol{v}$	$-\boldsymbol{v}^{cn}$	$\boldsymbol{v}^{cp}$	$\boldsymbol{v}^{cp}+\boldsymbol{v}^{cn}$	$\boldsymbol{v}^{cp}+\boldsymbol{v}^{cn}$
$\mathbf{A}$	$[\mathbf{A}_f^\top, \mathbf{0}_{N,b}]^\top$	$\mathbf{A}_f$	$\mathbf{A}_f$	$\mathbf{A}_f$
$\mathbf{R}$	$\begin{bmatrix} \mathbf{A}_f(\mathbf{R}^c+\mathbf{R}^g+\mathbf{R}^f)\mathbf{A}_f^\top+\mathbf{R}_f^l & \mathbf{A}_f\mathbf{R}^g\mathbf{A}_0^\top \\ \mathbf{A}_0\mathbf{R}^g\mathbf{A}_f^\top & \mathbf{A}_0\mathbf{R}^g\mathbf{A}_0^\top+\mathbf{R}_0^m \end{bmatrix}$	$\mathbf{A}_f(\mathbf{R}^{cp}+\mathbf{R}^g+\mathbf{R}^f)\mathbf{A}_f^\top+\mathbf{R}_f^l$	$\mathbf{A}_f(\mathbf{R}^{cp}+\mathbf{R}^{cn}+\mathbf{R}^f)\mathbf{A}_f^\top+2\mathbf{R}_f^l$	$\mathbf{A}_f(\mathbf{R}^{cp}+\mathbf{R}^{cn}+\mathbf{R}^f)\mathbf{A}_f^\top+2\mathbf{R}_f^l$
$\mathbf{E}$	$-\mathbf{E}^{cn}\cdot\mathbf{A}^\top$	$-\mathbf{E}^{cp}\cdot\mathbf{A}^\top$	$-(\mathbf{E}^{cp}+\mathbf{E}^{cn})\cdot\mathbf{A}^\top$	$-(\mathbf{E}^{cp}+\mathbf{E}^{cn})\cdot\mathbf{A}^\top$
$\mathbf{0}$	$\mathbf{0}_{N,N}$	$\mathbf{0}_{N,N}$	$\mathbf{0}_{N,N}$	$\mathbf{0}_{N,N}$

	Bipole with metallic return Positive P2M	Positive P2G
$\boldsymbol{i}$	$[\boldsymbol{i}^{p\top}, \boldsymbol{i}^{m\top}, \boldsymbol{i}^{n\top}]^\top$	$[\boldsymbol{i}^{p\top}, \boldsymbol{i}^{m\top}, \boldsymbol{i}^{n\top}]^\top$
$\boldsymbol{v}$	$[\boldsymbol{v}^{cp\top}, 0, -\boldsymbol{v}^{cn\top}, 0]^\top$	$[\boldsymbol{v}^{cp\top}, -\boldsymbol{v}^{cn\top}]^\top$
$\mathbf{A}$	$\begin{bmatrix} \mathbf{A}_f^* & \mathbf{0}_{b+1,N+1} \\ \mathbf{0}_{b+1,N+1} & \mathbf{0}_{b+1,N+1} \\ \mathbf{0}_{b,N+1} & \mathbf{A}_0^* \end{bmatrix}$	$\begin{bmatrix} \mathbf{A}_f & \mathbf{0}_{b+1,N} \\ \mathbf{0}_{b,N} & \mathbf{0}_{b,N} \\ \mathbf{0}_{b,N} & \mathbf{A}_0 \end{bmatrix}$
$\mathbf{R}$	$\begin{bmatrix} \mathbf{A}_f^*(\mathbf{R}^{cp*}+\mathbf{R}^{g*})\mathbf{A}_f^{*\top}+\mathbf{R}_f^l & \mathbf{A}_f^*\mathbf{R}^{g*}\mathbf{A}_f^{*\top} & \mathbf{A}_f^*\mathbf{R}^{g*}\mathbf{A}_0^{*\top} \\ \mathbf{A}_f^*\mathbf{R}^{g*}\mathbf{A}_f^{*\top} & \mathbf{A}_f^*\mathbf{R}^{g*}\mathbf{A}_f^{*\top}+\mathbf{R}_f^m & \mathbf{A}_f^*\mathbf{R}^{g*}\mathbf{A}_0^{*\top} \\ \mathbf{A}_0^*\mathbf{R}^{g*}\mathbf{A}_f^{*\top} & \mathbf{A}_0^*\mathbf{R}^{g*}\mathbf{A}_f^{*\top} & \mathbf{A}_0^*(\mathbf{R}^{cn*}+\mathbf{R}^{g*})\mathbf{A}_0^{*\top}+\mathbf{R}_0^l \end{bmatrix}$	$\begin{bmatrix} \mathbf{A}_f(\mathbf{R}^{cp}+\mathbf{R}^g+\mathbf{R}^f)\mathbf{A}_f^\top+\mathbf{R}_f^l & \mathbf{A}_f\mathbf{R}^g\mathbf{A}_0^\top & \mathbf{A}_f\mathbf{R}^g\mathbf{A}_0^\top \\ \mathbf{A}_0\mathbf{R}^g\mathbf{A}_f^\top & \mathbf{A}_0\mathbf{R}^g\mathbf{A}_0^\top+\mathbf{R}_0^m & \mathbf{A}_0\mathbf{R}^g\mathbf{A}_0^\top \\ \mathbf{A}_0\mathbf{R}^g\mathbf{A}_f^\top & \mathbf{A}_0\mathbf{R}^g\mathbf{A}_0^\top & \mathbf{A}_0(\mathbf{R}^g+\mathbf{R}^{cn})\mathbf{A}_0^\top+\mathbf{R}_0^l \end{bmatrix}$
$\mathbf{E}$	$-\begin{bmatrix} \mathbf{E}^{cp*} & \mathbf{0}_{N+1,N+1} \\ \mathbf{0}_{N+1,N+1} & \mathbf{E}^{cn*} \end{bmatrix}\cdot\mathbf{A}^\top$	$-\begin{bmatrix} \mathbf{E}^{cp} & \mathbf{0}_{N,N} \\ \mathbf{0}_{N,N} & \mathbf{E}^{cn} \end{bmatrix}\cdot\mathbf{A}^\top$
$\mathbf{0}$	$\mathbf{0}_{2N+2,2N+2}$	$\mathbf{0}_{2N,2N}$
$\mathbf{R}^{cp*}$	$\mathrm{diag}(r_1^{cp},\cdots,r_N^{cp},r_f)$	
$\mathbf{R}^{g*}$	$\mathrm{diag}(r_1^{g},\cdots,r_N^{g},r_f^{g})$	
$\mathbf{E}^{cp*}$	$\mathrm{diag}(1/c_1^{cp},\cdots,1/c_N^{cp},0)$	
$\mathbf{A}_0^*$	$[\mathbf{A}_0, \mathbf{0}_{b,1}]$	
$\mathbf{A}_f^*$	$\begin{bmatrix} \mathbf{A}_f, & \begin{bmatrix} \mathbf{0}_{b-1,1} \\ -1 \\ 1 \end{bmatrix} \end{bmatrix}$	

2.4 Simulations

This section validates the accuracy of the current calculation method by comparing the calculated current derivatives with the simulated ones. Hybrid four-terminal HVDC grids in different configurations are modeled in PSCAD/EMTDC. Three fault scenarios—P2G and P2P faults in the symmetric monopole grid and a P2P fault in the bipole grid with metallic return—are studied in this section. The fault impedance varies from 0.01 Ω to 500 Ω.

2.4.1 P2P fault in a symmetric monopole grid

Since P2P faults are generally of low resistance in a symmetric monopole grid [39], a P2P fault with a resistance of 0.01 Ω is applied to line 12 near terminal 1. Fig. 2.10 shows current derivatives within 3 ms after the P2P fault that occurs at $t = 0$ ms. Only 3 ms is shown in Fig. 2.10 because this period is long enough for relays to detect the fault [40]. The simulated current derivatives contain significant oscillations, which are caused by the high operating frequency of MMCs. However, these oscillations do not affect relays' normal operation because oscillations are relatively small compared to current derivatives caused by the fault. Fig. 2.10 shows that the calculation results are accurate for both healthy and faulty line currents.

2.4.2 P2G fault in a symmetric monopole grid

Eleven fault points are equally distributed between the two terminal inductors on line 12. The fault point $d = 0$ indicates the fault close to MMC 1; and $d = 1$ indicates the fault close to MMC 2. For each fault point, a positive P2G fault with a resistance of 500 Ω is employed, and the initial current derivative of each line is obtained. The simulated and calculated initial current derivatives corresponding to each fault point are plotted in Fig. 2.11, where i'_{jk} represents $\left|\frac{\mathrm{d}i^p_{jk}}{\mathrm{d}t}_0 + \frac{\mathrm{d}i^n_{jk}}{\mathrm{d}t}_0\right|$. Fig. 2.11 shows that for each fault point on line 12, the calculation method can provide an accurate estimation of the current derivative. Meanwhile, the initial derivatives of faulty line currents are far larger than those of healthy line currents, making it possible to determine a secure and dependable threshold to detect faults and identify the fault location in symmetric monopole grids.

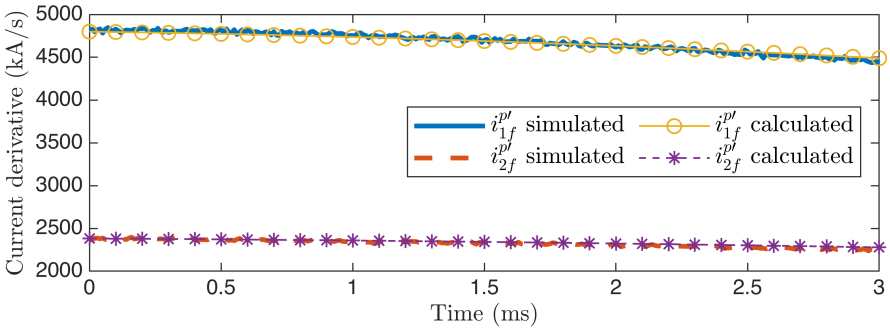

(a)

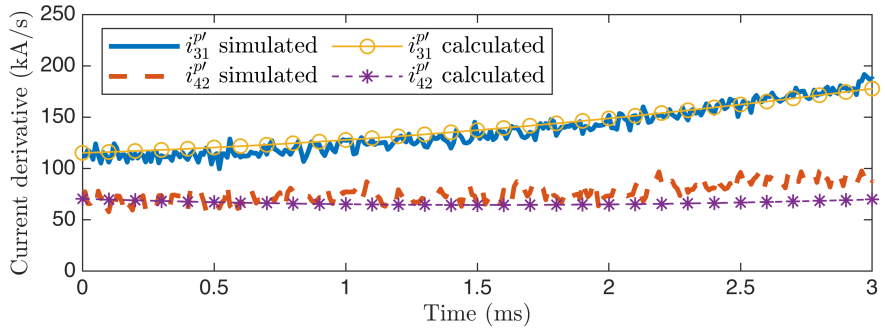

(b)

Figure 2.10: (a) Faulty, and (b) healthy line current derivatives during a P2P fault on line 12 near MMC 1 in a symmetric monopole grid ($r_f = 0.01\,\Omega$).

2.4.3 P2P fault in a bipole grid with metallic return

On both line 12 and line 24 in the bipole test grid with metallic return, eleven fault points are equally distributed between the two terminal inductors. A P2P fault with a resistance of 0.01 Ω is applied to each fault point, and the initial derivative of i_{12}^{p} and i_{24}^{p} are obtained. The simulated and calculated initial current derivatives corresponding to each fault point are plotted in Fig. 2.12, where $i_{12}^{p\prime}$ and $i_{24}^{p\prime}$ are $i_{1f}^{p\prime}$ and $i_{2f}^{p\prime}$ when the fault is on line 12 and line 24, respectively. Fig. 2.12 justifies the accuracy of the developed current-derivative calculation method for the bipole grid with metallic return during a P2P fault. Meanwhile, Fig. 2.12 indicates that when the fault move from line 12 to line 24, the magnitude of $\frac{\mathrm{d}i_{12}^{p}}{\mathrm{d}t}_{0}$ will decrease significantly, and the magnitude of $\frac{\mathrm{d}i_{24}^{p}}{\mathrm{d}t}_{0}$ will rise to a large value.

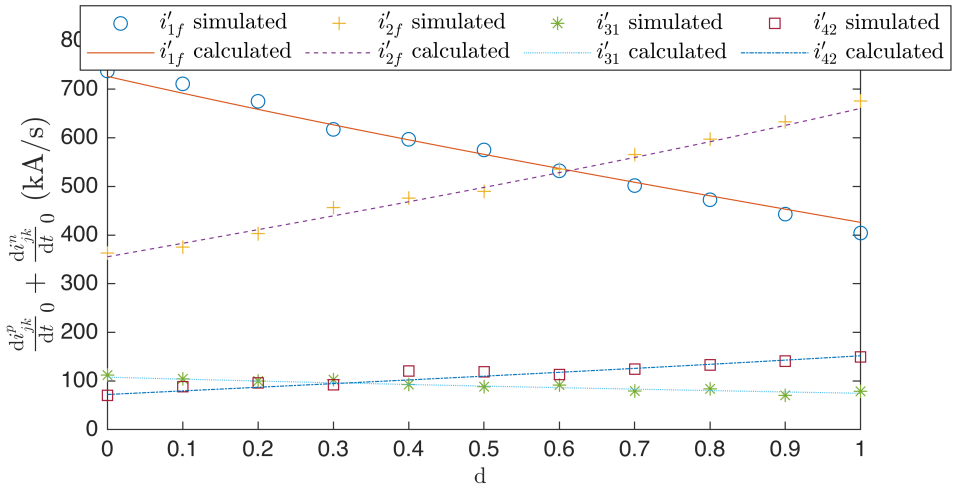

Figure 2.11: Initial current derivatives when a P2G fault occurs on different points of line 12 in an symmetric monopole grid.

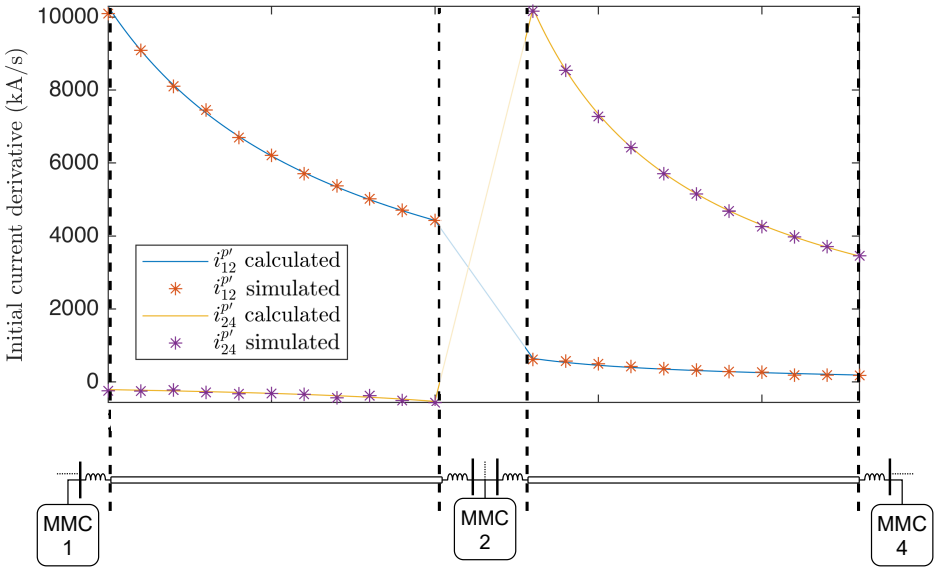

Figure 2.12: Initial current derivatives when a P2P fault occurs on different points of line 12 and line 24 in a bipole grid with metallic return.

Chapter 3

Current Derivative-Based Relaying Algorithm for HVDC Grids

3.1 Introduction

Various relaying algorithms for HVDC grids can be categorized into time-domain [5, 32, 41, 42, 43, 44, 45, 46, 47, 48] and frequency-domain [49, 50, 51, 52, 53, 54, 55, 56, 57]. Time-domain relays include overcurrent [42], undervoltage [41], derivatives [40, 58, 59], current differential [60, 61], traveling wave [45], and AI-based [46, 47, 48] approaches. Overcurrent and undervoltage relays require few calculation resources but lack selectivity and quick response [42]. Derivative relays use the rising speed of current or voltage to detect the fault. They respond quickly to the fault and have selectivity if terminal inductors are implemented at the ends of each transmission line [43]. Two main concerns about derivative relays are determining the pick-up threshold and measuring accurate derivatives [5, 44]. Current differential relays rely on communication channels. They provide high sensitivity, but the inherent communication delay limits their applications as the primary protection scheme in large HVDC grids [54]. Traveling wave-based relays rely on the detection of steep voltage wavefronts [32, 45]. These relays respond quickly to the fault but require a high sampling frequency of currents and voltages, which adds to the investment. Pick-up thresholds for these relays can be obtained by using the simplified HVDC model [45]. AI-based relays employ algorithms in pattern recognition fields to identify and locate faults [46, 47, 48]. AI algorithms are firstly trained on datasets (e.g., voltages and currents) of different fault scenarios. Then, these algorithms are applied to real-time measured voltages and currents to identify the fault. Generally, AI-based

relays require significant calculation resources.

Most frequency-domain relays rely on high-frequency components of current or voltage measurements because high-frequency components of currents and voltages on the faulty line are larger than those on healthy lines [49]. For these relays, an internal fault is detected if the square of the high-frequency component [49, 50] or the ratio between the high-frequency and low-frequency components exceeds a threshold [51], whereas [50, 51] use current measurements, and [49] uses voltage measurements. Frequency components are extracted by the Laplace transform [52], the short-time Fourier transform [53], the S transform [54], or the wavelet transform (WT) [55, 56], and the relay settings are determined by extensive simulations, which are time consuming. Disadvantages of frequency-domain relays are that 1) the design of high-frequency filters is not trivial, 2) transform algorithms require significant calculation resources, and 3) frequency-domain relays are slower than time-domain ones [57].

This chapter presents a number of relaying algorithms for HVDC grids in various configurations. All of these relaying algorithms use locally measured current derivatives, and they are fast, selective, and calculation-resource-sparing. Furthermore, all relay settings are calculated instead of being obtained by performing time-consuming electromagnetic transient (EMT) simulations. Section 3.2 introduces the developed relaying algorithms. Section 3.3 introduces the calculation of the relay settings. Section 3.4 shows simulation results when the developed relaying algorithm is employed in the test grid.

3.2 Current Derivative-Based Relaying Algorithm

This section presents a number of relaying algorithms for HVDC grids in various configurations. In this section, first, a universal framework of the relaying algorithms is presented, and then, the specific relaying algorithms for five grid topologies—the symmetric monopole grid, the asymmetric monopole grid with ground or metallic return, and the bipole grid with metallic or ground return—are presented.

Fig. 3.1 shows the universal framework for relay jk, the relay on line jk near MMC j. The relaying algorithm only uses the locally measured current derivatives and contains three modules: fault-type discrimination, internal fault detection, and external fault detection. In the module 1, measured current derivatives are used to determine the fault type, i.e., P2P, P2M, or P2G, based on the characteristics of

current derivatives. Based on the current-derivative characteristics, a set of comparison blocks can be designed to distinguish between different types of faults, Fig. 3.1. The characteristics of current derivatives in each grid topology and for various fault scenarios are listed in Table 3.1. The general trend based on Table 3.1 is that i) for a P2P fault, $|\frac{\mathrm{d}i^p_{jk}}{\mathrm{d}t} + \frac{\mathrm{d}i^n_{jk}}{\mathrm{d}t}|$ is small because the positive and negative derivatives cancel each other, ii) for a P2G fault, $|\frac{\mathrm{d}i^p_{jk}}{\mathrm{d}t} + \frac{\mathrm{d}i^n_{jk}}{\mathrm{d}t}|$ is large, and iii) for a P2M fault, $|\frac{\mathrm{d}i^m_{jk}}{\mathrm{d}t}|$ is large, where the P2M fault in an asymmetric monopole grid with metallic return is similar to the P2P fault in a symmetric monopole grid. It should be noted that module 1 can not strictly identify the fault type but only specifies that the fault will not be a certain type of an internal fault. For example, if a P2G fault occurs far away from line jk in a bipole grid with metallic return, $|\frac{\mathrm{d}i^p_{jk}}{\mathrm{d}t} + \frac{\mathrm{d}i^g_{jk}}{\mathrm{d}t}|$ could be small, and relay jk will know that this fault must not be an internal P2G or P2M fault.

Table 3.1: Characteristics of current derivatives in each grid topology and for various fault scenarios

Grid configuration	Fault scenario	Characteristics of current derivatives
Symmetric monopole	P2G	Large $\lvert\frac{\mathrm{d}i^p_{jk}}{\mathrm{d}t} + \frac{\mathrm{d}i^n_{jk}}{\mathrm{d}t}\rvert$
	P2P	Small $\lvert\frac{\mathrm{d}i^p_{jk}}{\mathrm{d}t} + \frac{\mathrm{d}i^n_{jk}}{\mathrm{d}t}\rvert$
Asymmetric monopole with ground return	P2G	Large $-\frac{\mathrm{d}i^n_{jk}}{\mathrm{d}t}$
Asymmetric monopole with metallic return	P2G	Large $\lvert\frac{\mathrm{d}i^n_{jk}}{\mathrm{d}t} + \frac{\mathrm{d}i^m_{jk}}{\mathrm{d}t}\rvert$
	P2M	Small $\lvert\frac{\mathrm{d}i^n_{jk}}{\mathrm{d}t} + \frac{\mathrm{d}i^m_{jk}}{\mathrm{d}t}\rvert$
Bipole with ground return	P2G	Large $\lvert\frac{\mathrm{d}i^p_{jk}}{\mathrm{d}t} + \frac{\mathrm{d}i^n_{jk}}{\mathrm{d}t}\rvert$
	P2P	Small $\lvert\frac{\mathrm{d}i^p_{jk}}{\mathrm{d}t} + \frac{\mathrm{d}i^n_{jk}}{\mathrm{d}t}\rvert$
Bipole with metallic return	P2G	Large $\lvert\frac{\mathrm{d}i^p_{jk}}{\mathrm{d}t} + \frac{\mathrm{d}i^n_{jk}}{\mathrm{d}t}\rvert$ and small $\lvert\frac{\mathrm{d}i^m_{jk}}{\mathrm{d}t}\rvert$
	P2M	Medium $\lvert\frac{\mathrm{d}i^p_{jk}}{\mathrm{d}t} + \frac{\mathrm{d}i^n_{jk}}{\mathrm{d}t}\rvert$ and large $\lvert\frac{\mathrm{d}i^m_{jk}}{\mathrm{d}t}\rvert$
	P2P	Small $\lvert\frac{\mathrm{d}i^p_{jk}}{\mathrm{d}t} + \frac{\mathrm{d}i^n_{jk}}{\mathrm{d}t}\rvert$ and small $\lvert\frac{\mathrm{d}i^m_{jk}}{\mathrm{d}t}\rvert$

After the completion of the fault-type discrimination module, the current derivative will be compared with the threshold corresponding to the fault type in module 2. For example, in the bipole grid with metallic return, if the real-time measured

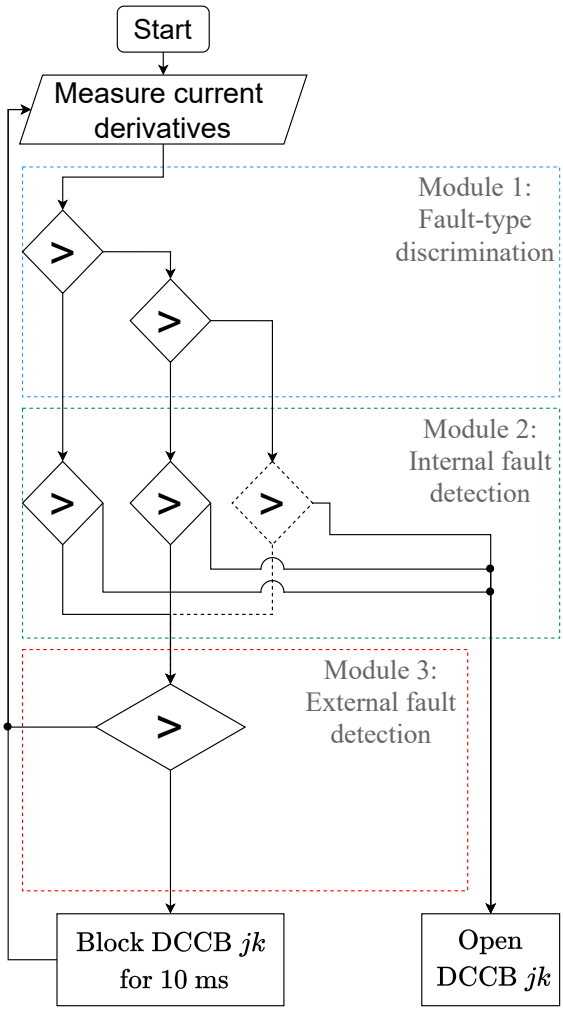

Figure 3.1: Universal framework for relay jk in an HVDC system.

$|\frac{\mathrm{d}i_{jk}^{p}}{\mathrm{d}t} + \frac{\mathrm{d}i_{jk}^{n}}{\mathrm{d}t}|$ is small (unique characteristic of the P2P fault), $\frac{\mathrm{d}i_{jk}^{p}}{\mathrm{d}t}$ will be compared with a threshold corresponding to P2P faults to determine if this fault is an internal P2P fault. If the derivative is larger than the threshold, an internal fault is detected, and DCCB jk will be triggered.

If the criteria in module 2 are not fulfilled, the derivative will be compared with a threshold in module 3 to determine if the fault is external. If an external fault is detected in module 3, DCCB jk will be blocked for 10 ms. Interruption of fault current by DCCBs on faulty lines may result in large current derivatives on healthy

lines. The main objective of module 3 is to prevent the trip of DCCBs on healthy lines due to the trip of DCCBs on faulty lines.

3.2.1 Relaying Algorithm for a Bipole Grid with Metallic Return

The input data to relay jk are current derivatives of the positive, metallic, and negative poles of line jk, Fig. 3.2. For the sake of simplicity, the prime mark is used to denote the derivative in Fig. 3.2. In this subsection, the bipole grid is assumed to be low-resistance grounded at one terminal and high-resistance grounded at others.

There are three types of faults in a bipole grid with metallic return, the P2P, P2G, and P2M faults. In module 1, the real-time measured $|\frac{\mathrm{d}i^p_{jk}}{\mathrm{d}t} + \frac{\mathrm{d}i^n_{jk}}{\mathrm{d}t}|$ is firstly compared with DI^{th1}_{jk}, where DI^{th1}_{jk} is slightly smaller than the minimum $|\frac{\mathrm{d}i^p_{jk}}{\mathrm{d}t} + \frac{\mathrm{d}i^n_{jk}}{\mathrm{d}t}|$ when a P2M fault occurs on line jk. If $|\frac{\mathrm{d}i^p_{jk}}{\mathrm{d}t} + \frac{\mathrm{d}i^n_{jk}}{\mathrm{d}t}| > DI^{th1}_{jk}$, $|\frac{\mathrm{d}i^m_{jk}}{\mathrm{d}t}|$ will be compared with DI^{th2}_{jk}, where DI^{th2}_{jk} is slightly smaller than the minimum $|\frac{\mathrm{d}i^m_{jk}}{\mathrm{d}t}|$ when an internal P2M fault occurs. If $|\frac{\mathrm{d}i^m_{jk}}{\mathrm{d}t}| > DI^{th2}_{jk}$, an internal P2M fault is detected—in module 1 instead of module 2. Generally, module 1 is capable of detecting one type of internal fault. This is why the right block in module 2 of Fig. 3.1(a) is dashed and can be removed.

If $|\frac{\mathrm{d}i^p_{jk}}{\mathrm{d}t} + \frac{\mathrm{d}i^n_{jk}}{\mathrm{d}t}| < DI^{th1}_{jk}$, $\frac{\mathrm{d}i^p_{jk}}{\mathrm{d}t}$ will be compared with DI^{th3} in module 2. DI^{th3} is smaller than the minimum $\frac{\mathrm{d}i^p_{jk}}{\mathrm{d}t}$ when a P2P fault occurs on line jk and is larger than the maximum $\frac{\mathrm{d}i^p_{jk}}{\mathrm{d}t}$ when an external P2P fault occurs. All the relays in a bipole grid with metallic return can use the same DI^{th3}—which will be proven in Section 3.3.1—so DI^{th3} does not have a subscript.

If $|\frac{\mathrm{d}i^m_{jk}}{\mathrm{d}t}| < DI^{th2}_{jk}$, $\frac{\mathrm{d}i^p_{jk}}{\mathrm{d}t}$ and $\frac{\mathrm{d}i^n_{jk}}{\mathrm{d}t}$ will be compared with DI^{th4}_{jk} and $-DI^{th4}_{jk}$, respectively. DI^{th4} is slightly smaller than the minimum $\frac{\mathrm{d}i^p_{jk}}{\mathrm{d}t}$ when an internal positive P2G fault occurs. If one of the criteria in module 2 is satisfied, an internal fault is detected, and DCCB jk will be triggered.

If no criterion in module 2 is satisfied, $|\frac{\mathrm{d}i^p_{jk}}{\mathrm{d}t}|$ and $|\frac{\mathrm{d}i^n_{jk}}{\mathrm{d}t}|$ will be compared with DI^{th5}_{jk} in module 3. DI^{th5}_{jk} is slightly smaller than the minimum $|\frac{\mathrm{d}i^p_{jk}}{\mathrm{d}t}|$ when a positive P2M fault occurs on an adjacent line to line jk. The adjacent lines to line jk are those directly connected to converter j or converter k. If either one of these derivatives exceeds DI^{th5}_{jk}, an external fault is detected, and DCCB jk will be blocked for 10 ms.

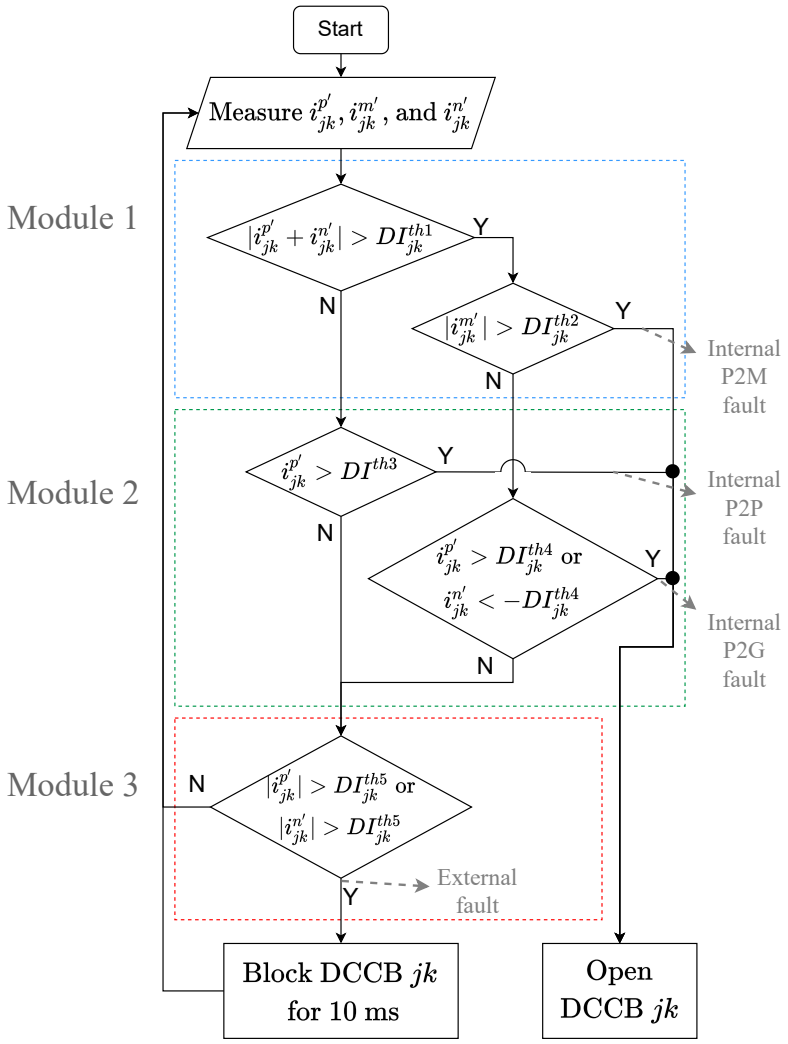

Figure 3.2: Operating principle of relay jk in a bipole grid with metallic return.

3.2.2 Relaying Algorithms for a Symmetric Monopole Grid, an Asymmetric Monopole Grid with Metallic Return, and a Bipole Grid with Ground Return

The symmetric monopole grid, asymmetric monopole grid with metallic return, and bipole grid with ground return have a same characteristic: they all have two poles for power transmission, where the metallic return can be considered as the neutral pole. Consequently, the operating principles of the relays in these grids are similar,

Fig. 3.3. This subsection will take the symmetric monopole grid as an example and introduce this grid's relaying algorithm illustrated in Fig. 3.3(a) in detail. The relaying algorithms for an asymmetric monopole grid with metallic return and a bipole grid with ground return will be introduced briefly.

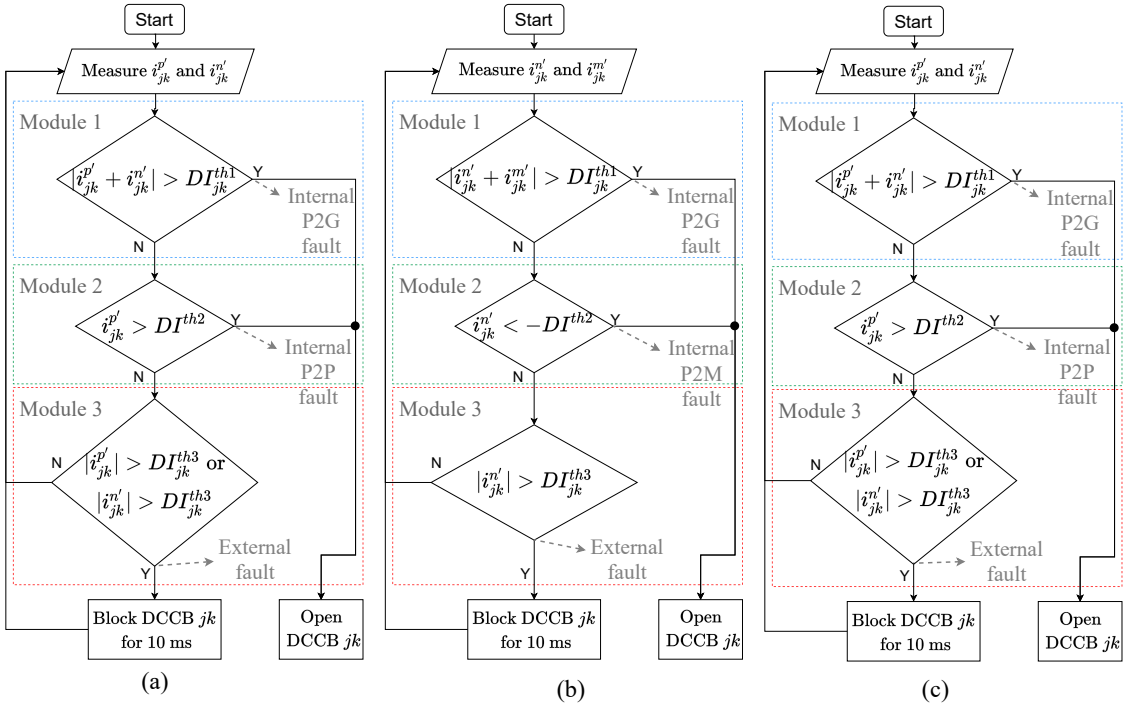

Figure 3.3: Operating principle of relay jk in (a) a symmetric monopole grid, (b) an asymmetric monopole grid with metallic return, and (c) a bipole grid with ground return.

The inputs to relay jk in the symmetric monopole grid are current derivatives on the positive and negative poles of line jk. In module 1, $|\frac{\mathrm{d}i^p_{jk}}{\mathrm{d}t} + \frac{\mathrm{d}i^n_{jk}}{\mathrm{d}t}|$ is compared with a threshold DI^{th1}_{jk}. DI^{th1}_{jk} is slightly smaller than the minimum $|\frac{\mathrm{d}i^p_{jk}}{\mathrm{d}t} + \frac{\mathrm{d}i^n_{jk}}{\mathrm{d}t}|$ when a P2G fault occurs on line jk. If the real-time measured $|\frac{\mathrm{d}i^p_{jk}}{\mathrm{d}t} + \frac{\mathrm{d}i^n_{jk}}{\mathrm{d}t}|$ is larger than DI^{th1}_{jk}, an internal P2G fault is detected

If $|\frac{\mathrm{d}i^p_{jk}}{\mathrm{d}t} + \frac{\mathrm{d}i^n_{jk}}{\mathrm{d}t}|$ is smaller than DI^{th1}_{jk}, $\frac{\mathrm{d}i^p_{jk}}{\mathrm{d}t}$ will be compared with DI^{th2} in module 2, where DI^{th2} is similar to the definition of DI^{th3} in Section 3.2.1. If $\frac{\mathrm{d}i^p_{jk}}{\mathrm{d}t} > DI^{th2}$, an internal P2P fault is detected.

If no internal fault is detected, $|\frac{\mathrm{d}i^p_{jk}}{\mathrm{d}t}|$ and $|\frac{\mathrm{d}i^n_{jk}}{\mathrm{d}t}|$ will be compared with DI^{th3}_{jk} in module 3. DI^{th3}_{jk} is slightly smaller than the minimum $|\frac{\mathrm{d}i^p_{jk}}{\mathrm{d}t}|$ when a positive P2G fault occurs on an adjacent line of line jk. If an external fault is detected, DCCB jk will be blocked for 10 ms to prevent the trip of DCCB jk due to the trip of DCCBs on adjacent lines.

For an asymmetric monopole grid with metallic return, DI^{th1}_{jk} is slightly smaller than the minimum $|\frac{\mathrm{d}i^n_{jk}}{\mathrm{d}t} + \frac{\mathrm{d}i^m_{jk}}{\mathrm{d}t}|$ when a P2G fault occurs on line jk; DI^{th2} is smaller than the minimum $|\frac{\mathrm{d}i^n_{jk}}{\mathrm{d}t}|$ when a P2M fault occurs on line jk and is larger than the maximum $|\frac{\mathrm{d}i^n_{jk}}{\mathrm{d}t}|$ when an external P2M fault occurs; DI^{th3}_{jk} is slightly smaller than the minimum $|\frac{\mathrm{d}i^n_{jk}}{\mathrm{d}t}|$ when a P2M fault occurs on an adjacent line of line jk.

For a bipole grid with ground return, DI^{th1}_{jk} is slightly smaller than the minimum $|\frac{\mathrm{d}i^p_{jk}}{\mathrm{d}t} + \frac{\mathrm{d}i^n_{jk}}{\mathrm{d}t}|$ when a P2G fault occurs on line jk; DI^{th2} is smaller than the minimum $|\frac{\mathrm{d}i^p_{jk}}{\mathrm{d}t}|$ when a P2P fault occurs on line jk and is larger than the maximum $|\frac{\mathrm{d}i^p_{jk}}{\mathrm{d}t}|$ when an external P2P fault occurs; DI^{th3}_{jk} is slightly smaller than the minimum $|\frac{\mathrm{d}i^p_{jk}}{\mathrm{d}t}|$ when a positive P2G fault occurs on an adjacent line of line jk.

3.2.3 Relaying Algorithms for Asymmetric Monopole Grid with Ground Return

The operating principle for relay jk in an asymmetric monopole grid with ground return is illustrated in Fig. 3.4. The inputs to relay jk is the current derivative on the negative poles of line jk. In module 1, $\frac{\mathrm{d}i^n_{jk}}{\mathrm{d}t}$ is compared with a threshold $-DI^{th1}$. DI^{th1} is smaller than the minimum $|\frac{\mathrm{d}i^n_{jk}}{\mathrm{d}t}|$ when a P2G fault occurs on line jk and is larger than the maximum $|\frac{\mathrm{d}i^n_{jk}}{\mathrm{d}t}|$ when an external P2G fault occurs. If the real-time measured $\frac{\mathrm{d}i^n_{jk}}{\mathrm{d}t}$ is small than $-DI^{th1}$ ($|\frac{\mathrm{d}i^n_{jk}}{\mathrm{d}t}| > DI^{th1}$), an internal P2G fault is detected. Since there is only one type of DC fault in an asymmetric monopole grid with ground return, module 2 is useless for relays in this grid topology. If no internal P2G fault is detected, $|\frac{\mathrm{d}i^n_{jk}}{\mathrm{d}t}|$ will be compared with DI^{th2}_{jk} in module 3. DI^{th2}_{jk} is slightly smaller than the minimum $|\frac{\mathrm{d}i^n_{jk}}{\mathrm{d}t}|$ when a negative P2G fault occurs on a line adjacent to line jk. If an external fault is detected, DCCB jk will be blocked for 10 ms to prevent the trip of DCCB jk due to the trip of DCCBs on adjacent lines.

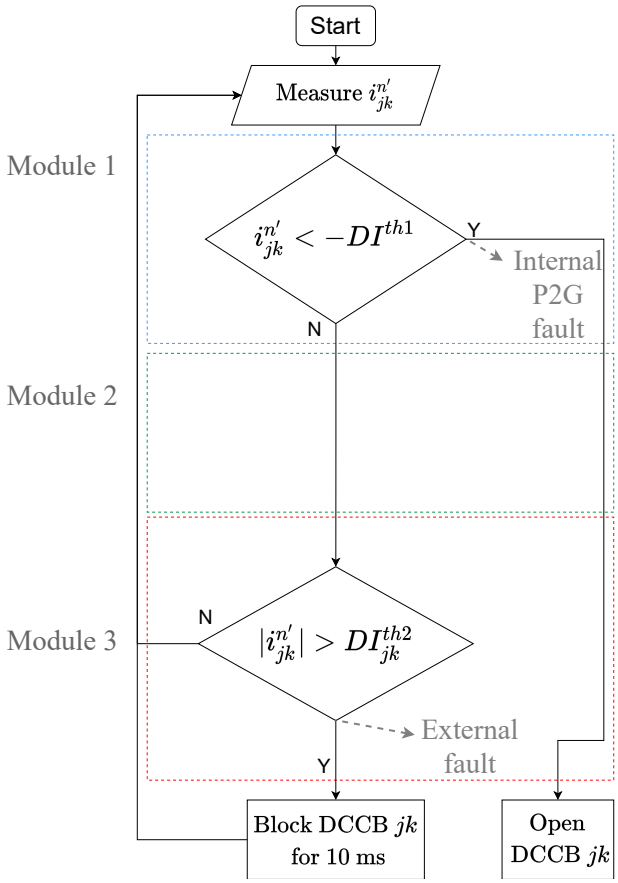

Figure 3.4: Operating principle for relay jk in an asymmetric monopole grid with ground return.

3.3 Calculation of Relay Settings

This section calculates initial current derivatives, the current derivatives right after the fault occurrence, of transmission lines and use the calculated initial current derivatives to determine the thresholds for relaying algorithms. According to (2.13), (2.14), (2.17), and (2.20), initial current derivatives $\frac{\mathrm{d}\boldsymbol{i}}{\mathrm{d}t}_0$ can be approximated as

$$\frac{\mathrm{d}\boldsymbol{i}}{\mathrm{d}t}_0 = -\mathbf{L}^{-1}(\mathbf{R}\boldsymbol{i}_0 - \mathbf{A}\boldsymbol{v}_0) \approx V_{dc}\mathbf{L}^{-1}\mathbf{A}\mathbf{1}, \tag{3.1}$$

where $\frac{\mathrm{d}\boldsymbol{i}}{\mathrm{d}t}_0$ is the vector of initial current derivatives of transmission lines; $\boldsymbol{i}_0$ and $\boldsymbol{v}_0$ are pre-fault values of $\boldsymbol{i}$ and $\boldsymbol{v}$, respectively. The elements in $\mathbf{R}\boldsymbol{i}_0$ represent pre-fault voltage drops on electrical paths, while the non-zero elements in $\mathbf{A}\boldsymbol{v}_0$ are close to

the rated voltage of the HVDC grid V_{dc} . Since the voltage drops on electrical paths (<2 kV) are much smaller than V_{dc} (640 kV for the monopole test grid), $\mathbf{R}\boldsymbol{i}_0$ can be neglected compared to $\mathbf{A}\boldsymbol{v}_0$. Besides, $\boldsymbol{v}_0$ can be approximated as $V_{dc}\mathbf{1}$ because the elements in $\boldsymbol{v}_0$ are close to V_{dc}. As a result, the approximation in (3.1) can be obtained.

This approximation provides three advantages: 1) simplifying the expression for $\frac{\mathrm{d}\boldsymbol{i}}{\mathrm{d}t}_0$, 2) ensuring the calculated thresholds are insensitive to changes in the operating point, and 3) demonstrating that the initial current derivatives does not depend on the fault resistance. Due to these advantages, the relaying algorithm based on current derivatives is dependable even when the operating point changes or the fault resistance is high.

3.3.1 Calculation of DI^{thx}

Each threshold in the discussed relaying algorithms corresponds to a fault type. For example, DI^{th3} in a bipole grid with metallic return corresponds to the P2P fault because DI^{th3} should be smaller than the minimum $\frac{\mathrm{d}i^p_{jk}}{\mathrm{d}t}_0$ during an internal P2P fault and larger than the maximum $\frac{\mathrm{d}i^p_{jk}}{\mathrm{d}t}_0$ during an external P2P fault. Compared to other thresholds for the bipole grid with metallic return, DI^{th3} is the only one that does not have a subscript, indicating all relays in the grid can use the same DI^{th3}. Some thresholds for other grid topologies—DI^{th2} for a symmetric monopole grid, DI^{th1} for an asymmetric monopole grid with ground return, DI^{th2} for an asymmetric monopole grid with metallic return, and DI^{th2} for a bipole grid with ground return—have the same characteristic. These relay settings, denoted as $DI^{thx}, x \in \{1,2,3\}$, can be calculated by

$$DI^{thx} = \frac{\mathcal{L}(|i_{flt}|) + \mathcal{U}(|i_{hlt}|)}{2}, \tag{3.2}$$

where i_{flt} and i_{hlt} are the initial current derivatives of faulty and healthy lines, respectively, $\mathcal{L}(|i_{flt}|)$ and $\mathcal{U}(|i_{hlt}|)$ are the lower and upper bounds of $|i_{flt}|$ and $|i_{hlt}|$, respectively. These two bounds are calculated by

$$\mathcal{L}(|i_{flt}|) = V_{dc}\frac{(1-e)^{b-1}}{(1+e)^{b-1}}\frac{\alpha l_t + l_c}{\left(\frac{\mathbf{L}_{diag}(1)}{2}\right)^2}, \tag{3.3a}$$

$$\mathcal{U}(|i_{hlt}|) = V_{dc}\frac{\sum_{k=0}^{b-1}\left((!(b-k)+!(b-k-1))\binom{b-1}{k} l_c^{b-k}\prod_{s=1}^{k}\mathbf{L}_{diag}(s)\right)}{(\mathbf{L}_{diag}(b)-\alpha l_t - l_c)(\alpha l_t + l_c)(1-e)^{b-1}\prod_{k=1}^{b-1}\mathbf{L}_{diag}(k)}, \tag{3.3b}$$

where all terminal inductances and equivalent MMC inductances are assumed to be l_t and l_c, respectively. α is 1 for the asymmetric monopole grid with ground return;

and α is 2 for the symmetric monopole grid, asymmetric monopole grid with metallic return, and bipole grid. $\binom{b}{k}$ is the binomial coefficient "b choose k", where $\binom{b}{k} = 0$ when $k > b$ or $k < 0$. $!k$ is the subfactorial of k, where $!0 = 1$. $\mathbf{L}_{diag}$ and e are expressed as

$$\mathbf{L}_{diag} = \text{order}(\text{diag}(\mathbf{A}_0\mathbf{L}^c\mathbf{A}_0^\top + \alpha\mathbf{L}_0^l)), \tag{3.4a}$$

$$e = \frac{l_c^2 \max_{1\le k\le b} \sum_{s\neq k\in\{1,\cdots,b\}} \left|\mathbf{A}_0\mathbf{A}_0^\top(k,s)\right|}{\mathbf{L}_{diag}(b) - l_c \max_{1\le k\le b} \sum_{s\neq k\in\{1,\cdots,b\}} \left|\mathbf{A}_0\mathbf{A}_0^\top(k,s)\right|} \frac{1}{\mathbf{L}_{diag}(1)}. \tag{3.4b}$$

$\text{diag}(\mathbf{A}_0\mathbf{L}^c\mathbf{A}_0^\top + \alpha\mathbf{L}_0^l)$ returns a vector containing all diagonal elements in $\mathbf{A}_0\mathbf{L}^c\mathbf{A}_0^\top + \alpha\mathbf{L}_0^l$. $\text{order}(\text{diag}(\mathbf{A}_0\mathbf{L}^c\mathbf{A}_0^\top + \alpha\mathbf{L}_0^l))$ returns a vector where all elements in $\text{diag}(\mathbf{A}_0\mathbf{L}^c\mathbf{A}_0^\top + \alpha\mathbf{L}_0^l)$ are ordered from the largest one to the smallest one, i.e., $\mathbf{L}_{diag}(1)$ is the largest element in $\mathbf{L}_{diag}$. The proof of (3.3) is presented in Section 3.3.2.

3.3.2 Bounds for Initial Current Derivatives

The initial current derivative of the faulty pole is approximated as

$$\frac{\mathrm{d}\boldsymbol{i}}{\mathrm{d}t}_0 \approx \mathbf{L}^{-1}\mathbf{A}_f V_{dc}\mathbf{1} = V_{dc}\begin{bmatrix} \mathbf{L}^{-1}(1,b) - \mathbf{L}^{-1}(1,b+1) \\ \vdots \\ \mathbf{L}^{-1}(k,b) - \mathbf{L}^{-1}(k,b+1) \\ \vdots \\ \mathbf{L}^{-1}(b-1,b) - \mathbf{L}^{-1}(b-1,b+1) \\ \mathbf{L}^{-1}(b,b) - \mathbf{L}^{-1}(b,b+1) \\ \mathbf{L}^{-1}(b+1,b) - \mathbf{L}^{-1}(b+1,b+1) \end{bmatrix}, \tag{3.5}$$

where the last two red-colored elements correspond to initial derivatives of faulty line currents, and other elements correspond to those of healthy line currents. Since each element in $\mathbf{L}^{-1}$ can be calculated as

$$\mathbf{L}^{-1}(k,s) = \frac{(-1)^{s+k} m_{s,k}}{\det(\mathbf{L})}, \qquad (1 \le k, s \le b+1), \tag{3.6}$$

the initial current derivative can be expressed as

$$\left|\frac{\mathrm{d}\boldsymbol{i}(k)}{\mathrm{d}t}_0\right| = V_{dc}\frac{|m_{b,k} + m_{b+1,k}|}{|\det(\mathbf{L})|}, \qquad (1 \le k \le b+1), \tag{3.7}$$

where $\det(\cdot)$ is the determinant operator, and $m_{s,k}$ is the (s,k) minor of $\mathbf{L}$. $\mathbf{L}$ will change when the fault location changes. The following part will calculate the two-sided bounds for $|\det(\mathbf{L})|$, the lower bound for $|m_{b,k_f} + m_{b+1,k_f}|$, and the upper bound for $|m_{b,k_h} + m_{b+1,k_h}|$ among all fault locations to determine the relay settings.

3.3.2.1 Bounds for $|\det(\mathbf{L})|$

$\mathbf{L}$ is a $(b+1)\times(b+1)$ diagonally dominant matrix, whose two-sided bounds can be calculated as [62]:

$$\begin{aligned}&\prod_{k=1}^{b+1}\left[|\mathbf{L}(k,k)|-\left(\max_{k+1\le s\le b+1}\frac{|\mathbf{L}(s,k)|}{|\mathbf{L}(s,s)|-\boldsymbol{u}(s)}\right)\boldsymbol{u}(k)\right]\le|\det(\mathbf{L})|\\&\le\prod_{k=1}^{b+1}\left[|\mathbf{L}(k,k)|+\left(\max_{k+1\le s\le b+1}\frac{|\mathbf{L}(s,k)|}{|\mathbf{L}(s,s)|-\boldsymbol{u}(s)}\right)\boldsymbol{u}(k)\right],\end{aligned}\tag{3.8}$$

where $\boldsymbol{u}(k)=\sum_{s=k+1}^{b+1}|\mathbf{L}(k,s)|$. Equation (3.8) cannot calculate the bounds for $|\det(\mathbf{L})|$ among all fault locations, because (3.8) requires all elements in $\mathbf{L}$ to calculate the bounds. However, $\mathbf{L}$ varies when the fault location changes. In the following, (3.8) is modified such that only $\mathbf{A}_0$, $\mathbf{L}_{diag}$, l_t, and l_c are used to calculate the two-sided bounds for $|\det(\mathbf{L})|$.

Since $\max_{1\le k\le b}\sum_{s\ne k\in\{1,\cdots,b\}}l_c\left|\mathbf{A}_0\mathbf{A}_0^\top(k,s)\right|\ge\max_{1\le k\le b+1}\boldsymbol{u}(k)$, and the largest off-diagonal element in $\mathbf{L}$ is l_c, for each $1\le k_h\le b-1$,

$$(1-e)\mathbf{L}(k_h,k_h)\le|\mathbf{L}(k_h,k_h)|-\left(\max_{k_h+1\le s\le b+1}\frac{|\mathbf{L}(s,k_h)|}{|\mathbf{L}(s,s)|-\boldsymbol{u}(s)}\right)\boldsymbol{u}(k_h),\tag{3.9}$$

where e is defined in (3.4). According to the definition of $\mathbf{L}$ and $\mathbf{A}_f$, $\mathbf{L}(b,b+1)\equiv0$. Consequently,

$$\mathbf{L}(k_f,k_f)=|\mathbf{L}(k_f,k_f)|-\left(\max_{k_f+1\le s\le b+1}\frac{|\mathbf{L}(s,k_f)|}{|\mathbf{L}(s,s)|-\boldsymbol{u}(s)}\right)\boldsymbol{u}(k_f)\tag{3.10}$$

for each $b\le k_f\le b+1$.

Since $\mathbf{L}(k_h,k_h)$ and $\sum_{k_f=b}^{b+1}\mathbf{L}(k_f,k_f)$ compose the elements in $\mathbf{L}_{diag}$, and $\mathbf{L}(k_f,k_f)$ is not smaller than αl_t+l_c,

$$\prod_{k_f=b}^{b+1}\mathbf{L}(k_f,k_f)\prod_{k_h=1}^{b-1}(1-e)\mathbf{L}(k_h,k_h)\ge(\mathbf{L}_{diag}(b)-\alpha l_t-l_c)(\alpha l_t+l_c)(1-e)^{b-1}\prod_{k=1}^{b-1}\mathbf{L}_{diag}(k).\tag{3.11}$$

Thus, $\mathcal{L}(|\det(\mathbf{L})|)$ can be calculated as

$$\mathcal{L}(|\det(\mathbf{L})|)=(\mathbf{L}_{diag}(b)-\alpha l_t-l_c)(\alpha l_t+l_c)(1-e)^{b-1}\prod_{k=1}^{b-1}\mathbf{L}_{diag}(k),\tag{3.12}$$

which only uses the pre-fault grid's parameters and is independent of the fault location.

Similarly, the upper bound for $|\det(\mathbf{L})|$ can be calculated as

$$\mathcal{U}(|\det(\mathbf{L})|) = (\frac{\mathbf{L}_{diag}(1)}{2})^2(1+e)^{b-1}\prod_{k=2}^{b}\mathbf{L}_{diag}(k). \tag{3.13}$$

3.3.2.2 Bounds for $|M_{b,k} + M_{b+1,k}|$

$\mathbf{M}_k$ is defined as follows:

$$\mathbf{M}_k = \begin{bmatrix}\mathbf{I}_{b-1,b-1} & \mathbf{0}_{b-1,2}\\ \mathbf{0}_{1,b-1} & \mathbf{1}_{1,2}\end{bmatrix}\mathbf{L}\begin{bmatrix}\mathbf{I}_{k-1} & \mathbf{0}_{k-1,b-k+1}\\ \mathbf{0}_{1,k-1} & \mathbf{0}_{1,b-k+1}\\ \mathbf{0}_{b-k+1,k-1} & \mathbf{I}_{b-k+1}\end{bmatrix}, \quad (1 \le k \le b+1). \tag{3.14}$$

It can be proved that $|\det(\mathbf{M}_k)| = |m_{b,k} + m_{b+1,k}|$.

3.3.2.3 Lower bound for $|\det(\mathbf{M}_{k_f})|$

$\mathbf{M}_{k_f}$ is a $b \times b$ diagonally dominate matrix, whose diagonal elements are elements in $\mathbf{L}_{diag}$ except for $\mathbf{M}_{k_f}(b,b)$, where $\mathbf{M}_{k_f}(b,b) = \mathbf{L}(k_f,k_f) \ge \alpha l_t + l_c$. Similar to (3.12), $\mathcal{L}(|\det(\mathbf{M}_{k_f})|)$ is expressed as

$$\mathcal{L}(|\det(\mathbf{M}_{k_f})|) = (\alpha l_t + l_c)(1-e)^{b-1}\prod_{k=2}^{b}\mathbf{L}_{diag}(k). \tag{3.15}$$

3.3.2.4 Upper bound for $|\det(\mathbf{M}_{k_h})|$

$\det(\mathbf{M}_{k_h})$ is partitioned into the sum of three determinants:

$$\det(\mathbf{M}_{k_h}) = \det(\mathbf{M}_{k_h,1}) + \det(\mathbf{M}_{k_h,2}) + \det(\mathbf{M}_{k_h,3}), \tag{3.16}$$

where $\mathbf{M}_{k_h,1}$, $\mathbf{M}_{k_h,2}$, and $\mathbf{M}_{k_h,3}$ are equal to $\mathbf{M}_{k_h}$, except that $\mathbf{M}_{k_h,1}(b,s)$, $\mathbf{M}_{k_h,2}(b,s)$, and $\mathbf{M}_{k_h,3}(b,s)$ are zero when $s \in \{b-1,b\}$, $s \in \{1,\cdots,b-2\} \cup \{b\}$, and $s \in \{1,\cdots,b-1\}$, respectively. For example, $\mathbf{M}_4$, $\mathbf{M}_{4,1}$, $\mathbf{M}_{4,2}$, and $\mathbf{M}_{4,3}$ for $b=8$ are shown in Fig. 3.5. The colored and un-colored elements in Fig. 3.5 are the diagonal and off-diagonal elements of $\mathbf{L}$, respectively.

All of the elements in $\mathbf{M}_{k_h,1}$ are divided into three sets,

$$Set_1 = \{\mathbf{M}_{k_h,1}(s,k) | (1 \le s = k \le k_h - 1) \vee (k_h + 1 \le s = k+1 \le b-1)\}, \tag{3.17a}$$

$$Set_2 = \{\mathbf{M}_{k_h,1}(s,k) | (1 \le s \le k_h - 1 \wedge k \ne s) \vee (s = k_h) \vee (k_h + 1 \le s \le b-1 \wedge k \ne s-1)\}, \tag{3.17b}$$

$$Set_3 = \{\mathbf{M}_{k_h,1}(s,k) | (s = b) \wedge (b-1 \le k \le b)\}, \tag{3.17c}$$

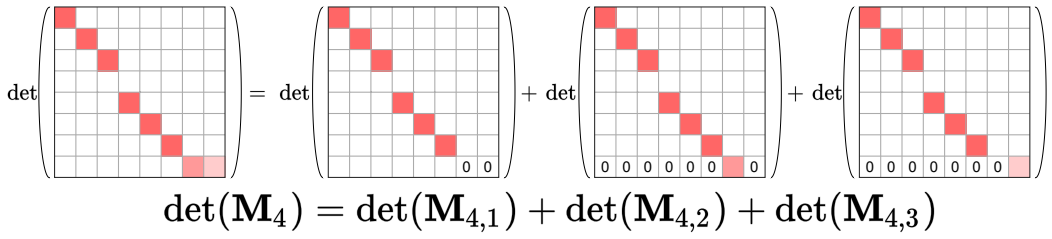

Figure 3.5: Matrices $\mathbf{M}_4$, $\mathbf{M}_{4,1}$, $\mathbf{M}_{4,2}$, and $\mathbf{M}_{4,3}$ for $b = 8$.

where the elements in Set_1, Set_2, and Set_3 correspond to the colored, un-colored, and zero elements of the $\mathbf{M}_{4,1}$ in Fig. 3.5, respectively. The upper bound for $|\det(\mathbf{M}_{k_h,1})|$ is expressed as

$$\mathcal{U}(|\det(\mathbf{M}_{k_h,1})|) = \sum_{k=0}^{b-2} \left((!(b-k)+!(b-1-k)) \binom{b-2}{k} l_c^{b-k} \prod_{s=1}^{k} \mathbf{L}_{diag}(s) \right). \tag{3.18}$$

To obtain (3.18), $|\det(\mathbf{M}_{k_h,1})|$ is considered as the sum of $b!$ summands, where each summand is the product of a sign factor and b elements in different rows and columns of $\mathbf{M}_{k_h,1}$. Meanwhile, it is assumed that the sign factor of each summand is positive, all elements in Set_2 are at their maximum value l_c, and the product of k elements in Set_1 is $\prod_{s=1}^{k} \mathbf{L}_{diag}(s)$. $(!(b-k)+!(b-1-k))$ means the number of ways that we can choose $b-k$ un-colored elements in different rows and columns from $\mathbf{M}_{k_h,1}$; and $\binom{b-2}{k}$ means the number of ways that we choose k colored elements in different rows and columns from $\mathbf{M}_{k_h,1}$.

Similarly,

$$\mathcal{U}(|\det(\mathbf{M}_{k_h,2})|) = \mathbf{M}_{k_h}(b,b-1) \sum_{k=0}^{b-2} ((!(b-1-k)+!(b-2-k)) \cdot \binom{b-2}{k} l_c^{b-1-k} \prod_{s=1}^{k} \mathbf{L}_{diag}(s)), \tag{3.19a}$$

$$\mathcal{U}(|\det(\mathbf{M}_{k_h,3})|) = \mathbf{M}_{k_h}(b,b) \sum_{k=0}^{b-2} ((!(b-1-k)+!(b-2-k)) \cdot \binom{b-2}{k} l_c^{b-1-k} \prod_{s=1}^{k} \mathbf{L}_{diag}(s)). \tag{3.19b}$$

Considering that $\mathbf{M}_{k_h}(b,b-1) + \mathbf{M}_{k_h}(b,b)$ is an element in $\mathbf{L}_{diag}$, $\mathcal{U}(|\det(\mathbf{M}_{k_h})|)$

can be obtained by adding (3.18) and (3.19) together as

$$\begin{aligned}\mathcal{U}(|\det(\mathbf{M}_{k_h})|) &\leq \mathcal{U}(|\det(\mathbf{M}_{k_h,1})|) + \mathcal{U}(|\det(\mathbf{M}_{k_h,2})|) + \mathcal{U}(|\det(\mathbf{M}_{k_h,3})|) \\ &= \sum_{k=0}^{b-1} \left((!(b-k) + !(b-1-k)) \binom{b-1}{k} l_c^{b-k} \prod_{s=1}^{k} \mathbf{L}_{diag}(s) \right). \end{aligned} \tag{3.20}$$

The bounds for $|i_{flt}|$ and $|i_{hlt}|$ are calculated as

$$\mathcal{L}(|i_{flt}|) = V_{dc} \frac{\mathcal{L}(|\det(\mathbf{M}_{k_f})|)}{\mathcal{U}(|\det(\mathbf{L})|)}, \tag{3.21a}$$

$$\mathcal{U}(|i_{hlt}|) = V_{dc} \frac{\mathcal{U}(|\det(\mathbf{M}_{k_h})|)}{\mathcal{L}(|\det(\mathbf{L})|)}. \tag{3.21b}$$

3.3.3 Calculation of DI_{jk}^{thx}

All of the thresholds $DI_{jk}^{thx}, x \in \{1,2,3,4,5\}$ that should be specifically calculated for relay jk and their corresponding calculation methods are presented in Table 3.2. Take DI_{jk}^{th1} for an symmetric monopole grid as an example, a positive P2G fault will be applied to the far end of line jk (the end of line jk close to MMC k), and $\frac{\mathrm{d}i_{jk}^{p}}{\mathrm{d}t}_0$ and $\frac{\mathrm{d}i_{jk}^{n}}{\mathrm{d}t}_0$ can be calculated by employing (3.1) to this fault scenario. Then, DI_{jk}^{th1} can be calculated as the product of $|\frac{\mathrm{d}i_{jk}^{p}}{\mathrm{d}t}_0 + \frac{\mathrm{d}i_{jk}^{n}}{\mathrm{d}t}_0|$ and a safety factor that is slightly smaller than 1, e.g., 0.95. To calculate DI_{jk}^{th3} for an symmetric monopole grid, a positive P2G fault will be applied to the far end of each line xy that is adjacent to line jk—the far end of line xy is the one far away from MMC j or MMC k. Then, (3.1) will be employed to each fault scenario, and $|\frac{\mathrm{d}i_{jk}^{p}}{\mathrm{d}t}_0|$ for each fault scenario can be obtained. Finally, DI_{jk}^{th3} can be calculated as the product of the minimum $|\frac{\mathrm{d}i_{jk}^{p}}{\mathrm{d}t}_0|$ among all the fault scenarios and a safety factor that is slightly smaller than 1.

3.4 Simulation Results

This section validates the feasibility of developed relaying algorithms. To evaluate the algorithm, hybrid four-terminal HVDC grids in different topologies are modeled in PSCAD/EMTDC.

Table 3.2: Calculation method for threshold DI_{jk}^{thx}.

	Threshold	Fault type	Fault point(s)	Calculated current derivative
Symmetric monopole grid	DI_{jk}^{th1}	Positive P2G	Far end of line jk	$\lvert\frac{\mathrm{d}(i_{jk}^{p}+i_{jk}^{n})}{\mathrm{d}t}\rvert$
	DI_{jk}^{th3}	Positive P2G	Far ends of adjacent lines xy	$\min(\lvert\frac{\mathrm{d}i_{xy}^{p}}{\mathrm{d}t}_{0}\rvert)$
Asymmetric monopole grid with ground return	DI_{jk}^{th2}	Negative P2G	Far ends of adjacent lines xy	$\min(\lvert\frac{\mathrm{d}i_{xy}^{n}}{\mathrm{d}t}_{0}\rvert)$
Asymmetric monopole grid with metallic return	DI_{jk}^{th1}	Negative P2M	Far end of line jk	$\lvert\frac{\mathrm{d}(i_{jk}^{n}+i_{jk}^{m})}{\mathrm{d}t}_{0}\rvert$
	DI_{jk}^{th3}	Negative P2M	Far ends of adjacent lines xy	$\min(\lvert\frac{\mathrm{d}i_{xy}^{n}}{\mathrm{d}t}_{0}\rvert)$
Bipole grid with ground return	DI_{jk}^{th1}	Positive P2G	Far end of line jk	$\lvert\frac{\mathrm{d}(i_{jk}^{p}+i_{jk}^{n})}{\mathrm{d}t}_{0}\rvert$
	DI_{jk}^{th3}	Positive P2G	Far ends of adjacent lines xy	$\min(\lvert\frac{\mathrm{d}i_{xy}^{p}}{\mathrm{d}t}_{0}\rvert)$
Bipole grid with metallic return	DI_{jk}^{th1}	Positive P2G	Far end of line jk	$\lvert\frac{\mathrm{d}(i_{jk}^{p}+i_{jk}^{n})}{\mathrm{d}t}_{0}\rvert$
	DI_{jk}^{th2}	Positive P2M	Far end of line jk	$\lvert\frac{\mathrm{d}i_{jk}^{m}}{\mathrm{d}t}_{0}\rvert$
	DI_{jk}^{th4}	Positive P2G	Far end of line jk	$\lvert\frac{\mathrm{d}i_{jk}^{p}}{\mathrm{d}t}_{0}\rvert$
	DI_{jk}^{th5}	Positive P2M	Far ends of adjacent lines xy	$\min(\lvert\frac{\mathrm{d}i_{xy}^{p}}{\mathrm{d}t}_{0}\rvert)$

3.4.1 Calculation of Thresholds

This subsection presents the calculated thresholds for the relays of the symmetric monopole grid and the bipole grid with metallic return.

In a symmetric monopole grid, using (3.3) and (3.2), $\mathcal{L}(|i_{flt}|)$, $\mathcal{U}(|i_{hlt}|)$, and DI^{th2} are calculated as 903.20 kA/s, 320.41 kA/s, and 611.81 kA/s, respectively. For the test system of this thesis, the minimum initial derivative of faulty line currents is 1450.2 kA/s, and the maximum initial derivative of healthy line currents is 193.81 kA/s. Since $193.81 < 611.81 < 1450.2$, the dependability and security of the designed relay is ensured.

The initial current derivative of each line during each fault can be obtained. DI_{jk}^{th1} for the symmetric monopole grid can be calculated as 0.9 times the minimum $|\frac{\mathrm{d}i_{jk}^{p}}{\mathrm{d}t}_{0}+\frac{\mathrm{d}i_{jk}^{n}}{\mathrm{d}t}_{0}|$ when a P2G fault occurs on line jk, and DI_{jk}^{th3} is 0.9 times the minimum $|\frac{\mathrm{d}i_{jk}^{p}}{\mathrm{d}t}_{0}|$ when a positive P2G fault occurs on lines adjacent to line jk.

The calculated thresholds for the symmetric monopole grid are shown in Table 3.3. Similarly, the thresholds for the bipole grid with metallic return can be calculated, Table 3.4.

Table 3.3: Thresholds for the symmetric monopole grid

Line jk	Line 12	Line 13	Line 14	Line 24	Line 34
DI_{jk}^{th1} (kA/s)	356.823	297.171	301.482	323.199	345.123
DI^{th2} (kA/s)			611.81		
DI_{jk}^{th3} (kA/s)	40.1508	8.5689	11.5569	15.4485	41.9067

Table 3.4: Thresholds for the bipole grid with metallic return

Line jk	Line 12	Line 13	Line 14	Line 24	Line 34
DI_{jk}^{th1} (kA/s)	2170.8	1386.63	1388.16	1691.28	2168.55
DI_{jk}^{th2} (kA/s)	1979.64	1219.05	1223.46	1510.38	1978.65
DI^{th3} (kA/s)			1475.9		
DI_{jk}^{th4} (kA/s)	3980.88	2541.78	2546.19	3103.65	3978.36
DI_{jk}^{th5} (kA/s)	84.303	46.0296	46.4769	59.1867	85.2624

3.4.2 Performance of the Developed Relaying Algorithm

The relaying algorithms for the symmetric monopole grid and the bipole grid with metallic return are evaluated in this section. P2P and P2G faults are applied to the symmetric monopole grid; P2P, P2G, and P2M faults are applied to the bipole grid with metallic return.

3.4.2.1 Low-impedance P2P fault in the symmetric monopole grid

Fig. 3.6 shows the current derivative of each line when a P2P fault with a resistance of 0.01 Ω occurs on line 12 near MMC 1 at $t = 1$ ms. After the fault occurrence, $|\frac{\mathrm{d}i_{12}^{p}}{\mathrm{d}t} + \frac{\mathrm{d}i_{12}^{n}}{\mathrm{d}t}|$ and $|\frac{\mathrm{d}i_{21}^{p}}{\mathrm{d}t} + \frac{\mathrm{d}i_{21}^{n}}{\mathrm{d}t}|$ remain below DI_{12}^{th1}, Fig. 3.6(a). Consequently, relay 12 and relay 21 identify this fault as a P2P fault in module 1. Then, $\frac{\mathrm{d}i_{12}^{p}}{\mathrm{d}t}$ and $\frac{\mathrm{d}i_{21}^{p}}{\mathrm{d}t}$ are compared with DI^{th2} in module 2. Since these two derivatives exceed DI^{th2} in one

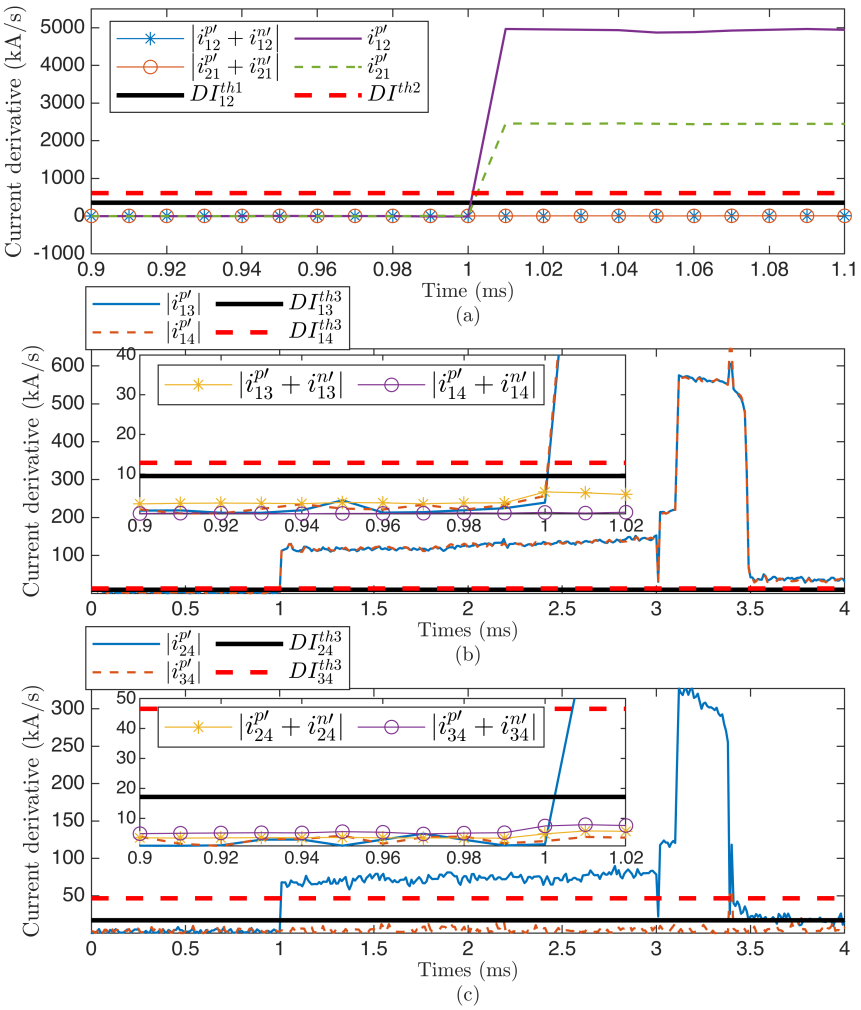

Figure 3.6: Current derivatives of each line during a P2P fault on line 12 near MMC 1 ($r_f = 0.01\,\Omega$).

sampling period (0.01 ms), relay 12 and relay 21 detect the internal P2P fault and trigger DCCB 12 and DCCB 21 at $t = 1.01$ ms, Fig. 3.7.

Meanwhile, relays on lines adjacent to line 12 detect an external fault. Take relay 13 as an example, for 0.9 ms $< t <$ 1.02 ms, $|\frac{\mathrm{d}i^p_{13}}{\mathrm{d}t} + \frac{\mathrm{d}i^n_{13}}{\mathrm{d}t}|$ and $\frac{\mathrm{d}i^p_{13}}{\mathrm{d}t}$ remain

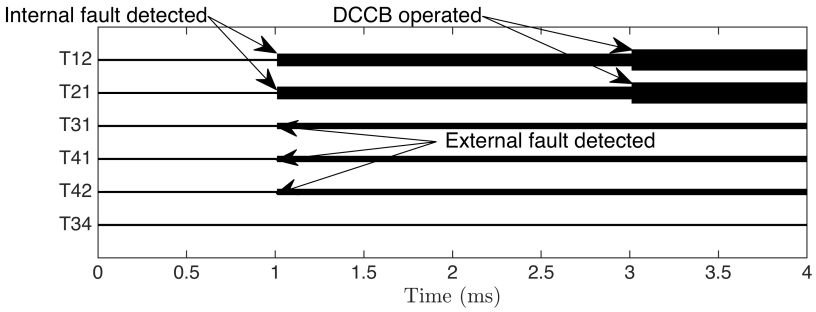

Figure 3.7: Trip signals during a P2P fault on line 12 near MMC 1 ($r_f = 0.01\,\Omega$).

below $DI_{13}^{th1} = 297.171$ kA/s and $DI^{th2} = 611.81$ kA/s, respectively, Fig. 3.6(b). Consequently, relay 13 detects no internal fault and proceeds to module 3, where $|\frac{\mathrm{d}i_{13}^p}{\mathrm{d}t}|$ is compared with DI_{13}^{th3}. The zoom-in box in Fig. 3.6(b) shows that $|\frac{\mathrm{d}i_{13}^p}{\mathrm{d}t}|$ exceeds DI_{13}^{th3} in 0.01 ms. As a result, relay 13 detects an external fault and blocks DCCB 13 for 10 ms, Fig. 3.7. When DCCB 12 and DCCB 21 operate at $t = 3.01$ ms, $|\frac{\mathrm{d}i_{13}^p}{\mathrm{d}t}|$ rises significantly and exceeds $DI^{th2} = 611.81$ kA/s at around $t = 3.5$ ms. However, DCCB 13 and DCCB 31 will not be triggered, because they have been blocked at $t = 1.01$ ms. Other relays on adjacent lines to line 12 also detect the external fault and block their DCCBs for 10 ms, Fig. 3.6(b)-(c) and Fig. 3.7.

Since $|\frac{\mathrm{d}i_{34}^p}{\mathrm{d}t}|$ stays below DI_{34}^{th3} and when the fault occurs, relay 34 and relay 43 detect no fault, Fig. 3.6(c). These two relays will neither mis-trigger DCCB 34 and DCCB 43 because $|\frac{\mathrm{d}i_{34}^p}{\mathrm{d}t} + \frac{\mathrm{d}i_{34}^n}{\mathrm{d}t}|$ and $|\frac{\mathrm{d}i_{34}^p}{\mathrm{d}t}|$ remain below DI_{34}^{th1} and DI^{th2} when DCCBs on line 12 operate, respectively.

3.4.2.2 High-impedance P2G fault in the symmetric monopole grid

Fig. 3.8 shows the current derivative of each line when a positive P2G fault with a resistance of 500 Ω occurs on line 12 near MMC 1 at $t = 1$ ms. After the fault occurrence, $|\frac{\mathrm{d}i_{12}^p}{\mathrm{d}t} + \frac{\mathrm{d}i_{12}^n}{\mathrm{d}t}|$ and $|\frac{\mathrm{d}i_{21}^p}{\mathrm{d}t} + \frac{\mathrm{d}i_{21}^n}{\mathrm{d}t}|$ exceeds DI_{12}^{th1} in 0.01 ms, Fig. 3.8(a). Consequently, relay 12 and relay 21 detect the internal P2G fault and trigger the DCCBs on line 12 at $t = 1.01$ ms, Fig. 3.9. Meanwhile, the relays on healthy lines detect the external fault. Take relay 13 as an example. For 0.9 ms $< t <$ 2 ms, $|\frac{\mathrm{d}i_{13}^p}{\mathrm{d}t} + \frac{\mathrm{d}i_{13}^n}{\mathrm{d}t}|$ remains below DI_{13}^{th1}, Fig. 3.8(a); $\frac{\mathrm{d}i_{13}^p}{\mathrm{d}t}$ does not exceed DI^{th2} but exceeds DI_{13}^{th3}, Fig. 3.8(b). As a result, an external fault is detected by relay 13, and DCCB 13 is blocked for 10 ms, Fig. 3.9. Similarly, other relays on healthy lines all detect the external fault and block their corresponding DCCBs, Fig. 3.8(b)-(c).

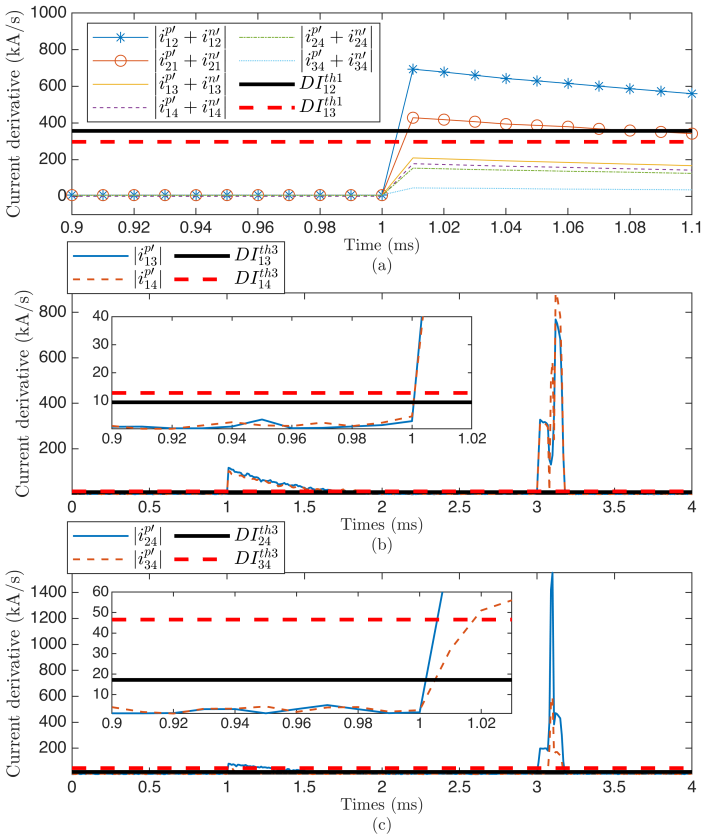

Figure 3.8: Current derivatives on each line during a P2G fault on line 12 near MMC 1 ($r_f = 500\,\Omega$).

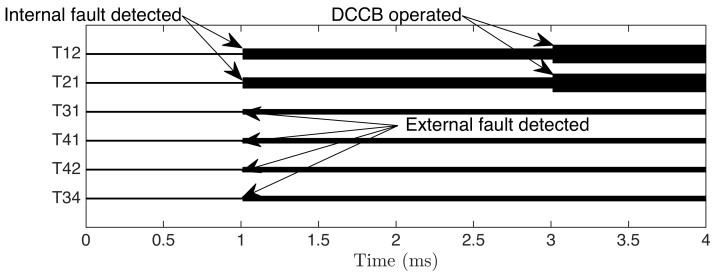

Figure 3.9: Trip signals during a P2P fault on line 12 near MMC 1 ($r_f = 0.01\,\Omega$).

3.4.2.3 Bipole grid with metallic return

The P2P, positive P2M, and positive P2G faults with a resistance of 0.01 Ω are applied to line 12 near MMC 1 in the bipole grid with metallic return at $t = 1$ ms. Fig. 3.10(a) shows current derivatives of the faulty line during the P2P fault. Since $|\frac{\mathrm{d}i^p_{12}}{\mathrm{d}t} + \frac{\mathrm{d}i^n_{12}}{\mathrm{d}t}|$ and $|\frac{\mathrm{d}i^p_{21}}{\mathrm{d}t} + \frac{\mathrm{d}i^n_{21}}{\mathrm{d}t}|$ remain below DI^{th1}_{12}, relay 12 and relay 21 identify this fault as a potential P2P fault through module 1. Then, $\frac{\mathrm{d}i^p_{12}}{\mathrm{d}t}$ and $\frac{\mathrm{d}i^p_{21}}{\mathrm{d}t}$ are compared with DI^{th3} in module 2. Since these two derivatives exceed DI^{th3} in 0.01 ms, an internal P2P fault is detected, and the DCCBs on line 12 are triggered. When the positive P2M fault occurs, $|\frac{\mathrm{d}i^p_{12}}{\mathrm{d}t} + \frac{\mathrm{d}i^n_{12}}{\mathrm{d}t}|$ and $|\frac{\mathrm{d}i^p_{21}}{\mathrm{d}t} + \frac{\mathrm{d}i^n_{21}}{\mathrm{d}t}|$ exceed DI^{th1}_{12}, and $|\frac{\mathrm{d}i^m_{12}}{\mathrm{d}t}|$ and $|\frac{\mathrm{d}i^m_{21}}{\mathrm{d}t}|$ exceed DI^{th2}_{12}. As a result, an internal P2M fault is detected. When the positive P2G fault occurs, $|\frac{\mathrm{d}i^p_{12}}{\mathrm{d}t} + \frac{\mathrm{d}i^n_{12}}{\mathrm{d}t}|$ and $|\frac{\mathrm{d}i^p_{21}}{\mathrm{d}t} + \frac{\mathrm{d}i^n_{21}}{\mathrm{d}t}|$ exceed DI^{th1}_{12}, while $|\frac{\mathrm{d}i^m_{12}}{\mathrm{d}t}|$ and $|\frac{\mathrm{d}i^m_{21}}{\mathrm{d}t}|$ remain below DI^{th2}_{12}. Then, $\frac{\mathrm{d}i^p_{12}}{\mathrm{d}t}$ and $\frac{\mathrm{d}i^p_{21}}{\mathrm{d}t}$ are compared with DI^{th4}_{12} in module 2. Since these two derivatives are larger than the corresponding threshold, an internal P2G fault is detected.

Fig. 3.11 shows the current derivatives of healthy lines during the P2P, positive P2G, and positive P2M faults. According to Fig. 3.11, the relays on lines adjacent to line 12 detect an external fault in all fault scenarios. Take relay 13 as an example, when a P2P fault occurs on line 12 at $t = 1$ ms, $|\frac{\mathrm{d}i^p_{13}}{\mathrm{d}t}|$ rises to around 500 kA/s, Fig. 3.11(a). Even though $|\frac{\mathrm{d}i^p_{13}}{\mathrm{d}t} + \frac{\mathrm{d}i^n_{13}}{\mathrm{d}t}|$ and DI^{th1}_{13} are not plotted in Fig. 3.11(a), $|\frac{\mathrm{d}i^p_{13}}{\mathrm{d}t} + \frac{\mathrm{d}i^n_{13}}{\mathrm{d}t}|$ can never exceed $DI^{th1}_{13} = 1386.63$ kA/s as $|\frac{\mathrm{d}i^p_{13}}{\mathrm{d}t}|$ is about 500 kA/s. Besides, $|\frac{\mathrm{d}i^p_{13}}{\mathrm{d}t}|$ is smaller than $DI^{th3} = 1475.9$ kA/s. As a result, relay 13 proceeds to module 3, and $|\frac{\mathrm{d}i^p_{13}}{\mathrm{d}t}|$ is compared with DI^{th5}_{13}. Since $|\frac{\mathrm{d}i^p_{13}}{\mathrm{d}t}|$ exceeds DI^{th5}_{13} quickly, an external fault is detected, and DCCB 13 is blocked. Similarly, other relays on adjacent lines to line 12 can detect the external fault right after the fault occurrence, Fig. 3.11(b)-(c).

For 1 ms $< t <$ 5 ms, $|\frac{\mathrm{d}i^p_{34}}{\mathrm{d}t}|$ does not exceed DI^{th5}_{34}, indicating relays on line 34 are slightly impacted by the fault on line 12.

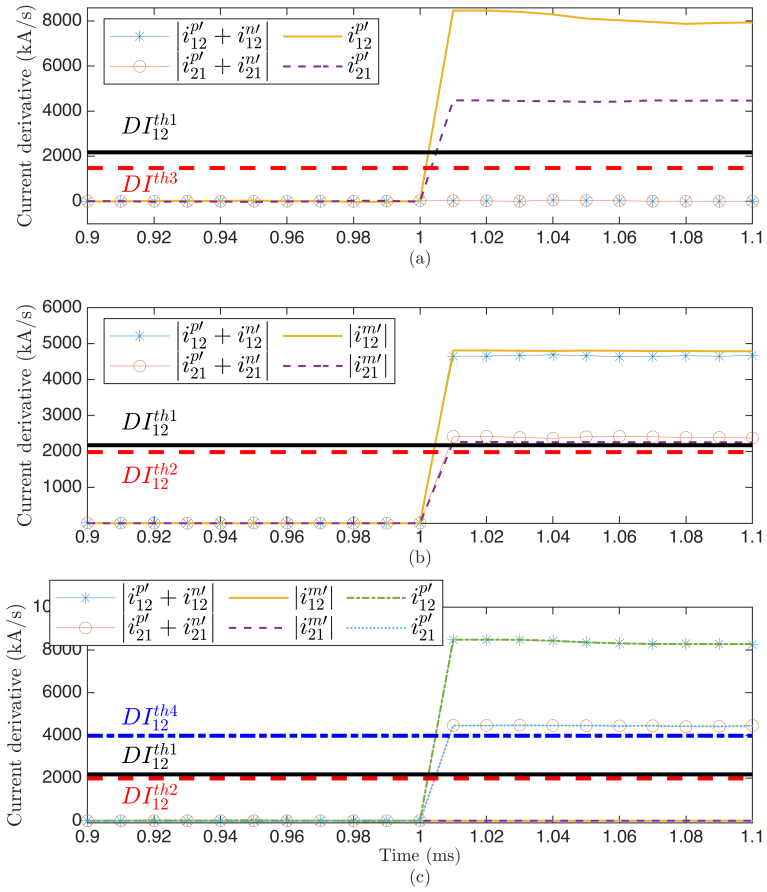

Figure 3.10: Current derivatives of the fault line during a (a) P2P, (b) P2M, and (c) P2G fault on line 12 near MMC 1 ($r_f = 0.01\,\Omega$).

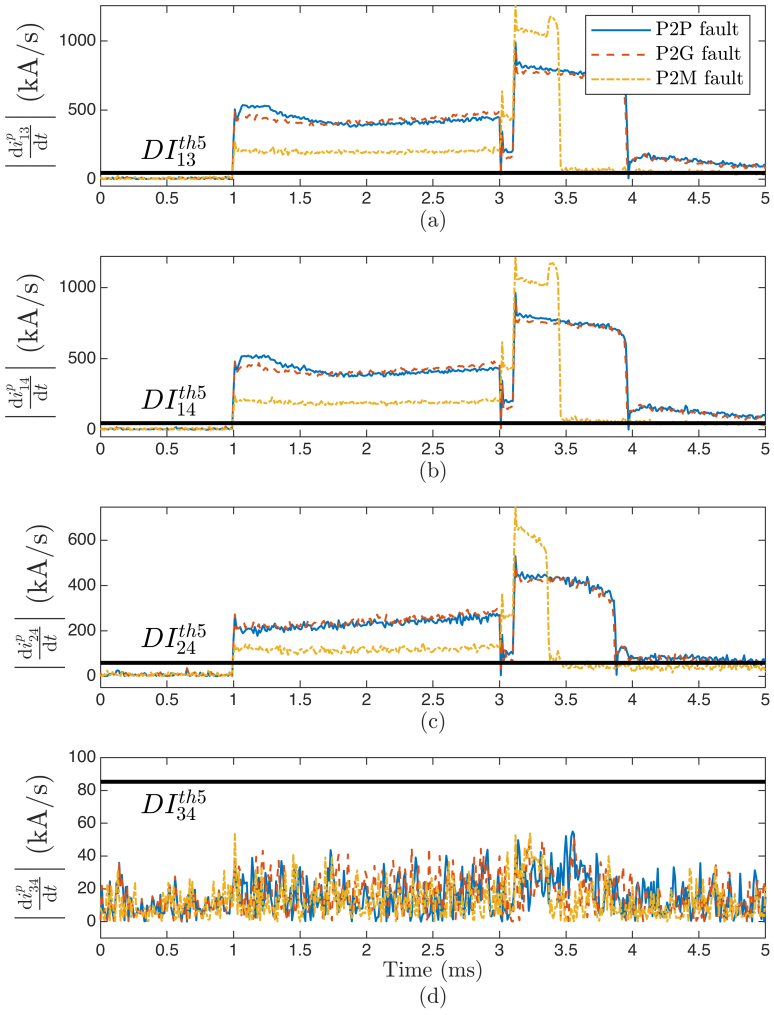

Figure 3.11: Current derivatives of (a) line 13, (b) line 14, (c) line 24, and (d) line 34 during a P2P, P2G, and P2M fault on line 12 near MMC 1 ($r_f = 0.01\,\Omega$).

3.5 Conclusion

This chapter presented a number of current derivative-based relaying algorithms for various HVDC grid topologies including the symmetric monopole grid, the asymmetric monopole grid with ground or metallic return, and the bipole grid with ground or metallic return. The relay settings are determined based on the current derivative calculation method discussed in Chapter 2. Simulation results demonstrate the accuracy of the calculation method and the dependability of the developed relaying algorithm. The designed relaying algorithms are able to reliably protect HVDC grids with various topologies against P2P, P2M, P2G solid and non-solid faults.

Chapter 4

Restoration of HVDC Systems

4.1 Introduction

Various methods are developed to restore an HVDC grid, which has been fully or partially de-energized due to a fault [63, 64]. In [63], an algorithm is developed to restore a four-terminal FB-MMC-based HVDC grid after a permanent DC fault. Since no DCCB is installed in the HVDC grid in [63], the protection system clears the DC fault by blocking all FB-MMCs and opening all ACCBs on the AC grid. When the grid is discharged and the fault current decreases to zero, the disconnectors on the faulty line are opened. In the restoration process of [63], ACCBs are first closed, and then the voltage-controlling FB-MMC is de-blocked. The other three power-controlling FB-MMCs are de-blocked when the DC voltage at the respective terminals is above 90% of the nominal value for more than 20 ms. Right after de-blocking of the power-controlling MMCs for almost 1 s, the power set-points are set to zero to limit the inrush currents. Another algorithm is proposed in [64] to restore an HVDC grid under a temporary fault without blocking the MMCs. However, this algorithm cannot be used in HVDC grids with HB-MMCs because HB-SMs cannot insert negative voltages into the fault current path, and consequently cannot interrupt the fault current.

The few proposed algorithms for the restoration of HVDC grids only consider one type of converter technology, i.e., MMCs with or without fault blocking capability. This chapter proposes an algorithm for restoration of HVDC grids with any combination of FB-MMCs and HB-MMCs. Therefore, the developed restoration algorithm of this chapter can be applied to hybrid HVDC grids as well as HVDC systems with

either FB-MMCs or HB-MMCs. In Section 4.2, the voltage control of FB-MMCs and HB-MMCs during the restoration process is discussed. The test grids used for the studies of this chapter are introduced in Section 4.3. The developed restoration algorithm for hybrid HVDC grids is discussed in Section 4.4. Simulation results are provided in Section 4.5 to evaluate the performance of the developed restoration algorithm. Finally, conclusions are given in Section 4.6.

4.2 Voltage Control of FB- and HB-MMCs

As discussed in Section 1.1.1, an MMC enables a stable DC output voltage by controlling the number of SMs inserted or bypassed in each arm. The SMs in each arm can be considered as a voltage source, whose voltage set-point is determined by

$$v^*_{xu} = \frac{v^*_{out}}{2} - v_x - l^{arm}\frac{\mathrm{d}i_{xu}}{\mathrm{d}t} - r^{arm} i_{xu}\,, \tag{4.1a}$$

$$v^*_{xl} = \frac{v^*_{out}}{2} + v_x - l^{arm}\frac{\mathrm{d}i_{xl}}{\mathrm{d}t} - r^{arm} i_{xl}\,, \tag{4.1b}$$

where v^*_{xu} and v^*_{xl} are the voltage set-points of the upper and lower arms connected to phase $x \in \{a, b, c\}$, respectively, v_x is the AC grid phase voltage, v^*_{out} is the set-point of the MMC DC-terminal voltage, and i_{xu} and i_{xl} are the currents on the upper and lower arms connected with phase x, respectively, Fig. 4.1.

When a converter is de-blocked at t_{db} during the restoration process, the MMC DC terminal voltage v_{out} should be close to the grid DC voltage v_{dc}; otherwise, the voltage difference between the DC grid and the MMC terminal will lead to a large inrush current and voltage oscillations. Therefore, to ensure a smooth restoration, v^*_{out} should be selected such that the MMC generates a terminal voltage v_{out} that is close to the grid voltage. An FB-MMC can be controlled such that the terminal voltage $v_{out,FB}$ reaches any voltage set-points $v^*_{out,FB}$ as FB-SMs can insert both positive and negative voltages in the converter arms. So in an FB-MMC, $v^*_{out,FB} = v_{dc}$ can be selected to generate a terminal voltage $v_{out,FB}$, which is the same as the HVDC grid voltage during the restoration process. On the contrary, for an HB-MMC, the converter DC terminal voltage $v_{out,HB}$ may not track all set-point voltages $v^*_{out,HB}$ as HB-SMs can only generate positive or zero voltages. For example, if $v^*_{out,HB} = 0$, one of the arm-voltage set-points v^*_{xu} or v^*_{xu} becomes negative according to (4.1). Since HB-SMs cannot generate negative voltages, $v_{out,HB}$ cannot follow the set-point $v^*_{out,HB}$ and will not become zero. To better understand this, the relationship between $v_{out,HB}$ and $v^*_{out,HB}$ in an HB-MMC is determined:

$$v_{out,HB} = (v_{xu} + v_{xl}) + r^{arm}(i_{xu} + i_{xl}) + l^{arm}\frac{\mathrm{d}(i_{xu} + i_{xl})}{\mathrm{d}t}\,, \tag{4.2}$$

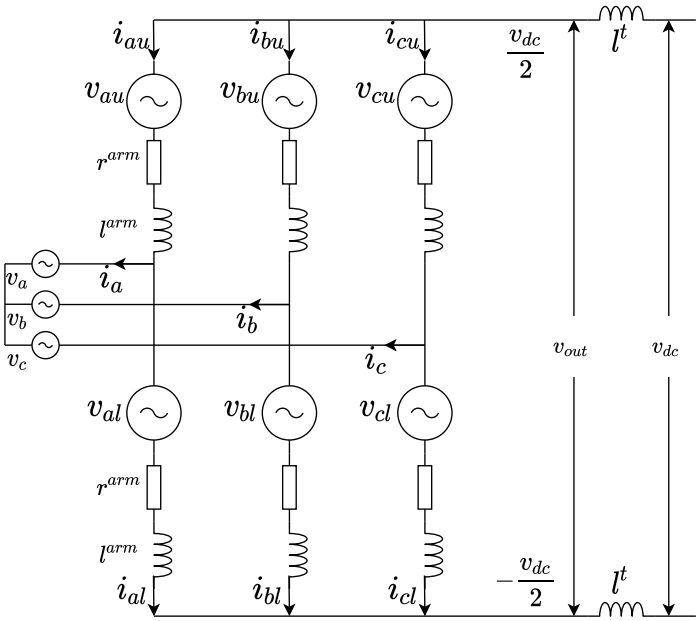

Figure 4.1: Voltage control of an MMC.

where v_{xu} and v_{xl} are the generated voltages on the upper and lower arms connected with phase x, respectively. Assuming $\sum_x^{a,b,c} i_{xu} = \sum_x^{a,b,c} i_{xl} = 0$,

$$\begin{aligned} 3v_{out,HB} - \sum_{x}^{a,b,c}(v_{xu} + v_{xl}) &= r^{arm} \sum_{x}^{a,b,c}(i_{xu} + i_{xl}) + l^{arm} \frac{\mathrm{d}\sum_x^{a,b,c}(i_{xu} + i_{xl})}{\mathrm{d}t} \\ \Rightarrow v_{out,HB} &= \frac{\sum_x^{a,b,c}(v_{xu} + v_{xl})}{3}\,. \end{aligned} \tag{4.3}$$

(4.3) indicates that when an HB-MMC is de-blocked, the generated DC voltage $v_{out,HB}$ is equal to the average of the arm voltages of all three phases. Furthermore, since HB-SMs can only insert positive or zero voltages,

$$v_{xu} = \max(v_{xu}^*, 0)\,, \tag{4.4a}$$
$$v_{xl} = \max(v_{xl}^*, 0)\,. \tag{4.4b}$$

Substituting (4.1) to (4.4) and (4.3) gives the relationship between the set-point of the terminal voltage $v_{out,HB}^*$ and the generated DC terminal voltage $v_{out,HB}$ in an HB-MMC. Using (4.1) to (4.4), Table 4.1 provides several pairs of ($v_{out,HB}^*$,$v_{out,HB}$) and indicates that the minimum voltage $v_{HB,th}$ that an HB-MMC can generate at its DC terminal is $0.622V_m$. This minimum voltage will be used later in Section 4.5 to evaluate the performance of the restoration algorithm.

Table 4.1: Several pairs of $(v^*_{out,HB}, v_{out,HB})$

Pair	1	2	3	4	5	6
$(v^*_{out,HB}, v_{out,HB})$	(0,0.622V_m)	(0.4V_m,0.850V_m)	(0.8V_m,1.087V_m)	(1.2V_m,1.354V_m)	(1.6V_m,1.653V_m)	(2V_m,2V_m)

As discussed earlier, to have a smooth restoration after the de-blocking of MMCs, the converter terminal voltage v_{out} should be increased gradually from the measured terminal voltage to the nominal DC voltage level. Therefore, in the developed restoration algorithm, the DC voltage terminal of the converter is controlled according to (4.5), where $v_{dc}(t_{db})$ is the measured grid voltage when the MMC is de-blocked, and k corresponds to the speed of voltage restoration.

$$v_{out} = v_{dc}(t_{db}) + k(t - t_{db}), \quad t_{db} \leq t \leq, t_{db} + \frac{V_{dc} - v_{dc}(t_{db})}{k}, \tag{4.5a}$$

$$v_{out} = V_{dc}, \quad t > t_{db} + \frac{V_{dc} - v_{dc}(t_{db})}{k}, \tag{4.5b}$$

4.3 Test Systems

Three types of four-terminal HVDC grids are tested in this chapter: a) a grid with only FB-MMCs called FFFF grid, b) a grid with both HB-MMCs and FB-MMCs called FHFH grid, and c) a grid with only HB-MMCs called HHHH grid as shown in Figure 4.2. In each grid, MMC1 controls the DC voltage while other MMCs control the active power. The parameters of the test systems are shown in Table 4.2. Since HB-MMCs cannot interrupt the fault current, an ACCB is inserted between each HB-MMC and the AC grid for fault current interruption.

4.4 Restoration Algorithm

The developed restoration algorithm has three main steps:

i) Fault isolation investigation: In this step, a voltage-pulse is injected to the grid to determine if the fault has been cleared. To do this, the voltage-controlling MMC (MMC1) is de-blocked for Δt_1 s to inject a voltage pulse V_p to the grid. By comparing the reflected wave at the converter terminal with the pre-fault wave, uncleared faults are detected and the restoration process will be terminated.

ii) Voltage restoration: In this step, MMC1, which control the HVDC grid voltage, is restored. If MMC1 is an FB-MMC, it is de-blocked instantaneously and

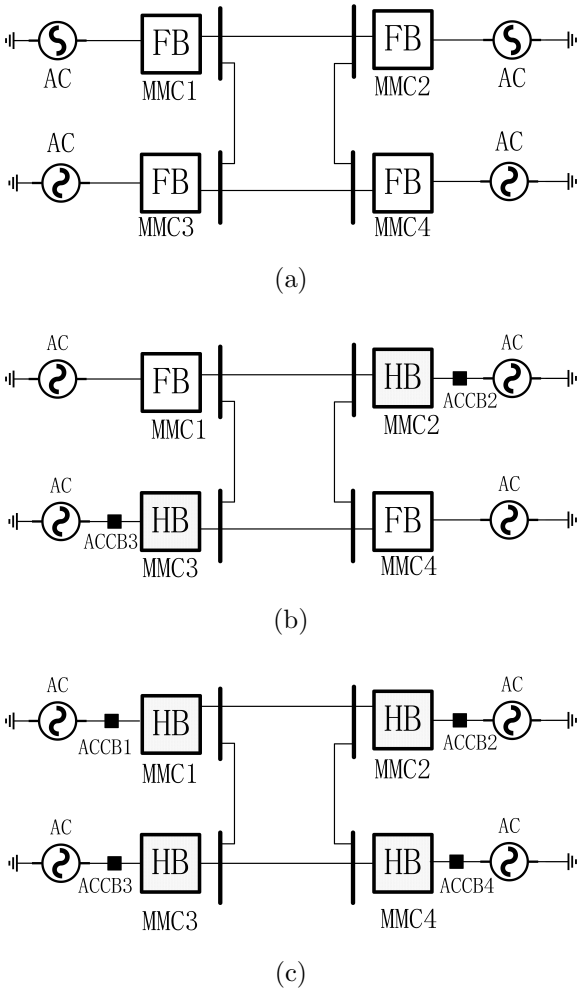

Figure 4.2: Three types of four-terminal HVDC grids: (a) FFFF grid, (b) FHFH grid, and (c) HHHH grid.

the grid voltage is gradually increased. If MMC1 is an HB-MMC, it is de-blocked after ACCB1 is closed, which takes about 3 cycles (50 ms). The grid voltage after closing ACCB1 and right before de-blocking MMC1 is given by (4.6):

$$V_{dc,cls} = \frac{3\sqrt{3}}{\pi} V_m \approx 1.65 V_m \,, \tag{4.6}$$

where V_m is the peak AC phase voltage. As discussed in Section 4.2, an HB-MMC can generate a DC terminal voltage larger than $0.622V_m$. Since $1.65V_m$ is larger than $0.622V_m$, the grid voltage is increased from $1.65V_m$ to the nominal value V_{dc},

Table 4.2: Parameters of the HVDC grid

MMC converter	
Number of SMs per arm	76
Rated SM capacitor voltage	8.5 kV
SM capacitor	3 mF
Arm inductance	50 mH
Control set-points	
Voltage set-point (MMC1)	640 kV
Power set-points (MMC2 & MMC3)	- 900 MW
Power set-point (MMC4)	950 MW
HVDC transmission line	
Rated voltage	640 kV
Rated power	1000 MW
Smoothing inductance	20 mh
Length (all the same)	400 km

by gradually increasing the voltage set-point of the voltage-controlling HB-MMC1 according to (4.5).

iii) Power restoration: In this step, when the DC terminal voltage of MMCn reaches a threshold V_{th}, the converter is restored. If MMCn is an FB-MMC, it is instantaneously de-blocked. If MMCn is an HB-MMC, it is de-blocked after the corresponding ACCB is closed. V_{th} is selected to be three times the magnitude of the voltage pulse V_p to avoid de-blocking of converters, while there are uncleared faults in the grid. In this algorithm, to prevent large inrush currents during restoration, power set-points of the power-controlling MMCs are gradually increased from zero to their nominal values in Δt_2 s.

4.5 Simulation Results

In the simulation studies of this chapter, a P2P short-circuit fault is applied to the middle of the transmission line connecting MMC1 and MMC2 at t =0.01 s, and the fault impedance is 10 Ω. The fault is assumed to be detected in 1 ms. When the fault is detected, MMCs are blocked immediately, and ACCBs are opened in 3 cycles (50 ms). To restore the HVDC grid, first, MMC1, which controls the grid voltage, injects a 200 kV (V_p) pulse into the grid for 0.5 ms. Since the most remote point

in the grid is 400 km away from MMC1, it takes less than 400 km $\times$ $2/v_{trv}$=2.667 ms for MMC1 to detect uncleared faults, where $v_{trv} \approx 3 \times 10^8$ m/s is the speed of traveling waves on overhead lines. To ensure that MMC1 is not restored when the fault still exists in the HVDC grid, a safety factor of four is used and MMC1 is fully restored $4 \times 2.667 \approx 10$ ms after injecting the voltage pulse. In the second step, MMC1 will increase the grid voltage with a speed of k=32 kV/ms to the nominal value. $V_{dc,cls}$ in the test systems of this chapter is 510 kV. In the third step, V_{th} =600 kV is selected, and power set-points of power-controlling MMCs will increase from zero to their nominal values in $\Delta t_2 = 20$ ms when their MMCs are de-blocked. The performance of the developed algorithm for the restoration of the three HVDC grids is evaluated in the remaining of this section.

4.5.1 Restoration of the FFFF grid

In the FFFF grid with four FB-MMCs, all FB-MMCs are blocked at t =0.011 s after the fault occurrence. Since the fault is detected and isolated in 1 ms, fault currents flowing through the four MMCs are not large as shown in Figure 4.3c. At t =0.3 s, a 200 kV voltage pulse is generated by MMC1 and the reflected waveform at the converter terminal shows that the fault is already cleared and the HVDC grid can be restored. The MMC1 terminal voltage waveform for two scenarios, when the fault is cleared and when the fault still exists, is shown in Figure 4.3b. MMC1 is de-blocked at t =0.31 s. The other MMCs are de-blocked when the DC voltages at corresponding terminals reach 600 kV. Since the output voltages of the converters are gradually increased from the measured terminal voltages at the de-blocking instant to the nominal voltage, voltage oscillations during the restoration are small, and large inrush currents are prevented as shown in Figure 4.3. The restoration sequence is provided in Table 4.3.

The developed restoration algorithm of this chapter is compared against the algorithm of [63] and the comparison is shown in Figure 4.4, where solid lines show the waveform of the designed algorithm and dashed lines show the waveform of the algorithm in [63]. Figure 4.4 shows that the designed algorithm, compared to the algorithm of [63], restores the HVDC grid faster. However, the algorithm of [63] results in a more smooth rise of the DC voltage as compared to the algorithm of this chapter, because fault clearance is not investigated prior to grid restoration in the algorithm of [63]. Even though the injected voltage pulse leads to some voltage oscillations in the designed algorithm, this voltage pulse enables a safe restoration and attenuates quickly. The designed algorithm provides faster restoration of the FFFF

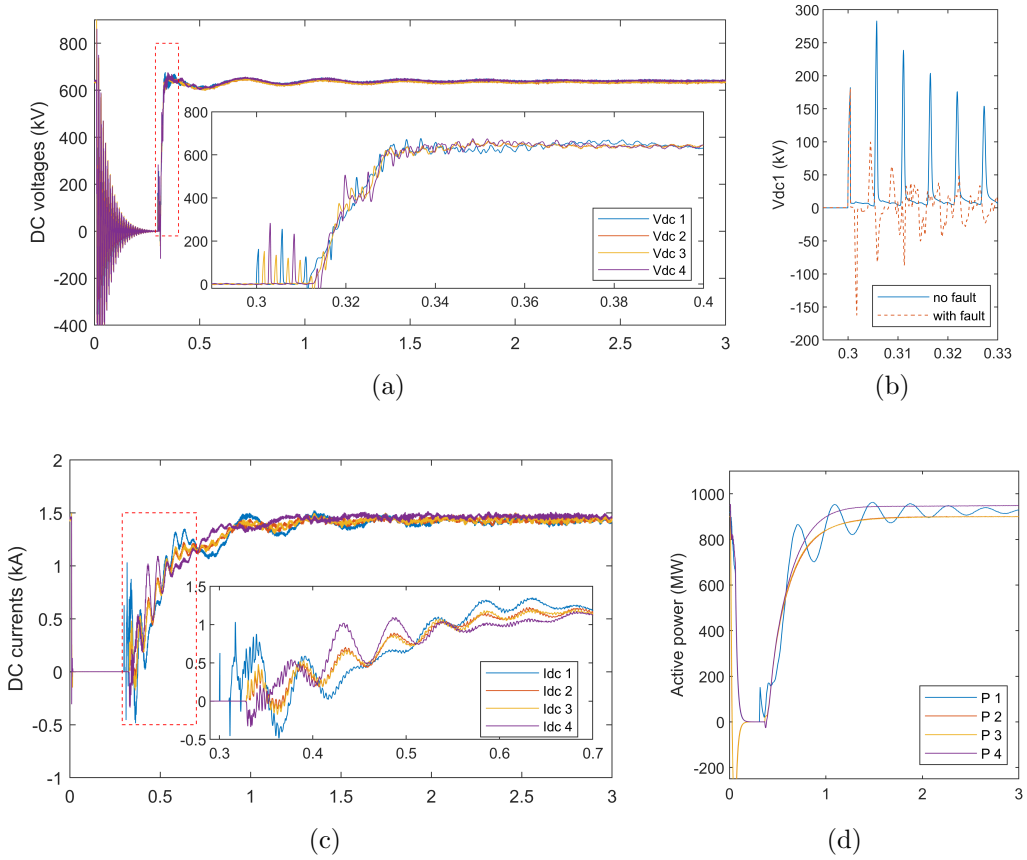

Figure 4.3: Waveform during the restoration of the FFFF grid: (a) DC voltage (fault cleared), (b)$V_{dc}, 1$ when the fault is cleared or not cleared, (c) DC current (fault cleared), and (d) power (fault cleared).

grid because the algorithm of [63] requires 50 ms to close the ACCBs and energize the grid, which is unnecessary as FB-MMCs do not require ACCBs to interrupt the fault current. Furthermore, in [63] power set-points of power-controlling MMCs are set to zero for 1 s after the MMCs are de-blocked, and are changed to their nominal values at the end of the period. In the designed algorithm power set-points are increased from zero to their nominal values over a 1 cycle (16.67 ms) period, which significantly accelerates the restoration process and reduces inrush currents.

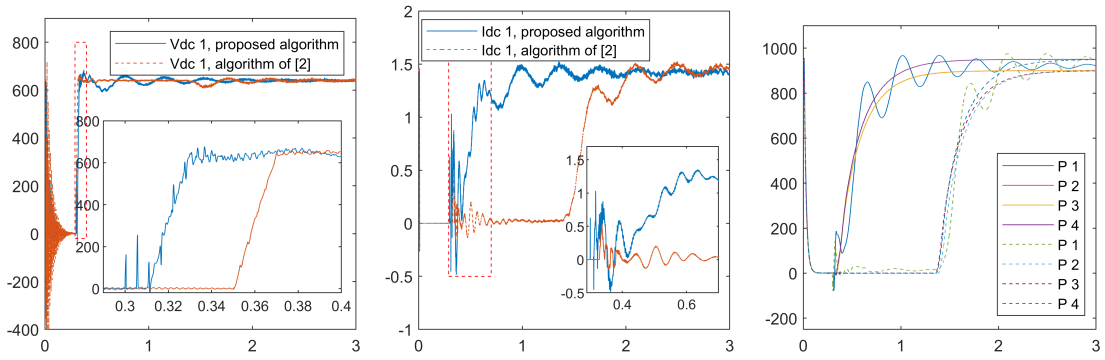

(a) (b) (c)

Figure 4.4: Comparison between the two restoration algorithms applied to the FFFF grid: (a) DC voltages, (b) DC currents, and (c) power.

Table 4.3: Restoration sequence of the three HVDC grids

	developed algorithm			Algorithm of [63]
	FFFF	FHFH	HHHH	FFFF
Fault identification		0.2		N/A
De-block FB-MMC1 (s)	0.21	0.21	0.27	0.2554
De-block HB-MMC2 (s)	0.2288	0.2888	0.27	0.3096
De-block HB-MMC3 (s)	0.2287	0.2887	0.27	0.2942
De-block FB-MMC4 (s)	0.2291	0.2293	0.27	0.3093
Close ACCB1 (s)	N/A	N/A	0.21	0.2054
Close ACCB2 (s)	N/A	0.2788	0.21	0.2054
Close ACCB3 (s)	N/A	0.2787	0.21	0.2054
Close ACCB4 (s)	N/A	N/A	0.21	0.2054

4.5.2 Restoration of the FHFH grid

The fault current in the FHFH grid that contains both FB-MMCs and HB-MMCs is larger than that of the FFFF grid because HB-MMCs cannot interrupt the fault current and rely on ACCBs to clear the fault. Figure 4.5b shows that after ACCBs trip at t =0.061 s, the fault current gradually decays to zero. Figure 4.5 shows the DC voltage, current and active power measured at all converter terminals. Figure 4.5 illustrates that the hybrid HVDC grid is smoothly restored using the designed restoration algorithm. Figure 4.5 shows that neither large inrush currents nor large voltage oscillations are caused during the restoration.

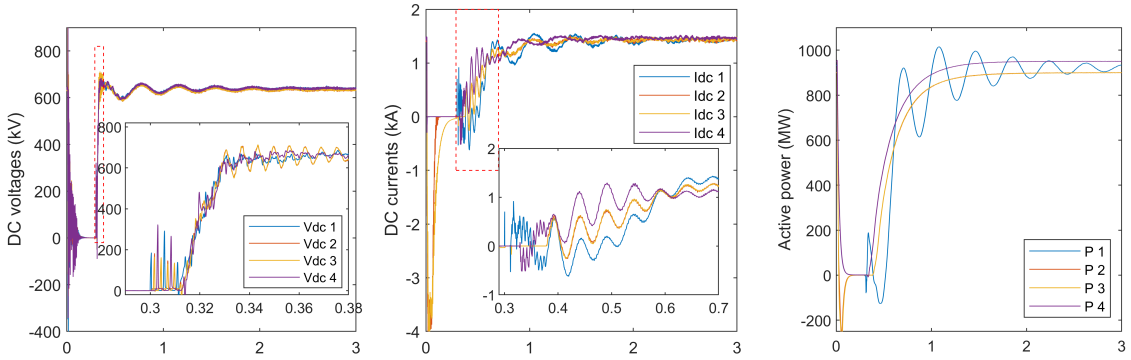

(a) (b) (c)

Figure 4.5: Waveform at each terminal during the restoration of the FHFH grid: (a) DC voltages, (b) DC currents, and (c) power.

4.5.3 Restoration of the HHHH grid

Figure 4.6 shows the restoration of the HHHH grid with four HB-MMCs. In this grid, when ACCB1 is closed, a voltage overshoot is caused due to the current flowing through ACCB1. Then, the grid voltage gradually decays to $1.65V_m$. At t =0.36 s, HB-MMCs are de-blocked and the grid voltage is restored to the nominal value.

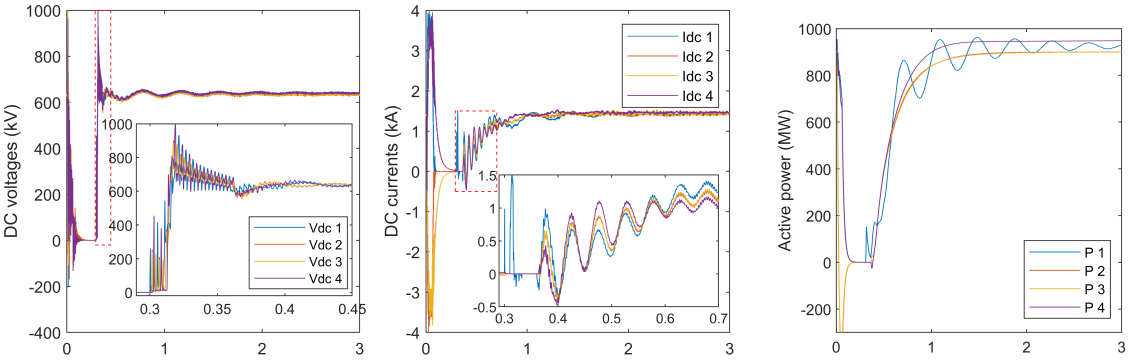

(a) (b) (c)

Figure 4.6: Waveform at each terminal during the restoration of the HHHH grid: (a) DC voltages, (b) DC currents, and (c) power.

4.6 Conclusion

This chapter presents a restoration algorithm for HVDC grids with any combination of converters with and without fault blocking capability. In this restoration algorithm, first, traveling waves resulted from a voltage-pulse injection from one of the converters to the grid is used to identify any uncleared faults. If no existing fault is detected, the converter controlling the grid voltage is first restored to establish the grid voltage, and consecutively converters that control the grid power are restored. The presented restoration algorithm specifies the proper sequence for the restoration of all different types of converters forming the HVDC grid. The restoration of three HVDC grids, which include FB-MMCs, HB-MMCs, or a combination of FB-MMCs and HB-MMCs, is studied in this chapter. To prevent large voltage oscillations and to limit inrush currents, this restoration algorithm increases the terminal voltages of the converters from the measured values to the nominal value and gradually energizes the grid. Also, the power set-points of power-controlling MMCs are increased from zero to their set-point values over one cycle to prevent large inrush currents. Simulation results show that this restoration algorithm can restore different types of grids including hybrid HVDC systems in less than 40 ms, with limited inrush currents and low voltage oscillations.

Chapter 5

Conclusion and Future Work

5.1 Conclusions

This research focuses on developing a protection scheme for HVDC systems with various structures, converters, topologies, and grounding configurations. The contributions of this thesis are summarized as below:

- A set of matrix-form differential equations were developed to calculate the current and current derivative of each line in an HVDC grid right after a DC fault. This set of equations (i) covers various system topologies, grounding configurations, and DC fault types, (ii) provides accurate values of fault currents and current derivatives, (iii) can be easily and quickly formed once the system structure, system topology, MMC parameters, and transmission line parameters are determined, and (iv) can be easily modified once the grid structure changes. Compared to EMT simulations, the matrix-form differential equations can calculate fault currents time-efficiently especially when the HVDC grid is complex.
- A universal current derivative-based relaying scheme is developed for HVDC grids. The designed current derivative-based relay (i) only uses the locally measured current derivatives and requires no communication channels, (ii) is fast, selective, calculation-resource-sparing, and insensitive to the fault type, fault resistance, operating point, and system transients, e.g., trips of DCCBs.
- A systematic approach is developed to calculate the settings of the relays in an HVDC system. This approach does not use the traditional method, which is

based on extensive time-consuming EMT simulations, to obtain the thresholds. The presented approach builds the matrix-form differential equations and uses them to calculate thresholds. Furthermore, for some specific fault scenarios, e.g., a P2P fault in a bipole grid, the developed approach can use only one formula to calculate the threshold corresponding to the fault scenario, significantly increasing the convenience of employing the presented relaying algorithm to these fault scenarios.

- An algorithm that can restore various types of HVDC grids, which may even contain different types of MMCs with and without fault blocking capability is developed. A voltage-control block is also developed for HB-MMCs that serve as voltage controllers in an HVDC system. Compared to conventional restoration algorithms, the presented one can (i) restore hybrid HVDC systems, (ii) restore the systems more quickly, and (iii) restore the system with smaller voltage oscillations and inrush currents.

5.2 Future Works

In continuation of this thesis, further research can be done in the following areas:

- The traveling-wave effect can be considered during calculating fault current derivatives of each line in an HVDC system.
- The performances of the protection scheme in HVDC grids with other types of MMCs, e.g., double-clamp-MMC (DC-MMC) and cascaded HB-MMC, can be studied and the necessary modifications can be implemented.

References

[1] Hao; Wang, Luo; Lori, Dianfeng; Wu, and Pudney Dale. Hierarchical control in a 5-terminal VSC-HVDC project , nov 2014.

[2] Sahar Pirooz Azad. *Small-Signal Dynamic Stability Enhancement Of A DC-Segmented AC Power System*. PhD thesis, University of Toronto, aug 2014.

[3] ABB. HVDC Light: It's time to connect. Technical report, ABB, Ludvika, Sweden, 2012.

[4] Shimin Xue, Jie Lian, Jinlong Qi, and Boyang Fan. Pole-to-Ground Fault Analysis and Fast Protection Scheme for HVDC Based on Overhead Transmission Lines. *Energies*, 10(7):1059, jul 2017.

[5] Chengyu Li, Chengyong Zhao, Jianzhong Xu, Yuke Ji, Fan Zhang, and Ting An. A Pole-to-Pole Short-Circuit Fault Current Calculation Method for DC Grids. *IEEE Transactions on Power Systems*, 32(6):4943–4953, nov 2017.

[6] Jingqiu Yu, Zheren Zhang, Zheng Xu, and Guoteng Wang. An Equivalent Calculation Method for Pole-to-Ground Fault Transient Characteristics of Symmetrical Monopolar MMC Based DC Grid. *IEEE Access*, 8:123952–123965, 2020.

[7] Wikipedia. Climate change - Wikipedia, 2021.

[8] MacMillan Amanda and Turrentine Jeff. Global Warming 101 - Definition, Facts, Causes and Effects of Global Warming — NRDC, 2021.

[9] Wikipedia. List of parties to the Paris Agreement - Wikipedia, 2021.

[10] Brian Walsh, Philippe Ciais, Ivan A. Janssens, Josep Peñuelas, Keywan Riahi, Felicjan Rydzak, Detlef P. Van Vuuren, and Michael Obersteiner. Pathways for balancing CO2 emissions and sinks. *Nature Communications*, 8(1):1–12, apr 2017.

[11] Moore Jon and Henbest Seb. New Energy Outlook 2020. Technical report, 2020.

[12] Kim Chan-Ki, K. Sood Vijay, Jang Gil-Soo, Lim Seong-Joo, and Lee Seok-Jin. *HVDC Transmission: Power Conversion Applications in Power Systems*. Wiley-IEEE Press, 2009.

[13] Boon Teck Ooi and Xiao Wang. Boost type PWM HVDC transmission system. *IEEE Transactions on Power Delivery*, 6(4):1557–1563, 1991.

[14] MaximizeMarketResearch. HVDC Converter Station Market -Industry Analysis and Forecast (2019-2026) – by Configuration (Monopolar, BI-Polar and Others), by Technology (LCC and VSC), by Component (Valve, Converter Transformers and Others), by Power Rating (Below 500 MW , More Than. Technical report, 2020.

[15] MarketsandMarkets. HVDC Converter Station Market by Configuration (Monopolar, Bi-Polar, Back-to-Back, Multi-Terminal), Technology (LCC, VSC), Component (Valve, Converter Transformer, Harmonic Filter, Reactor), Power Rating, and Region - Global Forecast to 2022. Technical report, 2017.

[16] Wikipedia. List of HVDC projects - Wikipedia, 2021.

[17] NS Energy. HVDC fifty years on - NS Energy, oct 2004.

[18] Guangfu Tang, Zhiyuan He, Hui Pang, Xiaoming Huang, and Xiao-ping Zhang. Basic topology and key devices of the five-terminal DC grid. *CSEE Journal of Power and Energy Systems*, 1(2):22–35, jul 2015.

[19] Lu Yanchun, Liu Tongliang, Jiang Ganggang, Zhang Yue, and Liu Yanwei. Research on the Fault Characteristics of DC side Based on MMC-HVDC. In *Proceedings 2018 Chinese Automation Congress, CAC 2018*, pages 520–525. Institute of Electrical and Electronics Engineers Inc., jan 2019.

[20] Willem Leterme, Pieter Tielens, Steven De Boeck, and Dirk Van Hertem. Overview of grounding and configuration options for meshed HVDC grids, dec 2014.

[21] Oluwafemi E. Oni, Innocent E. Davidson, and Kamati N.I. Mbangula. A review of LCC-HVDC and VSC-HVDC technologies and applications. In *EEEIC 2016 - International Conference on Environment and Electrical Engineering*. Institute of Electrical and Electronics Engineers Inc., aug 2016.

[22] Sixing Du, Apparao Dekka, Bin Wu, and Navid Zargari. *Modular Multilevel Converters: Analysis, Control, and Applications*. John Wiley Sons, Inc., Hoboken, NJ, USA, jan 2017.

[23] Jakob Glasdam, Jesper Hjerrild, Lukasz Hubert Kocewiak, and Claus Leth Bak. Review on multi-level voltage source converter based HVDC technologies for grid connection of large offshore wind farms. In *2012 IEEE International Conference on Power System Technology, POWERCON 2012*, 2012.

[24] Xiaofang Chen, Chengyong Zhao, and Chungang Cao. Research on the fault characteristics of HVDC based on modular multilevel converter. In *2011 IEEE Electrical Power and Energy Conference, EPEC 2011*, pages 91–96, 2011.

[25] Ghazal Falahi. *Design, Modeling and Control of Modular Multilevel Converter based HVDC Systems.* PhD thesis, North Carolina State University, dec 2014.

[26] Paul D. Judge, Geraint Chaffey, Michael M.C. Merlin, Philip R. Clemow, and Tim C. Green. Dimensioning and modulation index selection for the hybrid modular multilevel converter. *IEEE Transactions on Power Electronics*, 33(5):3837–3851, may 2018.

[27] E. Kontos, R. Teixeira Pinto, S. Rodrigues, and P. Bauer. Impact of HVDC Transmission System Topology on Multiterminal DC Network Faults. *IEEE Transactions on Power Delivery*, 30(2):844–852, apr 2015.

[28] Hani Saad, Tarek Ould-Bachir, Jean Mahseredjian, Christian Dufour, Sebastien Dennetiere, and Samuel Nguefeu. Real-time simulation of MMCs using CPU and FPGA. *IEEE Transactions on Power Electronics*, 30(1):259–267, 2015.

[29] Noman Ahmed, Lennart Angquist, Staffan Norrga, Antonios Antonopoulos, Lennart Harnefors, and Hans Peter Nee. A computationally efficient continuous model for the modular multilevel converter. In *IEEE Journal of Emerging and Selected Topics in Power Electronics*, volume 2, pages 1139–1148. Institute of Electrical and Electronics Engineers Inc., dec 2014.

[30] Shilin Gao, Hua Ye, and Yutian Liu. Accurate and Efficient Estimation of Short-Circuit Current for MTDC Grids Considering MMC Control. *IEEE Transactions on Power Delivery*, 35(3):1541–1552, jun 2020.

[31] Yujun Li, Jiapeng Li, Guihong Wu, Liansong Xiong, Ke Jia, and Zhao Xu. DC Fault Analysis Models of Three Converter Topologies Considering Control

Effects. *IEEE Transactions on Industrial Electronics*, 67(11):9480–9491, nov 2020.

[32] Ning Tong, Xiangning Lin, Yan Li, Zhihao Hu, Neng Jin, Fanrong Wei, and Zhengtian Li. Local Measurement-Based Ultra-High-Speed Main Protection for Long Distance VSC-MTDC. *IEEE Transactions on Power Delivery*, 34(1):353–364, feb 2019.

[33] J. Häfner and B. Jacobson. Proactive Hybrid HVDC Breakers - A key Innovation for Reliable HVDC Grids. In *CIGRE Bologna 2011*, 2011.

[34] Matthias K. Bucher and Christian M. Franck. Analytic Approximation of Fault Current Contribution from AC Networks to MTDC Networks during Pole-to-Ground Faults. *IEEE Transactions on Power Delivery*, 31(1):20–27, feb 2016.

[35] Hani Saad, Sebastien Dennetiere, Jean Mahseredjian, Philippe Delarue, Xavier Guillaud, Jaime Peralta, and Samuel Nguefeu. Modular multilevel converter models for electromagnetic transients. *IEEE Transactions on Power Delivery*, 29(3):1481–1489, 2014.

[36] Jianzhong Xu, Aniruddha M. Gole, and Chengyong Zhao. The Use of Averaged-Value Model of Modular Multilevel Converter in DC Grid. *IEEE Transactions on Power Delivery*, 30(2):519–528, apr 2015.

[37] Wikipedia. Incidence matrix - Wikipedia.

[38] Matlab. Create diagonal matrix or get diagonal elements of matrix - MATLAB diag.

[39] D. K.J.S. Jayamaha, N. W.A. Lidula, and A. D. Rajapakse. Protection and grounding methods in DC microgrids: Comprehensive review and analysis, mar 2020.

[40] Rui Li, Lie Xu, and Liangzhong Yao. DC fault detection and location in meshed multiterminal HVDC systems based on DC reactor voltage change rate. *IEEE Transactions on Power Delivery*, 32(3):1516–1526, jun 2017.

[41] Maximilian Stumpe, Philipp Tünnerhoff, Jaykumar Dave, Armin Schnettler, Dominik Ergin, Andre Schön, Klaus Würflinger, and Frank Schettler. DC fault protection for modular multi-level converter-based HVDC multi-terminal systems with solid state circuit breakers. *IET Generation, Transmission & Distribution*, 12(12):3013–3020, jul 2018.

[42] Raymundo E. Torres-Olguin and Hans Kristian Hoidalen. Inverse time overcurrent protection scheme for fault location in multi-terminal HVDC. In *2015 IEEE Eindhoven PowerTech, PowerTech 2015*. Institute of Electrical and Electronics Engineers Inc., aug 2015.

[43] Chenhao Zhang, Guobing Song, Ting Wang, and Xinzhou Dong. An Improved Non-unit Traveling Wave Protection Method with Adaptive Threshold Value and its Application in HVDC Grids. *IEEE Transactions on Power Delivery*, 2019.

[44] Sahar Pirooz Azad and Dirk Van Hertem. A Fast Local Bus Current-Based Primary Relaying Algorithm for HVDC Grids. *IEEE Transactions on Power Delivery*, 32(1):193–202, feb 2017.

[45] Willem Leterme, Jef Beerten, and Dirk Van Hertem. Nonunit protection of HVDC grids with inductive DC cable termination. *IEEE Transactions on Power Delivery*, 31(2):820–828, apr 2016.

[46] Ricardo C. Santos, Simon Le Blond, Denis V. Coury, and Raj K. Aggarwal. A novel and comprehensive single terminal ANN based decision support for relaying of VSC based HVDC links. *Electric Power Systems Research*, 141:333–343, dec 2016.

[47] Qingqing Yang, Simon Le Blond, Raj Aggarwal, Yawei Wang, and Jianwei Li. New ANN method for multi-terminal HVDC protection relaying. *Electric Power Systems Research*, 148:192–201, jul 2017.

[48] Wang Xiang, Saizhao Yang, and Jinyu Wen. ANN-based robust DC fault protection algorithm for MMC high-voltage direct current grids. *IET Renewable Power Generation*, 14(2):199–210, feb 2020.

[49] Wang Xiang, Saizhao Yang, Lie Xu, Junjie Zhang, Weixing Lin, and Jinyu Wen. A Transient Voltage-Based DC Fault Line Protection Scheme for MMC-Based DC Grid Embedding DC Breakers. *IEEE Transactions on Power Delivery*, 34(1):334–345, feb 2019.

[50] Yujun Li, Lei Wu, Jiapeng Li, Liansong Xiong, Xian Zhang, Guobing Song, and Zhao Xu. DC Fault Detection in MTDC Systems Based on Transient High Frequency of Current. *IEEE Transactions on Power Delivery*, 34(3):950–962, jun 2019.

[51] Xu Chu, Guobing Song, and Jun Liang. Analytical method of fault characteristic and non-unit protection for HVDC transmission lines. *CSEE Journal of Power and Energy Systems*, 2(4):37–43, dec 2016.

[52] Yujun Li, Jiapeng Li, Liansong Xiong, Xian Zhang, and Zhao Xu. DC Fault Detection in Meshed MTdc Systems Based on Transient Average Value of Current. *IEEE Transactions on Industrial Electronics*, 67(3):1932–1943, mar 2020.

[53] Yew Ming Yeap and Abhisek Ukil. Fault detection in HVDC system using Short Time Fourier Transform. In *IEEE Power and Energy Society General Meeting*, volume 2016-Novem. IEEE Computer Society, nov 2016.

[54] Dongyu Li, Abhisek Ukil, Kuntal Satpathi, and Yew Ming Yeap. Improved S Transform Based Fault Detection Method in VSC Interfaced DC System. *IEEE Transactions on Industrial Electronics*, pages 1–1, apr 2020.

[55] K. De Kerf, K. Srivastava, M. Reza, D. Bekaert, S. Cole, D. Van Hertem, and R. Belmans. Wavelet-based protection strategy for DC faults in multi-terminal VSC HVDC systems. *IET Generation, Transmission and Distribution*, 5(4):496–503, apr 2011.

[56] Dimitrios Tzelepis, Grzegorz Fusiek, Adam Dysko, Pawel Niewczas, Campbell Booth, and Xinzhou Dong. Novel Fault Location in MTDC Grids with Non-Homogeneous Transmission Lines Utilizing Distributed Current Sensing Technology. *IEEE Transactions on Smart Grid*, 9(5):5432–5443, sep 2018.

[57] Guobing Song, Zhongxue Chang, Chenhao Zhang, Sayed Tassawar Hussain Kazmi, and Wei Zhang. A High Speed Single-Ended Fault-Detection Method for DC Distribution Line - Part II: Protection Scheme. *IEEE Transactions on Power Delivery*, 35(3):1257–1266, jun 2020.

[58] Jeremy Sneath and Athula D. Rajapakse. Fault Detection and Interruption in an Earthed HVDC Grid Using ROCOV and Hybrid DC Breakers. *IEEE Transactions on Power Delivery*, 31(3):971–981, jun 2016.

[59] Chengyu Li, Aniruddha M. Gole, and Chengyong Zhao. A fast DC fault detection method using DC reactor voltages in HVdc grids. *IEEE Transactions on Power Delivery*, 33(5):2254–2264, oct 2018.

[60] Dimitrios Tzelepis, Adam Dysko, Grzegorz Fusiek, John Nelson, Pawel Niewczas, Dimitrios Vozikis, Philip Orr, Neil Gordon, and Campbell David

Booth. Single-ended differential protection in MTDC networks using optical sensors. *IEEE Transactions on Power Delivery*, 32(3):1605–1615, jun 2017.

[61] Shuo Zhang, Guibin Zou, Qiang Huang, Bin Xu, and Jun Li. Single-ended line protection for MMC-MTDC grids. *IET Generation, Transmission and Distribution*, 13(19):4331–4338, oct 2019.

[62] Xue-Rong Yong. Short Communication: Two Properties of Diagonally Dominant Matrices. *Numerical Linear Algebra with Applications*, 3(2):173–177, mar 1996.

[63] E. Kontos, R. Teixeira Pinto, and P. Bauer. Providing dc fault ride-through capability to H-bridge MMC-based HVDC networks. In *9th International Conference on Power Electronics - ECCE Asia: "Green World with Power Electronics", ICPE 2015-ECCE Asia*, pages 1542–1551. Institute of Electrical and Electronics Engineers Inc., jul 2015.

[64] Shenghui Cui and Seung Ki Sul. A Comprehensive DC Short-Circuit Fault Ride Through Strategy of Hybrid Modular Multilevel Converters (MMCs) for Overhead Line Transmission. *IEEE Transactions on Power Electronics*, 31(11):7780–7796, 2016.